Numerical analysis of Dielectric Barrier Discharge Plasma Actuators for supersonic flow applications

by

Aliaksandr Murzionak

A Thesis submitted to

the Faculty of Graduate Studies and Research

in partial fulfilment of

the requirements for the degree of

Doctor of Philosophy

in

Aerospace Engineering

Department of Mechanical and Aerospace Engineering

Carleton University

Ottawa, Ontario, Canada

February 2023

Copyright ©

2023 - Aliaksandr Murzionak

Abstract

Surface Dielectric Barrier Discharge Plasma Actuator (SDBD PA) is a device that allows for a flow control near a surface of an object. In its simplest form the device consists of one electrode exposed to the atmosphere, dielectric and encapsulated grounded electrode. The device generates strong electric due to high voltage applied to the exposed electrode. Under the effect of the strong electric field the gas in the atmosphere is ionized and turns into plasma, which is manipulated by changing the electric field. The energy from the plasma is transferred to the surrounding gas through particle collisions allowing for the airflow control.

The current work is concentrated on the supersonic applications of SDBD PA and aims at answering two questions:

- What effects does supersonic shock have on plasma generated by SDBD PA?
- What effects does SDBD PA have on supersonic shock?

To answer these questions an OpenFOAM solver was developed that allows to simulate plasma within a supersonic flow. The solver is based on electron-positive nitrogen ions drift-diffusion model for plasma. Several simulations are performed to observe the plasma behaviour: plasma propagation through a frozen shock along a flat plate, supersonic flow under free-slip and no-slip conditions around a wedge with SDBD PA at the tip of the wedge. The Mach number varied from 1.3 to 2, depending on the simulation.

The results demonstrate that as the plasma passes through the shock from low to high pressure side the ionization process is slowed down. If the rise in pressure across the shock is too high then it is possible to quench the ionization process completely. During the plasma propagation along the dielectric surface, the current flowing through the plasma generates heat, which in turn generates a compression wave. Most of the heating is concentrated within the plasma front, therefore as long as the plasma continues to propagate the source of compression wave is also being shifted. This allows for airflow adjustment within the supersonic flow boundary layer.

Further research is needed to optimise the SDPD PA geometry and operational profile for supersonic flow control.

Acknowledgments

I would like to thank professor Etele for his guidance during the course of my studies, and for his patience with this student of his.

A special thank you to my brother, who did his best to encourage me and who spent a lot of his time to go through this work to make it better.

Also, I would like to thank my parents for their continuous support throughout my years of studies.

Table of Contents

List of Tables

List of Figures

List of Acronyms

Acronyms	Definition
1D	1 Dimensional
2D	2 Dimensional
3D	3 Dimensional
CFD	Computation Fluid Dynamics
CPSJA	Counter-flow Plasma Synthetic Jet Actuator
DBD	Dielectric Barrier Discharge
DDBD	Double Dielectric Barrier Discharge
DGTEPA	Dual-Grounded Tri-Electrode Plasma Actuator
GCI	Grid Convergence Index
LAFPA	Localized Arc Filament Plasma Actuator
LEC	Lumped-Element Circuit model
NSDBD	NanoSecond Dielectric Barrier Discharge
PA	Plasma Actuator

PIC-DSMC	Particle-In-Cell Direct-Simulation-Monte-Carlo
SDBD	Single/Surface Dielectric Barrier Discharge

List of Symbols

Symbols	Units	Definition
$\mathbf{B}$	T	Magnetic Field
c	m/s	Speed of light in a vacuum ($2.998 \cdot 10^8$)
c_p	J/kgK	Specific heat capacity at constant pressure
c_v	J/kgK	Specific heat capacity at constant volume
$\mathbf{D}$	C/m^2	Electric displacement field
D_k	m^2/s	Diffusion coefficient of species k (e.g. ions, electrons)
e_o	C	Elementary charge ($1.602 \cdot 10^{-19}$)
$\mathbf{E}$	V/m	Electric field
$\mathbf{f}$	N/m^3	Volumetric force
$\mathbf{J}$	A/m^2	Current density
k	W/mK	Thermal conductivity
k_B	J/K	Boltzmann constant ($1.3806 \cdot 10^{-23}$)
k_t		Thermodiffusion relation

M		Mach Number
$\mathbf{n}$		Surface normal vector
N_k	m^{-3}	Number of particles density of species k (e.g. ions, electrons)
P	Pa	Pressure
Re		Reynolds Number
t	s	Time
T	K	Temperature
u	J/kg	Internal energy
$\mathbf{V}$	m/s	Velocity
V_{dr}	m/s	Electron drift velocity
q_{th}	W/m^3	Heat generation due to plasma
α	m^{-1}	Ionization rate
β	m^3/s	Recombination rate
γ_m		Effective secondary emission coefficient for metal
γ_d		Effective secondary emission coefficient for dielectric
Γ_k	$m^{-2}s^{-1}$	Flux of species k (e.g. ions, electrons)
ϵ	F/m	Absolute permittivity

ϵ_0	F/m	Absolute permittivity of vacuum ($8.8541 \cdot 10^{-12}$)
ϵ_r		Relative permittivity
λ_D	m	Debye length
μ	$Pa\ s$	Dynamic viscosity
μ_B	H/m	Vacuum permeability ($4\pi \cdot 10^{-7}$)
μ_k	m^2/Vs	Mobility of species k (e.g. ions, electrons)
ρ	kg/m^3	Mass density
ρ_c	C/m^3	Charge density
σ_c	C/m^2	Surface charge density
ϕ_E	V	Electric potential

Superscript

$*$	Excited molecules

Subscript

c	Charge
e	Electrons
i	Ions
k	Species k (e.g. ions, electrons)
p	Positive ions

Chapter 1

Introduction

1.1 Plasma

A plasma actuator is a device that uses plasma to adjust a flow in the vicinity of the actuator. Plasma is the fourth state of matter (the first three being solid, liquid, and gas). It is a neutrally charged ionized gas. This means that the number of negatively charged particles is the same as the number of positively charged particles. Since the gas is ionized it is highly conductive and as such it is sensitive to any changes in electric fields. Charge neutrality is ensured by highly mobile charges that quickly react to any changes in the surrounding electric field. The size of non-neutral regions does not exceed what is called Debye length (λ_D) - the maximum distance between two charged particles that are not shielded from each others electric field. Table 1.1 shows examples of some of the key parameters for different types of plasma such as electron concentration (N_e), electron temperature (T_e), Debye radius (length) and the size of a typical plasma cloud. As seen from the table, the Debye length (or radius) varies significantly depending on the type of plasma. The plasma created by a plasma actuator generally fits within the micro-plasma classification. Plasma can be subdivided into thermal (equilibrium) and non-thermal (non-equilibrium or cold) plasma, collisional or collision-less. Thermal equilibrium implies that the electron temperature is on the

Type of plasma	Typical N_e (cm^{-3})	Typical T_e (eV)	Debye radius(cm)	Typical size (cm)
Earth ionosphere	10^5	0.03	0.3	10^6
Flames	10^8	0.2	0.03	10
He-Ne laser	10^{11}	3	0.003	3
Gliding arc	10^{12}	1	$5 \cdot 10^{-4}$	10
Hg lamp	10^{14}	4	$3 \cdot 10^{-5}$	0.3
Solar chromosphere	10^9	10	0.03	10^9
Lightning	10^{17}	3	$3 \cdot 10^{-6}$	100
Micro-plasma	10^{11}	3	0.003	0.003

Table 1.1: Comparison of Debye Radius and characteristic size for different plasma systems [1].

same order of magnitude as the temperature of ions and neutral particles. In the case of non-equilibrium plasma electrons have a much higher temperature than the surrounding ions or neutral particles. This means that non-thermal plasma can be used without significant thermal protection since electrons are unable to significantly increase the surrounding temperature due to their low mass.

Depending on the gas density and collision frequency the effect of particle collisions may or may not be ignored. "Collision-less" plasma is attributed to low density plasma (e.g. interstellar space) where the collision frequency is low. This prevents the approximation of the plasma as a continuous fluid and as such the numerical calculations are limited to so called kinetic models where each particle is modelled on it own. At atmospheric pressures the frequency between charged particle collisions is high hence one obtains a collisional plasma.

It is estimated that plasma covers 99 % of the known universe [1]. The current applications of plasma are very diverse and include power generation, chemical catalyst, illumination (e.g. neon lights) and many others. Figure 1.1 shows some examples of plasma in nature as well as those created by humans. Naturally occurring plasma

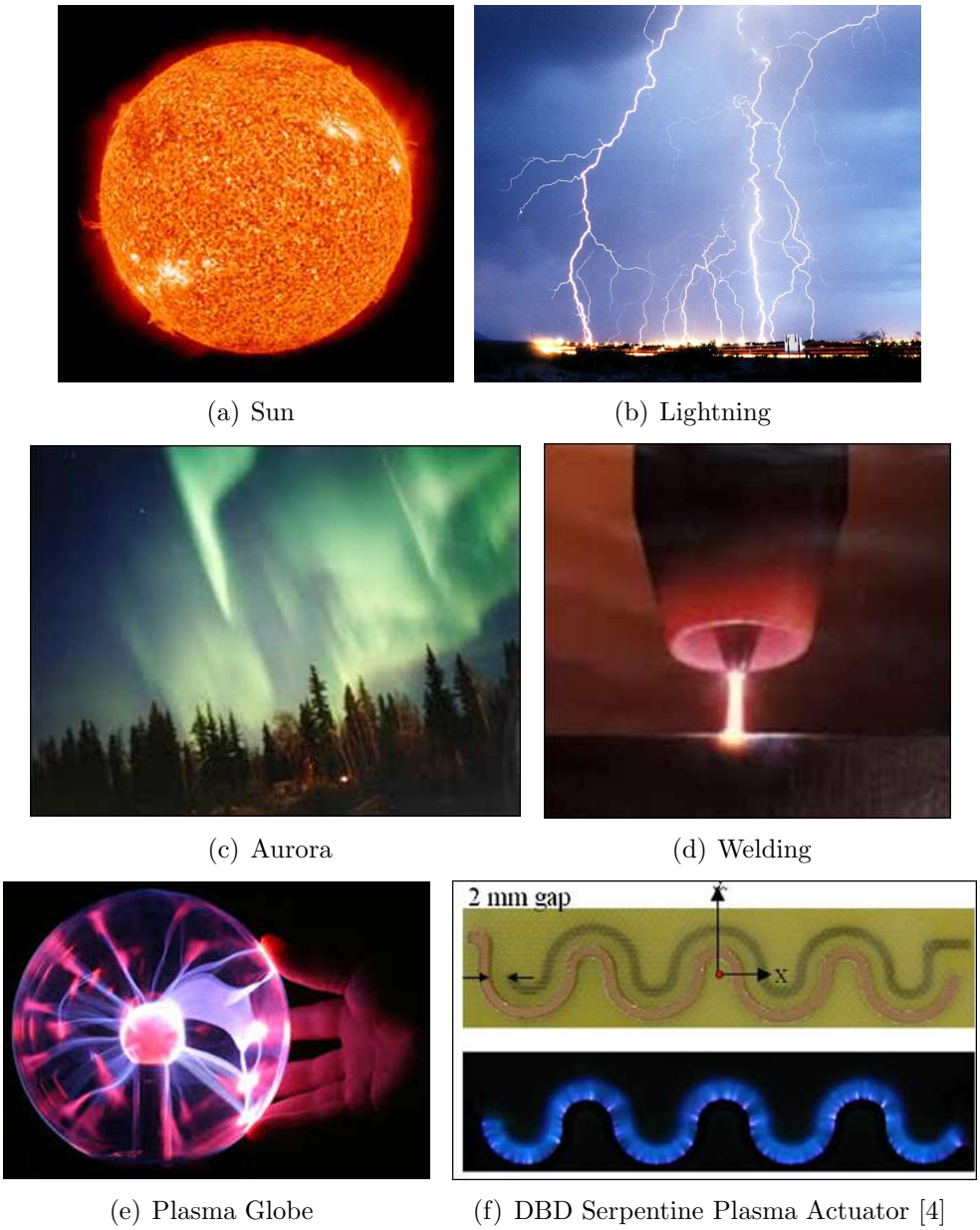

(a) Sun (b) Lightning

(c) Aurora (d) Welding

(e) Plasma Globe (f) DBD Serpentine Plasma Actuator [4]

Figure 1.1: Examples of plasma.

includes stars, lightning, and Auroras (Figure 1.1 a,b,c). While stars and lightning are examples of hot or thermal plasma (temperatures are in the several thousands of Kelvin), Auroras are weakly ionized plasma and are an example of non-equilibrium plasma. Plasma welding (Figure 1.1 d) is an example of a human-made thermal plasma in which case the working gas heats up to high temperatures high enough to

weld or cut metal. A plasma globe (Figure 1.1 e) produces a non-thermal plasma arc between an electrode and a dielectric (the globe), which operates in the kilohertz-kilovolt range. Surface (also Single) Dielectric Barrier Discharge (SDBD) Plasma Actuators (PA) are yet another example of devices which produce non-thermal collisional plasma. The temperature near the vicinity of a PA is only slightly higher (within 100 K) than the surrounding gas temperature. Figure 1.1 (f) shows a serpentine configuration of DBD PA that can be used to generate streamwise vortices close to a surface.

1.2 What is Plasma Actuator?

SDBD PAs are a relatively new application of plasma for flow adjustment or actuation [5]. A PA is an electric device that generates plasma in a small region through an applied electric field, and due to the interaction of the electric field and the generated plasma the airflow is altered in the vicinity of the actuator. The effects of the actuator depend on the type of actuator and its position with respect to the oncoming flow. These effects include the prevention or excitation of boundary flow separation, creation of streamwise vortices, and modification of aerodynamic shock-waves among others. Figure 1.2 shows the schematics of a simple Surface Dielectric Barrier Discharge Plasma Actuator (SDBD PA). The exposed electrode is connected to a voltage supply (usually in the kHz and kV range), while the encapsulated electrode is grounded and separated from the exposed electrode with a dielectric barrier. The air above the dielectric barrier on top of the grounded electrode is ionized and turns into plasma. The charged particles move under the effect of the generated electric field and in turn generate a time-averaged force on the flow in the direction from the exposed/charged electrode towards the encapsulated/grounded electrode and slightly towards the surface.

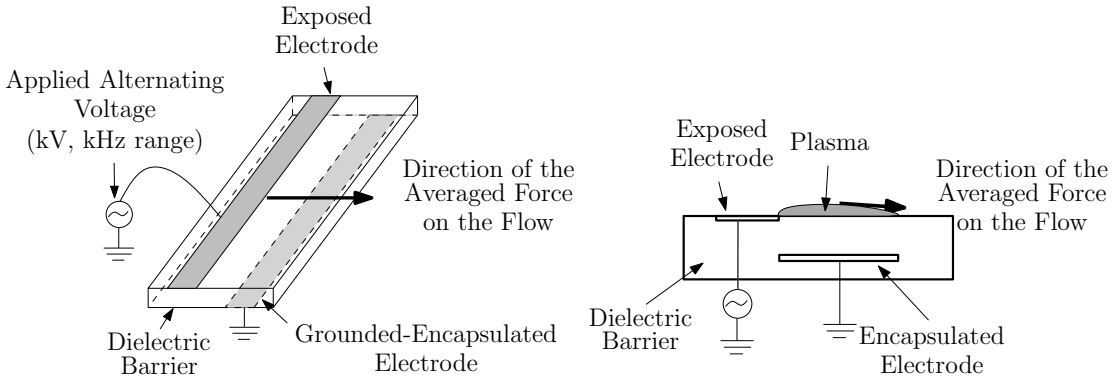

(a) 3D view (b) side view

Figure 1.2: Schematic of SDBD PA.

The main use of plasma actuators is to adjust the flow in the vicinity of a surface. Depending on the orientation of SDBD plasma actuator (PA) it can have different effects on the flow. If the grounded electrode is downstream of the charged electrode (Figure 1.3 (a)) then the time-averaged force acts to accelerate the flow in the downstream direction and towards the surface thereby delaying boundary layer separation. In the case where the grounded electrode is upstream of the exposed electrode (Fig-

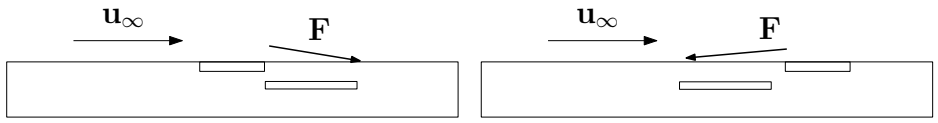

(a) Delaying boundary layer separation (b) Facilitating boundary layer separation

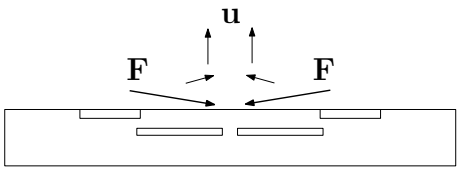

(c) Synthetic wall jet

Figure 1.3: SDBD PA effect on the flow.

ure 1.3 (b)) the time-averaged force acts in the upstream direction and could induce boundary layer separation. By placing two SDBD PAs facing toward each other (Figure 1.3 (c)) one can generate a synthetic jet away from the wall [6]. An interesting

effect can also be achieved by placing the actuator with the electrodes parallel to the flow. This positioning generates a vortex with its centre aligned with the flow. By changing the shape of the plasma actuator into a serpentine shape (Figure 1.1 (f)) one can combine the flow acceleration effect with the vortex generation [7].

1.3 Literature Review

Due to the presence of charged particles, plasma adds complexity to a numerical model due to plasma physics and thus increases the demand for computational resources. There are currently several methods that are used to simulate plasma actuators [8]. One is the phenomenological model, which estimates the body force on the fluid due to the presence of plasma within the electric field and uses CFD techniques to compute the rest of the flow. In certain cases this electric field is assumed and tuned based on experimental results. This provides a computationally inexpensive alternative to more time consuming and more accurate methods. To preserve some or all aspects of the plasma physics there are two main approaches: kinetic and fluid models. In the case of kinetic models the solutions are based on the kinetic equations of the particles and usually involve some statistical modelling of the particle interactions. Fluid models present the ions (either only positive or both positive and negative), electrons and neutral particles as different species mixed together. Due to the nature of the plasma and the different time scales between the motion of the neutral and charged particles, neutral particles are excluded from the calculations in certain cases (e.g. quiescent flow).

Kinetic and fluid models are better suited for understanding the mechanisms behind the aerodynamic effects that are produced by a plasma, while phenomenological models are advantageous for testing the implementation of a plasma actuator in a particular physical problem such as controlled vortex shedding on a wing.

1.3.1 Phenomenological models

Linear electric field model

The phenomenological model developed by Shyy [9] is used extensively due to its simplicity and ease of implementation. One of the more recent examples of its use is the implementation by Riherd and Ray [4] to model a serpentine configuration of a SDBD PA along a flat surface (Figure 1.1 (f)) for $Re_x = 50\,000$ and $M = 0.1$. The serpentine configuration results in the development of streamwise vortex flow. The structure of the vortex facilitates laminar-turbulent transition. This means that a serpentine PA configuration can be used as an active trip for initiating laminar to turbulent flow transition.

Cho and Shyy [10, 11] use the Shyy model to simulate a PA which is coupled to a control loop to modify the vortex shedding from a SD7003 airfoil at high angles of attack. The control loop is designed to take into account the uncertainty in the oncoming free-stream flow and produce an improvement in the lift coefficient of the airfoil at Reynolds numbers on the order of 1 000 with $V_\infty = 0.3\,m/s$. The results demonstrate a limited ability to control the lift coefficient through active vortex shedding induced by the SDBD PA. The authors conclude that the complexity of the flow with vortex shedding and reattachment requires additional study of the active flow control mechanism in near stall conditions to improve the effect of a PA.

Liu et al. [6] present numerical simulations of a "synthetic jet" created by a PA in both steady and unsteady modes of operation for quiescent flow using the Shyy model. In this case the PA (either two parallel actuators acting against each other or a single actuator in the form of a ring) directs the flow towards the center causing the flow to move away from the wall in the form of a jet (Figure 1.3 (c)) with an average speed of 0.28 m/s and a maximum speed of 1.1 m/s. The simulations of the unsteady operation of the PA produce a larger momentum flux as compared to steady

operation by as much as 10 %.

In another work, Zhang et al. [12] use a PA to prevent flow separation at a rounded trailing end of an elliptical NCCR 1510-7067N airfoil at $Re = 5.8 \cdot 10^6$ and $M = 0.12$. While the flow follows this rounded trailing edge (Coanda effect), the effect of the PA moves the separation point further away from the top surface improving the lift coefficient.

Suzen model

The model created by Suzen [13] is used by quite a few groups around the world. The work that directly involved Suzen includes the simulation of plasma flow control in a low-pressure turbine [14–16]. Reasor [15] presents a comparison of the implementation of the Suzen model for structured 2D (GHOST) and unstructured 3D (UNCLE) solvers in quiescent flow. The original work by Suzen is done using the GHOST solver, and as such it was limited to 2D cases. Reasor's work [15] is the next step towards 3D implementation of a SDBD PA model for more complicated flow analysis. The comparison of the velocity profiles along a flat surface indicates that the 3D solver is capable of producing similar results to the 2D solver. For these simulations Reasor used the following parameters: charge density ($\rho_{c_{max}}$) of 0.0075 C/m^3, Debye length (λ_D) of 0.17 mm, an applied voltage amplitude of 5 kV, and a voltage frequency of 4.5 kHz. These settings produce a wall jet with a maximum velocity of 1 m/s. Reasor also compares the velocity profiles generated by the 3D solver to experimental data obtained by Santhanakrishnan et al. [17]. While the profiles have similar shapes the locations of the maximum velocity are different. According to the simulation the location of the maximum horizontal velocity is 0.4 cm away from the trialling edge of the exposed electrode, while experimental data indicate that this maximum happens further downstream (1.6 cm). This is one of the indications that the Suzen model does not completely model all the effects of a SDBD PAs.

Dennis [16] uses Suzen's model for a flow separation control over a low pressure turbine Pak-B blade with chord length of 6.28 inches at a $Re = 5\,0000$ and a free-stream velocity of 5 m/s. The model's parameters λ_D and $\rho_{c_{max}}$ are tuned based on the quiescent flow from experimental results on a flat plate. The author demonstrates, using these simulations, the ability of a PA to delay flow separation on a Pak-B low pressure turbine blade and reduce the pressure coefficient on the suction side of the blade. The pressure coefficient profile, however, has noticeable differences between the simulations and experimental work, though the author attributes this to a slightly different PA configuration. With a higher value of λ_D a better agreement is achieved. This indicates that even after the tuning of the model for quiescent flow, additional adjustments to the model parameters are required as the configuration is changed. Overall this paper demonstrates that Suzen model allows one to simulate the flow separation control on a low pressure turbine. However, the model requires some fine tuning before it gives proper results.

Asada et al. [18] and Sato et al. [19] use the model created by Suzen to study the control of flow separation on a NACA 0015 airfoil with a SDBD PA operating in "burst mode" (also referred as "unsteady operation", "pulsating mode", or "non-continuous" operation of the actuator). Figure 1.4 shows the voltage profile for a burst mode of operation. The alternating voltage is applied to the exposed electrode only for a few cycles after which the voltage is set to zero for some period of time. The cycle is then repeated. Asada [18] presents results for $M = 0.2$, non-dimensional burst frequencies of $F^+ = 1$ and $F^+ = 6$ and two locations of the actuator: leading edge and 5 % chord length. The burst frequency is non-dimensionalised with the chord length and the free-stream velocity (1.1)

$$F^+ = \frac{f^+_{burst} c}{u_\infty} \tag{1.1}$$

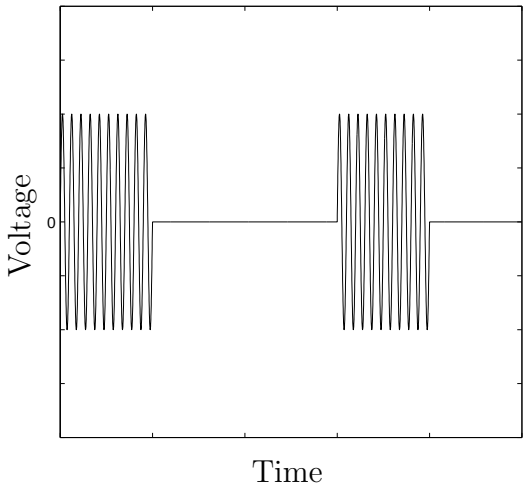

Figure 1.4: Operation of PA in burst mode.

where f^+_{burst} is the burst frequency, c is the chord length and u_∞ is the free-stream velocity. According to simulations, if the PA is located at the leading edge then at both tested frequencies large vortex shedding is prevented. In case of the 5 % chord location, the vortex shedding is suppressed only at $F^+ = 6$.

Sato et al. [19] make a comprehensive comparison with a variety of settings for different angles of attack, burst frequency, actuator position, plasma scale and actuator voltage frequency for the same configuration as presented by Asada et al. [18]. They conclude that the burst mode of operation for a PA can produce almost the same effect on the flow as continuous mode, while significantly reducing the required power input for the operation of the PA. The power reduction is directly proportional to the ratio between the on-off periods of the cycle. In addition, it is found that the most effective position of a PA for the prevention/delay of flow separation is in the vicinity of the separation point.

Kim and Wang [20] also use the model created by Suzen to study the effect of a PA and the number of these actuators on the flow and vortex shedding around a cylinder with $Re = 3\,0000$. An unsteady mode of operation is also studied. Results of this

work suggest that a mean drag reduction of 85 % can be achieved through the use of a steady PA. Suppression of large scale vortices by steady operation of the PA is also shown to reduce the fluctuation of the "lift" component of the force on the cylinder. The burst mode of operation produces similar results, however, the improvements in the drag reduction are lower. The authors hypothesize that the reason behind the difference is that in the case of the steady operation the vortex suppression is due to the momentum transfer to the flow, while in the case of the unsteady operation the PA modifies the shear-layer instability. The authors also analyse the flow using different numbers of actuators (two and four). According to the results the number of actuators has a significant effect on the steady mode of operation while burst mode is almost unaffected. In the case of steady flow the lower number of actuators is unable to prevent flow separation and vortex shedding. In the case of unsteady operation both configurations (with two and four PAs) produce similar flow features: suppression of large-scale vortex shedding and generation of small scale vortices. From this one can conclude that the burst mode of operation can provide significant improvements to the drag reduction at a fraction of the energy cost of a steady operation of PA.

A propeller with PA along the blade span is studied by Cheng et al. [21] using the Suzen model. Different rotation speeds (300 - 600 RPM), forward speeds (5 - 10 m/s) of the propeller and different locations of the PA are examined. The resulting maximum speed at the tip of the blade is 48 m/s for the case of 600 RPM and 10 m/s forward speed. The PA generally improves the efficiency of the propeller, but this improvement decreases with increased forward speed due to the increase in viscous forces. Another result of this work is that the effectiveness of the PA is increased at higher altitude due to lower pressure.

Lumped-Element Circuit model (LEC)

The lumped-element circuit model (LEC) developed by Orlov [22] provides a time based boundary condition for a PA computation, unlike the model described by Suzen where the charge distribution on the boundary is assumed to be Gaussian. The LEC method, however, is rarely used outside of Corke's group (Orlov was part of this group when developing the model). As a result there are a few authors who published their work with the use of LEC.

Mertz [23] compares the LEC and Suzen models and their variations for quiescent flow. The author tests the time averaged force produced by a SDBD PA and its variation with the maximum applied voltage. Mertz concludes that the LEC method without the electric potential splitting (as done by Suzen) produces better agreement with the experimental results. He then applies this model to a flow around a cylinder with diameter of 4 in at 6 m/s free-stream velocity and demonstrates that PA is able to suppress the vortex shedding process. For this simulation Mertz used a 11.5 kV peak voltage at 10 kHz (sine wave).

Orlov and Corke [24] demonstrate the effect of different voltages (5 - 20 kV peak voltage) and frequencies (3 - 20 kHz) on power dissipation and plasma extent using the LEC model. It is shown that the power depends on the voltage to the power of 3.5 ($\phi_E^{7/2}$) above 7 kV at 3 kHz. Orlov et al. [25] present the time-space plasma evolution for quiescent flow of a SDBD PA as computed with the LEC model in which the authors demonstrate a good agreement between experimental and the LEC model for the plasma time-space distribution. Orlov et al. [26] applies the LEC model for NACA0021 airfoil leading edge flow separation control with steady and unsteady actuator operation at 2.5 kV and 5 kHz within an air flow at $M = 0.1$. The unsteady operation of the PA is shown to perform better than steady operation by causing a larger delay in flow separation.

1.3.2 Fluid model

Fluid models of plasma are computationally more expensive than phenomenological models because of the need to model more than a single species. Due to that complexity these models are usually used for 1D or 2D, and rarely for 3D simulations. A SDBD PA is a good example of 2D or 3D plasma flow. 1D simulations on the other hand are usually used for cases where a large number of chemical reactions are present.

An example of a 1D model is the work done by Poggie et al. [2, 27]. The authors modelled the ionization process of air with 23 species (variations of molecular and atomic combinations of oxygen, nitrogen and electrons) and 50 chemical reaction mechanisms for a 12 ns pulse at different peak voltage settings (5 - 27 kV). This example does not involve a SDBD, but a nanosecond plasma discharge within a DDBD (Double Dielectric Barrier Discharge) mechanism (Figure 1.5). Nonetheless

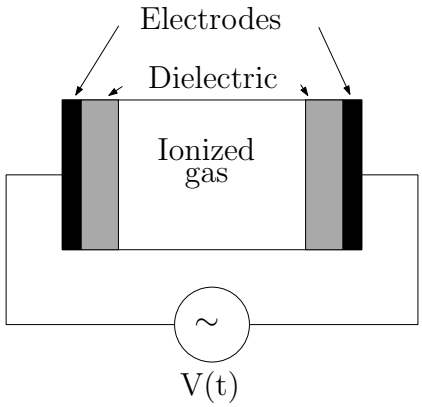

Figure 1.5: Schematic of DDBD plasma generator [2].

the governing equations are similar to those required for a SDBD PA simulation. In this paper the authors use a 1D simulation to test a plasma discharge for nanosecond plasma actuators at 4.74 kPa (36 Torr) and 310.3 K. According to the authors the results of the simulations agree reasonably well with the experimental measurements of the rise for translational and vibrational temperatures of nitrogen. One of the

conclusions is that the most significant chemical kinetics and particle dynamics occur near the sheath edge.

Roy et al. [4, 7, 28–35] also look into plasma discharge for various configurations of DBD mechanisms and different gas compositions. In [28, 29] Roy et al. reports on the simulations of a SDBD PA in quiescent helium environment at 300 torr (40 kPa), 1 kV peak voltage with a frequency of 5 kHz. In this work the authors found that during the positive part of the cycle the force is from the exposed electrode toward the encapsulated electrode, while during the negative part of the cycle most of the electrodynamic force is generated at the edge of the exposed electrode and directed toward this electrode. The force magnitude during the negative part of the cycle is smaller than during the positive part.

Another example of a SDBD simulation is described by Singh and Roy [31], where the authors simulate a helium plasma using electron and positive ion species in quiescent flow at 300 Torr, 300 K with peak voltage of 400 V at 5 kHz. One of the conclusions in this paper is that when the exposed electrode is charged positively the force is from the exposed to encapsulated electrode, while when the exposed electrode is negative the electrons cover the surface of the dielectric and become a virtual negative electrode shielding the enclosed ground electrode and therefore reducing the opposite force on the positive ions. In Singh et al. [32] a more complicated case than in Singh and Roy [31] is considered by introducing nitrogen and oxygen with 8 chemical reactions and 8 species (electrons, O_2, O_2^+, O, O^-, N_2, N_2^+, N). The simulations are performed with a gas density of 1.3 kg/m^3 and the peak voltage of 1 kV at 5 kHz frequency. The conclusion from this paper is that species of the same charge behave similarly in that they have similar density distribution profiles. Another result is that the time average force is in the direction from the exposed to enclosed electrodes. According to the paper the force in the streamwise direction is positive when voltage is positive, and negative during the negative part of the voltage cycle

(though the force magnitude is smaller than during the positive part of the cycle), with force peaks occurring at the peaks of the voltage cycles.

In Singh et al. [33] the authors present a simplified equation of force produced by a SDBD PA:

$$F = F_{x0}\phi_{E_0}^4 exp(-\{[x - x_0 - (y - y_0)]/y\}^2 - \beta_x(y - y_0)^2)\widehat{i} + F_{y0}\phi_{E_0}^4 exp(-\{-x_0]/y\}^2 - \beta_y(y - y_0)^2)\widehat{j} \quad (1.2)$$

All of the coefficients are curvefit based on previous work. The authors state that the above formula agrees well with more rigorous simulations using fluid models once all coefficients are tuned, paving way for a new phenomenological model.

Wang et al. [35] present the results for serpentine, square and triangular configurations of a PA using a two species (electrons and ions) fluid model 3D simulation in quiescent flow for a 9 kV peak voltage. Serpentine and square shaped PA configurations are shown to be very effective at generating streamwise vortical structures thus improving the mixing of the surrounding fluids. Wang et al. [7] present simulation results where a serpentine PA is used to improve flame stabilization. The plasma is modelled using a three species fluid model (positive and negative ions, and electrons). The combustion part of the simulation is independent of the plasma chemistry, such that the plasma has an effect only on the airflow and not the chemical kinetics. One of the main results described in this paper is that a serpentine PA enhances the air-fuel mixing as well as predicting better flame stabilization.

Shang and Huang [36] and Huang et al. [37] use a fluid model with electron and positive ion species to simulate the effect of a SDBD PA on a quiescent flow and the electrodynamic force produced by this device. Huang et al. [37] present an analysis of a full cycle of a simulated SDBD operation and compare this to experimental data for discharges at different peak voltages (2 - 4 kV) at 10 kHz. According to presented

results during the positive phase of the voltage cycle the body force is directed from the exposed electrode towards the encapsulated electrode, while during the negative part of the cycle the force is in the reverse direction. The magnitude of the force during the positive part of the cycle is higher than during the negative part, resulting in the time averaged force direction from exposed to enclosed electrode. According to the authors the concentration of ions close to the trailing edge the exposed electrode after the positive part of cycle reduces the effective electric field during the negative portion of the cycle and therefore the resulting electrodynamic force in the upstream direction. This results in higher electrodynamic force during the positive part of the cycle and lower electrodynamic force during the negative part of the cycle. Another result of this work is that ion density over the dielectric barrier has a half-Gaussian profile when the exposed electrode is positively charged. This supports the idea for the half-Gaussian distribution of charge density used in Suzen model.

The group of Miles, Shneider and Macheret from Princeton University has done a considerable amount of research into SDBD PAs and the use of plasma in aerodynamics [38–49]. Macheret et al. [38, 39] use a fluid model for 1D and 2D simulations of air ionization for a hypersonic intake and the use of Magneto-Hydro-Dynamics (MHD) for flow control at high speed using a magnetic field. The ionization process is performed using an electron beam which is computed using a Monte-Carlo simulation. This work continued with additional papers published in 2002 [42, 43]. In these papers the authors report the results of simulations for the use of MHD to decelerate the flow from Mach 6-8 conditions to transonic speeds with the help of electron beam ionization and a magnetic field. The magnetic field decelerates the flow through the Lorentz force acting on the charged particles. According to their results it is possible to convert between one-forth and one-third of the total flow enthalpy into electricity and to bring down the total temperature to 1 000 K. The total temperature at Mach 8 is approximately 3 600 K (assuming a static temperature of 260 K), which

indicates a significant temperature reduction and possible reduction to the intake material requirements. Parent et al. [46] present result similar to the 2002 papers with the addition of a chemical model for air and plasma as 8 species (molecular and atomic oxygen and nitrogen, their ions and electrons) and 28 reaction mechanisms. While these papers do not deal with PAs, they demonstrate the use fluid models for the plasma aerodynamic computations and the complexity of the problems that can be resolved using these models.

Likhanski et al. [45,47] present the simulation of a flow generated by a PA using a 2D fluid model for the plasma in the absence of free-stream flow for atmospheric air with the PA operating at 1.5 kV and 1 MHz. According to Likhanskii et al. [45] the force generated by a PA is positive during positive and negative parts of the cycle. During the negative part of the cycle the electrons are deposited on the dielectric on top of the encapsulated electrode generating a "virtual electrode" which pulls the positive ions, while during the positive part of the cycle the positive ions are repelled by the positively charged exposed electrode. There are two sources of inefficiency to these motions: the negative ions move in the opposite direction to the positive ions and during the negative part of the cycle the positive ions are attracted towards the negatively charged exposed electrode. An interesting SDBD PA configuration is presented by Starikovskiy and Miles [49], where a semiconductor is added to the dielectric surface. The purpose of the semiconductor is to allow the flow of charge during the backstroke through it, therefore reducing the upstream force on the plasma and improving the efficiency of the device.

Boeuf and Pitchford [50] also worked on SDBD PAs and simulated a SDBD PA using a two species model (electrons and positive ions). In this work, the authors present the results of a simulation with constant voltage pulses of 1.2 - 1.8 kV at 1 kHz in a quiescent nitrogen flow at atmospheric pressure. For this configuration they notice that the force on the particles only acts on a limited region (sheath, 50 μm

wide) which moves at 3 - 5 $mm/\mu s$. The authors also notice that the horizontal force component is lower during the negative voltage part of the cycle.

In Shang [51] the simulation of a SDBD PA at 5 Torr in an electric field of 2.4 kV peak at 10 kHz is presented. The author concludes that the force on the flow is concentrated in a thin layer along the dielectric above the encapsulated electrode which corresponds to the statements by other authors presented above (e.g. [37, 50]).

At Seoul National University, Lee et al. [52] use the fluid model to analyse the type of discharge for a DBD device in helium-oxygen mixtures at 1 atm, 1.5 kV, 5 - 35 kHz with different oxygen concentration (5 - 40 ppm). Depending on the concentration of oxygen molecules in the mixture the type of discharge changes between the glow discharge and Townsend discharge. The Townsend discharge (or Townsend avalanche) is the cascade reaction in which a free electron ionizes a neutral atom/molecule and then gains enough energy from an electric field to cause another ionization upon the next collision with the next atom/molecule. The released electrons from these ionization processes also gain enough energy to ionize additional atoms/molecules therefore causing a chain ionization reaction. The level of ionization in a Townsend discharge is very small and no noticeable light is emitted. At higher levels of ionization and currents the frequency of electron-ion or electron-neutral collisions is increased and so is the number of ion-electron recombinations causing a larger number of photons to be released and thus the plasma starts to glow (i.e. a glow discharge). The authors use the Boltzmann equation to obtain an electron energy distribution function, from which they obtain the electron mobility (Eq. 2.26). The results of these simulations indicate that the glow discharge mode can be achieved by either lowering the concentration of oxygen in the mixture or by increasing the driving frequency. According to these results the maximum oxygen concentration to sustain the glow mode is approximately 25 ppm at 20 kHz. The authors also concluded that the glow discharge mode has a higher electron density and stronger electric field than the Townsend mode,

therefore making glow discharge more effective for the plasma treatment and processing. This work does not deal with the aerodynamic application of PAs, nonetheless it demonstrates the application of the fluid model for the plasma simulations and also demonstrates the importance of oxygen molecules in the plasma discharge.

Shi et al. [53] studied DBD discharge effects on a laminar incompressible flow under a sinusoidal applied voltage using a variation of a fluid model. In this model they do not compute the distribution of charged particles, instead, the charge continuity is solved under simplified boundary conditions. The applied voltage is a sinusoidal wave with an amplitude ranging from 14 kV and 22 kV and with frequencies of 0.5, 1 and 2 kHz. The simulations were performed using COMSOL software. The authors analysed the boundary layer changes due to DBD effects.

Nakano et al. [54] performed experiments and simulations on a Dual-Grounded Tri-Electrode Plasma Actuator (DGTEPA). In this case DGTEPA is a DBD PA with an additional grounded electrode located on top of the exposed electrode. In this configuration there is an additional source of initial ionization. Nakano experimented with a 10 kHz sine wave with a voltage peak from 2.5 to 6 kV. These results were compared to DBD PA. According to Nakano in the cases with a voltage amplitude above 3 kV a DGTEPA performs better than a DBD PA. The thrust generated by a DGTEPA is about three times higher than for a DBD PA, while the generated jet becomes thicker and the peak velocity increases by about 10 %. The simulations were performed with a three species (positive, negative ions and electrons) fluid model. The simulations concentrated on the force generated by PA, the heat, associated with plasma, was neglected.

1.3.3 Kinetic model

The most computationally expensive methods out of the ones discussed are the kinetic models. This type of model is widely used for simulations of rarefied plasma. However,

non-equilibrium plasma at atmospheric pressures requires a large number of particles and thus longer simulated times thereby limiting the use of these models.

Font is one of a few researches to make use of a kinetic model to simulate a SDBD PA [55–58]. In his work Font uses Particle-In-Cell Direct-Simulation-Monte-Carlo (PIC-DSMC) simulations to compute the body force produced on particles while the velocity of the neutral particles is ignored. Font [55] initially presents the results for nitrogen gas at atmospheric pressure using a square wave voltage pattern with a peak at 5 kV and an effective frequency in the range of 1 - 10 MHz. Later he introduces another simulation with oxygen [56] with all other parameters remaining the same. The simulation results are compared to experimental data for both pure oxygen and pure nitrogen. It is shown that the slope of the force versus the applied voltage from the simulation is too steep, while the trend and order of magnitude is correct for both oxygen and nitrogen simulations. The author relates the difference in slopes to possible accumulation of metastable plasma products, which are not included in the simulations. In the subsequent work by Font et al. [57] the force is computed using the PIC-DSMC and fed into FLUENT solver as a body force on the flow which results in initial vortex flow. From all these analyses [55–57], Font concludes that there are regions of spatially non-neutral plasma where positive ion density exceeds that of electrons. The location and intensity of the charge density within these regions is different depending on the direction of the electric field. This results in different magnitudes of the force on the particles during the negative and positive parts of the applied voltage cycle. Font states that the force in the upstream direction is 10 times smaller than in the downstream direction. Another observation is that oxygen has a higher level of ionization (as opposed to pure nitrogen) and produces negative ions. Even though the negative ions are present their concentration is smaller than that of the positive ions and thus the overall force is still in the forward direction.

In Font et al. [58] additional comparisons of kinetic model results to fluid model

results and experiments are presented. The two models predict higher ionization of the gas during the positive part of the cycle, both predict regions dominated by ions, and both predict the time averaged force in the direction from the exposed electrode towards the encapsulated electrode. However, there are a few differences. For example, the fluid model predicts a larger spread of plasma than the kinetic model which the authors relate to the so called seeding particles required to initialize the kinetic models. Based on the experimental force measurements a plasma density can be estimated which matches that from the fluid model. Based on a measured plasma resistivity an electron density can be estimated which agrees well with kinetic model. The authors state that it is possible that the plasma operates in both the Townsend type breakdown and glow discharge. Comparison to a capacitive V-dot probe voltage measurement showed the following. At a distance of x/d = 0.96 (d is the dielectric thickness and x is the distance from the exposed electrode) the dielectric surface is charged to +2 kV (positive part of the cycle) and -5 kV (negative part of the cycle) irrespective of the applied voltage amplitude (6 kV, 8 kV, 10 kV). This results in the field strength of 0.5 MV/m (positive part of the cycle) and 1.2 MV/m (negative part of the cycle) which is consistent with the kinetic model simulations.

Another example of the use of the kinetic model to simulate a SDBD is presented by Huerta and Ludeking [59]. This work is similar to that of Font [55] and Font et al. [56] except that the gas is argon. It is concluded that while it is possible to perform SDBD simulations using PIC-DSMC, the computational resources required are considerably more demanding than for the fluid models. Additionally, many collision cross sections required for the PIC simulations are not well known, as opposed to the ionization and reaction rates variables needed for fluid models which are better known.

1.3.4 Other models

It is also possible to calculate a body force distribution from the Navier-Stokes equations based on experimentally measured velocity fields. An example of this is the work done by Kotsonis et al. [60, 61]. Kotsonis and Ghaemi [60] present experimental and simulation results for continuous and unsteady modes of operation of a PA. The body force is obtained from PIV measurements of continuous operation of an actuator in quiescent flow which is then fed into a Navier-Stokes solver (OpenFOAM). Simulations agree reasonably well with the experiment showing it is possible to extract the proper body force from the PIV measurements. However, the force extracted from the measurements for quiescent flow does not guarantee the same body force for conditions with external flow. In Kotsonis et al. [61] the results of the use of a PA for control of boundary layer instabilities (Tollmien-Schlichting waves) and laminar-turbulent transition are presented. Again the body force is obtained from experimental measurements and fed into simulation software. This work shows the ability of a PA to suppress boundary layer instabilities and therefore delay a boundary layer separation.

A model specifically designed for nanosecond DBD (NSDBD) actuator operation has also been used by several researchers. Unlike SDBD PAs which operate with alternating voltage in the kHz frequency range, NSDBD actuators operate in pulses with a duration of 1 - 10 ns with milliseconds in between the pulses. Geometry wise NSDBD PAs can be identical to SDBD PAs. A NSDBD PA does not operate long enough to transfer significant momentum as done by a SDBD PA under an alternating voltage, yet NSDBD PAs are still capable of preventing flow separation. It is thought that the main mechanism through which a NSDBD transfers energy to the flow is through Joule heating which causes compression waves to form [62]. As a result, a NSDBD PA can be modelled as a heating element. Gaitonde et al. [62] present the

results of a Large Eddy Simulation of a NACA0015 airfoil at a $Re = 100\,000$ and a free-stream velocity of 15 m/s using NSDBD PA heating element model. The authors demonstrate stall prevention characteristics using a NSDBD PA and show that the NSDBD PA trips the flow creating an attached turbulent boundary layer.

Zheng et al. [63] analysed the effects of NSDBD on shock structure using "self-similar" plasma model which estimates the thermal energy deposited by electric field into flow field. Zheng examined the effect that the NSDBD plasma actuator has on shock structure generated by an object flying at Mach numbers above 4. According to their findings it possible to move a bow shock further away from a blunt body by using a NSDBD on the surface of that body. In addition Zheng proposed that it is possible to adjust the flight trajectory of a projectile by modifying a shock structure generated by the cone of the projectile. The simulations indicated that by introducing a nano-second discharge on a wedge behind the shock one could generate a shockwave at the point of discharge which will interact with the initial shock structure generating a force normal to the direction of the flight.

1.4 High speed experiments

Most simulations of SDBD PAs presented in the literature deal with subsonic incompressible and in many cases quiescent flow, while the simulations of SDBD PAs in supersonic flow are fewer (e.g. the work by Shneider and Macheret [38–44]). The application of plasma for supersonic flow and/or shock control is currently being tested though a number of experiments. However, many of these tests use PAs other than SDBD.

Webb et al. [64] describes experimental results for the use of Localized Arc Filament Plasma Actuators (LAFPA) to control the location of a reflected shock for a free-stream flow with $M = 2.3$. The authors observe that the LAFPA placed upstream

of the reflected shock moves the shock upstream by approximately one boundary layer thickness. This is thought to be caused by heating of the upstream boundary layer by the PA.

Pavon et al. [65] discuss the effect of DBD PAs on a shock generated by a NACA 3506 airfoil at transonic speeds. For this airfoil shocks are observed for Mach numbers as low as 0.65 - 0.75. According to the results, the PA has no noticeable effect on either shock structure or pressure distribution across the shock. However, the shock facilitates the generation of high current filaments in the plasma region which usually occur at higher voltages.

Nishihara et al. [3] present the results of an experiment in which a PA is used to effect the shock wave created by a shock generator (a 12° or 22° ramp located at the walls of a wind tunnel) in a supersonic wind tunnel with the flow at M = 3. The shock is then reflected from the wall on the opposite side of the tunnel. Two SDBD PA locations are considered:

- the entire PA is completely behind the shock on the ramp with the grounded electrode being upstream of the exposed electrode,
- the grounded (encapsulated) electrode is in front of the ramp and ramp-generated oblique shock, while the exposed electrode is on the surface of the ramp behind the shock.

In both cases the expected force is upstream. The PA operates at 17 kV with triangular pulses at 1 kHz. The working fluid is air at 400 torr total pressure. According to the results in the first case, the PA generates a compression wave of its own which moves away from the PA and disturbs the oblique shock wave. In the second case, the PA generates an oblique shock upstream of the ramp which in turn reduces the strength of the ramp shock. This configuration also causes perturbations to the ramp shock similar to the first configuration. These perturbations are also transmitted to

the reflected shock and the separation bubble that is formed at the wall due to the shock-boundary-layer interaction.

Leonov et al. [66] experimentally analysed the effect of plasma discharge on supersonic flow ($M = 2$) along a flat plate with further applications to blunt and streamlined geometries. The plasma in this case is generated using exposed electrodes at constant voltage (5 kV). This type of plasma generator generates filaments between the electrodes that move with the flow until filament breakdown and a new filament is generated. The typical gas temperature within the filament is on the order of 3 000 K. In this case the plasma has the same effect on the flow as a ramp which creates an oblique shock. The angles of this virtual ramp and resultant shock depend on the electrical power released by the plasma generator. This virtual ramp can be used to reduce the drag on an obstacle downstream of the plasma generator with varying degrees of efficiency depending on the obstacle geometry. The effectiveness is lower for a streamlined obstacle and higher for a blunt obstacle. The drag reduction for blunt cases can reach as high as 5 %. Leonov et al. also present a model for the angle and position of the oblique shock generated by the plasma as well as the temperature of the gas in the heated layer.

Similar to Gaitonde et al. [62], Sun et al. [67] use the heating element model to numerically model the effect of plasma on the flow, except in this case experimental and numerical simulations are presented for a supersonic flow. The flow is at a static pressure of 2 813 Pa and a static temperature of 105 K with a Mach number of 3. The authors analysed two types of actuation: millisecond discharge (modelled as steady state) and microsecond discharge for a flow along a flat plate. In the case of millisecond discharge or nearly continuous discharge an oblique shock is observed at the plasma region location. In addition, the boundary layer thickness is increased. In the case of a microsecond discharge the plasma generator creates compression waves travelling away from the generator in a radial direction. The authors also

test the plasma generator at the base of a 25° ramp. It is shown that the plasma causes an oblique shock in front of the ramp and reduces the overall pressure drop for a location on the ramp downstream of the shock. Another application of the microsecond plasma actuation tested by Sun et al. is the effect of the flow separation at the base of a reflected shock. The test is performed for an incoming 32° oblique shock. The application of a plasma shows an increase in the static pressure ratio from 2.2 to 2.8 after the reflection shock. In addition, the separation area after the shock is reduced.

Wang et al. [68] performed experiments to analyse the possible effects that a Counter-flow Plasma Synthetic Jet Actuator (CPSJA) could have on a bow shock generated by a blunt object within a supersonic flow field. The free stream Mach number of the flow was set to 2. In addition, the data was compared to simulation results. Unlike DBDPA, CPSJA is a cavity that uses high current pulses to heat the gas inside the cavity, which in turn generates high pressure pulsating jet, which in this case was directed against the direction of the flow. The currents that generate the plasma are 29 A to 84 A for a 2 mm cavity with a pulse duration of approximately 10 μs. The study showed that it is possible to suppress the step-induced separation region located downstream of the blunt body.

1.5 Current Work

As mentioned in the previous sections SDBD PAs are studied extensively throughout the world. SDBD PAs are capable of drag reduction, flow separation control and control of vortex shedding. These are shown through numerous computations and supported by experimental data. However, the computations of SDBD PA are mostly limited to subsonic flows. The use of PAs for flow control at supersonic speeds is tested mostly using experimental approaches with very few numerical simulations.

However, as experiments show, PAs can have a profound effect on the flow at supersonic speeds resulting in shock wave control and drag reduction. Since computational studies are usually a faster and cheaper alternative to experiments, it can be important to develop a methodology for supersonic flow computations in presence of plasma. While the phenomenological models are capable of providing acceptable force approximation for the flow, these models still require fine tuning or experimental constants for a given case and the currently available variety are not tested for supersonic flows (with the exception of the heating element model). The kinetic models are computationally too expensive to be feasible for the simulations of supersonic flow within an atmosphere. The fluid models on the other hand are capable of producing good results without experimental data from specific configurations, though validation is still needed. This means that the fluid models are the most viable candidates for fundamental simulations of SDBD PA at supersonic speeds.

The aim of this work is to develop a CFD code for compressible flow simulations that is capable of plasma computations. In addition this work is trying to answer two questions with regards to supersonic flow - plasma interactions:

- What effects does a shock have on a plasma generated by a SDBD PA?
- What effects does a SDBD PA have on a shock in supersonic flow?

To answer these questions an OpenFOAM solver is developed and tested first at quiescent (or frozen) flow conditions and then at supersonic flow conditions. Once the code is developed it could be further used to test additional ideas for airflow control at supersonic speeds and designs of supersonic aircraft and engines.

Chapter 2

Computational Model

The software used for this work is OpenFOAM [69]. OpenFOAM is a program that contains differential equation solvers and is mainly aimed at fluid dynamics problems. It is written in C++ and it is open source, hence it's relatively easy to modify and create one's own solver. All tested geometries presented in this work consist of gas and dielectric regions (Figure 2.1) which have different sets of equations. Some of these equations have to be coupled across these two regions. The newly developed solver

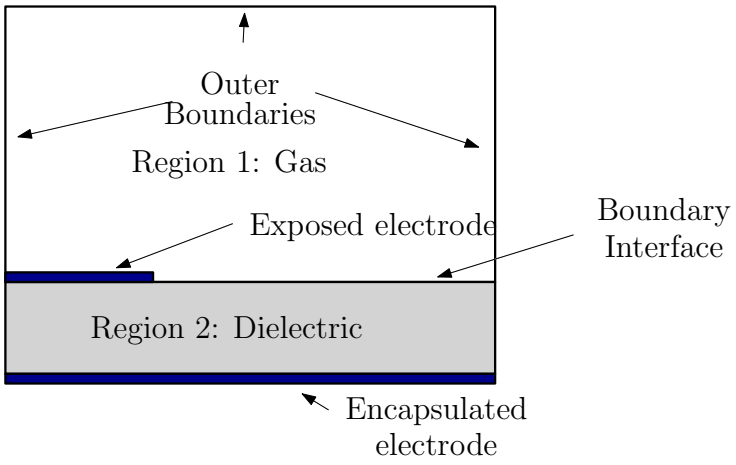

Figure 2.1: Computation domain for OpenFOAM simulations.

for this analysis is based on a combination of a conjugate heat transfer with multiple regions (chtMultiRegionFoam) solver and a supersonic (sonicFoam) solver. Due to the simplicity of the geometries the meshing is done using blockMesh in OpenFOAM.

The following is an overview of the model as implemented in OpenFOAM.

2.1 Governing equations

In this work the effects of a plasma on supersonic flow and vice-versa are examined so the use of compressible flow equations is required. An assumption is made that the level of ionization is relatively low and therefore the number of ions is much lower than the number of neutral particles. Based on this assumption the compressible flow equations are written only for a single neutral species. Eq. 2.1 represents the Navier-Stokes equations for a compressible flow with a body force $\mathbf{f}_E$. The effect of the electrostatic force ($\mathbf{f}_E$) on the bulk flow is modelled through this force term while other possible body forces are neglected (e.g. gravity). The computation of this term is described later in this section.

$$\frac{\partial \rho \mathbf{V}}{\partial t} + \nabla \cdot (\rho \mathbf{V} \times \mathbf{V}) - \left(\mu \nabla^2 \mathbf{V} + \frac{1}{3} \mu \nabla (\nabla \cdot \mathbf{V}) \right) = -\nabla p + \mathbf{f}_E \tag{2.1}$$

The viscosity term (μ) is computed using the Sutherland model (Eq. 2.2) for nitrogen with the Sutherland coefficient (A_s) set to $1.4067 \cdot 10^{-6}\ Pa \cdot s$ and the Sutherland temperature (T_s) set to 111 K.

$$\mu = \frac{A_s \sqrt{T}}{1 + T_s/T} \tag{2.2}$$

The continuity equation for a compressible flow is

$$\frac{\partial \rho}{\partial t} + \nabla \cdot (\rho \mathbf{V}) = 0 \tag{2.3}$$

The energy equation, written in terms of the specific internal (u) and specific

kinetic ($0.5V^2$) energy, can be expressed as ($\left[\frac{J/s}{m^3}\right]$)

$$\frac{\partial \rho u}{\partial t} + \nabla \cdot (\rho u \mathbf{V}) + 0.5\frac{\partial \rho V^2}{\partial t} + 0.5\nabla \cdot (\rho V^2 \mathbf{V}) + \nabla \cdot (p\mathbf{V}) - \nabla^2(\alpha_{eff} u) = \mathbf{f}_E \cdot \mathbf{V} + q_{th} \quad (2.4)$$

The potential energy is considered negligible for the cases analysed in this work. The term $\mathbf{f}_E \cdot \mathbf{V}$ is the work done by the electric field on the flow and q_{th} is the heating of the flow due to the ionization related processes. The term α_{eff} is the sum of laminar and turbulent thermal diffusivity as computed by OpenFOAM. In the cases considered here the turbulence model is set to laminar therefore α_{eff} is defined as

$$\alpha_{lam} = \frac{\kappa}{\rho c_p} \quad (2.5)$$

where κ for the Sutherland model in OpenFOAM is computed as

$$\kappa = \mu c_v (1.32 + 1.77\frac{R}{c_v}) \quad (2.6)$$

The internal energy (u) is computed from

$$u = c_v T \quad (2.7)$$

where c_p and c_v are the specific heat capacities at constant pressure and constant volume, and are assumed to be constant at values of 1040 J/kgK and 743 J/kgK for N_2 over the range of temperatures considered.

2.1.1 Computations of the electrostatic force and electric field

As mentioned in the previous section, one of the ways the plasma affects the bulk flow is through the Lorentz force $\mathbf{f}_E$ and is generally defined as

$$\mathbf{f}_E = \rho_c \mathbf{E} + \mathbf{J} \times \mathbf{B} \tag{2.8}$$

where ρ_c is the volumetric charge density and will be discussed later, $\mathbf{E}$ is the electric field, $\mathbf{J}$ is the current density and $\mathbf{B}$ is the magnetic field. In order to find the electric and magnetic fields one needs to solve Maxwell's equations. For the cases studied here, the applied magnetic field is zero while the induced magnetic field is assumed to be negligible due to the relatively small currents, which allows the $\mathbf{B}$ term to be neglected.

Eq. 2.9 is the mathematical formulation of Ampere's law,

$$\nabla \times \mathbf{B} = \mu_B \mathbf{J} + \frac{1}{c^2} \frac{\partial \mathbf{E}}{\partial t} \tag{2.9}$$

where μ_B is the vacuum permeability and is equal to $4\pi 10^{-7}$ H/m, while c is the speed of light in a vacuum and approximately equal to $3 \cdot 10^8$ m/s. As can be seen by the magnitude of the terms on the right of Eq. 2.9, the induced magnetic field by either $\mathbf{J}$ or $\mathbf{E}$ can be neglected when these terms are small.

The Maxwell-Faraday equation relates any time varying magnetic field to the spatial variation in electric field as shown in Eq. 2.10. However, in the absence of a time varying magnetic field it can be simplified to Eq. 2.11

$$\nabla \times \mathbf{E} = -\frac{\partial B}{\partial t} \tag{2.10}$$

$$\nabla \times \mathbf{E} = 0 \tag{2.11}$$

Gauss's law for magnetism (Eq. 2.12) that deals with the divergence of the magnetic field can be neglected due to the absence of an applied magnetic field and negligible induced magnetic field thus,

$$\nabla \cdot \mathbf{B} = 0 \tag{2.12}$$

The last of Maxwell's equations to consider is the Gauss law that relates the charge distribution to the resulting electric field. In the fluid region with plasma, free charges are present hence one must solve Eq. 2.13 due to a non-zero value of ρ_c. In the dielectric region, which is modelled as non-conductive solid and hence maintains its original charge $\rho_c = 0$, Eq. 2.13 is simplified to Eq. 2.14.

$$\nabla \cdot \mathbf{E} = \frac{\rho_c}{\epsilon} \tag{2.13}$$

$$\nabla \cdot \mathbf{E} = 0 \tag{2.14}$$

The permittivity, ϵ in Eq. 2.13 is convenient to present as a product of relative permittivity (ϵ_r) and vacuum permittivity ($\epsilon_o = 8.85 \cdot 10^{-12}$ F/m) as shown in Eq. 2.15,

$$\epsilon = \epsilon_r \epsilon_o \tag{2.15}$$

For the numerical computations the electric field ($\mathbf{E}$) is calculated by solving for the electric potential (ϕ_E). The two are related through Eq. 2.16.

$$\mathbf{E} = -\nabla \phi_E \tag{2.16}$$

Using the above correlation within the Gauss Law in Eq. 2.13 yields Eq. 2.17 in the

fluid region with plasma and Eq. 2.18 everywhere else.

$$\nabla \cdot (\epsilon \nabla \phi_E) = -\rho_c \tag{2.17}$$

$$\nabla \cdot (\epsilon \nabla \phi_E) = 0 \tag{2.18}$$

In the absence of a magnetic field (applied or induced) the Lorentz force (Eq. 2.8) is reduced to Eq. 2.19.

$$\mathbf{f}_E = \rho_c \mathbf{E} \tag{2.19}$$

with both terms on the right hand side related through Eq. 2.17. Therefore, one still needs to find the charge density distribution (ρ_c), which leads to Section 2.1.2.

2.1.2 Charge density computations (ρ_c)

The charge density comes from the summation of the charge densities of all charged species as shown in Eq. 2.20

$$\rho_c = e_o \sum_k s_k N_k \tag{2.20}$$

where s_k is the charge sign: for electrons it is -1 and for positive ions it is $+1$ (assuming no higher order ions are present); e_o is the elementary charge and is equal to approximately $1.602 \cdot 10^{-19}$ C and N_k is the number density of species k (e.g. electron and positive ion).

The charged particle densities (N_k) are found from continuity equations for each species:

$$\frac{\partial N_k}{\partial t} + \nabla \cdot \mathbf{\Gamma}_k = S_k \tag{2.21}$$

where the source term S_k depends on the type of species and the ionization model

used. The flux of the charged particles ($\mathbf{\Gamma}_k \left[\frac{particles}{m^2 s}\right]$ is defined as

$$\mathbf{\Gamma}_k = N_k \mathbf{V} + s_k \mu_k \mathbf{E} N_k - D_k \nabla N_k \tag{2.22}$$

This equation includes the effect of the bulk flow on the transport of charged species ($N_k \mathbf{V}$), the movement of charged species due to an applied electric field ($s_k \mu_k \mathbf{E} N_k$) and the diffusion of the charged species ($D_k \nabla N_k$). The diffusion coefficient D_k can be computed from

$$D_k = \frac{\mu_k k_B T_k}{e_o} \tag{2.23}$$

where μ_k is particle mobility (which depends on the type of particle, the medium density and electric field strength), k_B is the Boltzmann constant and is approximately equal to $1.3806 \cdot 10^{-23}$ J/K and T_k is the temperature in Kelvin.

When values for k_b and e_o are substituted into Eq. 2.23, then assuming an ion temperature of 116 K and an electron temperature of 11600 K one obtains Eqs. 2.24 and 2.25, respectively (which are consistent with the values used by Boeuf [50] for N_2),

$$D_i = 0.01 \mu_i \tag{2.24}$$

and

$$D_e = 1 \mu_e \tag{2.25}$$

The value for the electron mobility is based on the electron drift velocity (V_{dr_e}) (Eq. 2.26),

$$\mu_e = V_{dr_e} / E \tag{2.26}$$

The drift velocity of electrons in nitrogen gas is calculated from Eq. 2.27 which is a

curve fit in m/s based on the data from [70].

$$V_{dr_e} = (E/N)^{0.69813} e^{42.267} (1 + (E/N)^{-0.66345} e^{-33.703}) \tag{2.27}$$

The data for the drift velocity is shown in Figure 2.2.

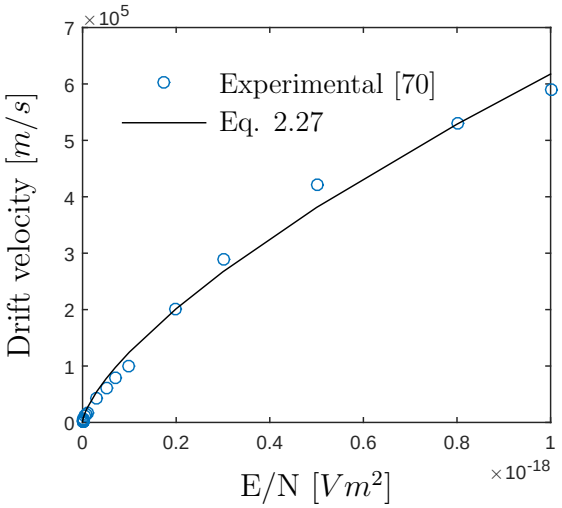

Figure 2.2: Electron drift velocity in N_2.

Combining Eqs 2.26 and 2.27 yields for the electron mobility, μ_e

$$\mu_e = \frac{(E/N)^{0.69813} e^{42.267} (1 + (E/N)^{-0.66345} e^{-33.703})}{E} \tag{2.28}$$

while the ion mobility for positive ions of N_2 is taken from [71],

$$\mu_i = 1.8 \cdot 10^{-4} \cdot 2.69 \cdot 10^{25} / N_{tot} = 1.8 \cdot 10^{-4} \cdot 2.69 \cdot 10^{25} \frac{k_B T}{p} \tag{2.29}$$

where in both Eqs. 2.28 and 2.29 the units of mobility are $\frac{m^2}{Vs}$.

At this point the solution for charge density still requires the computation of the source terms (S_k) for every species. These parameters depend on the gas and the plasma model used within the simulations.

To solve for the source term (S_k) in Eq. 2.21 all cases considered in this work

model the fluid as nitrogen gas. While ionization is a process which consists of multiple reactions and many variations of molecular/atomic states (e.g. different levels of ionization, excitations, etc.), the current model consists of only electrons, positive ions and neutral particles of diatomic nitrogen (N_2). This simplifies the reactions to a single ionization - recombination set. This reaction can be written as

$$e^- + N_2 \rightleftharpoons 2e^- + N_2^+ \tag{2.30}$$

This reaction represents ionization of diatomic nitrogen through electron impact when the electric field is sufficiently strong to give free electrons enough energy to ionize an N_2 particle during impact and the reverse process of electron - positive ion recombination otherwise. In the forward direction for every positive ion within the plasma that is generated, a newly generated electron is also produced (while in the opposite direction, for every positive ion consumed, one electron is also consumed). Therefore the source terms for both electrons and positive ions are equal and can be expressed in the following form,

$$S_k = S_p = S_e = \alpha|\mathbf{\Gamma}_e| - \beta N_e N_p \tag{2.31}$$

where the ionization reaction ($\alpha|\mathbf{\Gamma}_e|$) depends on the number of electrons impacting a neutral particle and is represented by the product of Γ_e an ionization coefficient (α) for N_2 which is found from Eq. 2.32 in units of $[m^{-1}]$ (taken from [72]).

$$\alpha \quad = \quad \begin{cases} 8.8 \cdot 0.750 p e^{\frac{-27500}{1.333E/p}} & if \quad E/p < 150 \cdot 1.333 \\ 12 \cdot 0.750 p e^{\frac{-34200}{1.333E/p}} & if \quad E/p > 150 \cdot 1.333 \end{cases} \tag{2.32}$$

where E/p is in units of $\frac{V/m}{Pa}$. The recombination reaction ($\beta N_e N_p$) depends on the number of both electrons (N_e) and positive ions (N_p) and a recombination coefficient

$\beta \left[\frac{m^3}{s}\right]$ (taken from [50, 73])

$$\beta = 1 \cdot 10^{-13} \tag{2.33}$$

2.1.3 Thermal energy computations (q_{th})

The term q_{th} in Eq. 2.4 represents the heat generated within a plasma. The model for computing this value is taken from the work of Abdollahzadeh et al [73], where q_{th} consists of the heat generated by ions and electrons,

$$q_{th} = q_{th_{ions}} + q_{th_e} \tag{2.34}$$

The first $q_{th_{ions}}$ is the Joule heating due to ion currents (J_p) and can be found directly from

$$q_{th_{ions}} = \mathbf{J}_p \cdot \mathbf{E} \tag{2.35}$$

where the positive ion current J_p is defined as

$$\mathbf{J}_p = e_o \mathbf{\Gamma}_p \tag{2.36}$$

and $\mathbf{\Gamma}_p$ is defined by Eq. 2.22.

One could also apply the Joule heating due to electron current directly and use q_{th_e} as found from an expression similar to Eq. 2.35. In this case one would assume that all of the heating is instantaneous.

$$q_{th_e} = \mathbf{J}_e \cdot \mathbf{E} \tag{2.37}$$

where J_e is the current due to the electrons:

$$\mathbf{J}_e = -e_o \mathbf{\Gamma}_e \tag{2.38}$$

However, the heating due to electron current is not as straight forward as that due to ionic current as outlined by different authors [74–76]. Therefore, q_{th_e} in Eq. 2.39 is used which consists of three parts.

When an electron impacts a neutral particle it may increase the random translational motion and/or the rotational motion of the neutral particle as represented by the term $q_{trans/rot}$. However, this collision may also change the orbital state of the electrons within the neutral particle without actually ionizing the neutral particle and thus this energy is represented by q_{orbit}. In addition to changes in the electronic state, a collision may also change the vibrational energy of a neutral particle as represented by q_{vib}. Summing all of these effects yields

$$q_{th_e} = q_{trans/rot} + q_{orbit} + q_{vib} \tag{2.39}$$

The translational/rotational energy is calculated using

$$q_{trans/rot} = \eta_1(\mathbf{J}_e \cdot \mathbf{E}) \tag{2.40}$$

where η_1 is found from

$$\eta_1 = 2.07278 \times 10^{-2} e^{-2.6180|\frac{E}{N}|} + 4.04597 \times 10^{-2} e^{-174.46|\frac{E}{N}|} + 0.168412 e^{-7131.03|\frac{E}{N}|} + 2.98161 \times 10^{-3} \tag{2.41}$$

and E/N has units of Vm^2.

The term q_{orbit} is found from

$$q_{orbit} = \xi\eta_2(\mathbf{J}_e \cdot \mathbf{E}) \tag{2.42}$$

where η_2 is found from

$$\eta_2 = 0.1348001e^{-3.5410|\frac{E}{N}|} - 0.97065e^{-0.202042|\frac{E}{N}|} + 0.414522e^{-2.63147\times10^{-3}|\frac{E}{N}|} + 0.4507497 \quad (2.43)$$

and the factor ξ is assumed to be 30 % (thus only 30 % of this energy is converted into a sensible gain in the bulk flow specific internal energy).

Equations 2.41 and 2.43 are taken from [73] and written in terms of $\frac{E}{N}$ in Townsend units (1 Td = 10^{-21} Vm^2).

The vibrational excitation heating is found from the solution to the equation

$$\frac{\partial q_{vib}}{\partial t} + \frac{q_{vib}}{\tau_{vib}} = \frac{\eta_3}{\tau_{vib}}(\mathbf{J}_e \cdot \mathbf{E}) \quad (2.44)$$

where the relaxation parameter for vibrational excitation (τ_{vib}) is set to 1 μs to represent the delay in the conversion of the energy stored in vibrational excitation to specific internal energy of the bulk flow (u). To calculate η_3 one can use

$$\eta_3 = -0.16041e^{-6107.97|\frac{E}{N}|} - 0.146957e^{-9.4288|\frac{E}{N}|} + 1.02191e^{-0.25157|\frac{E}{N}|} + 3.91435 \times 10^{-2} \quad (2.45)$$

taken from [73].

Figure 2.3 shows the plot of fractional powers (Eq. 2.41, 2.43 and 2.45). As one can see, at lower strengths of the electric field, the heating comes mainly from vibrational excitation, while at higher field strengths, electronic excitation is the dominant factor. Considering that the heating due to vibrational excitation is delayed, one can say that at lower values of E/N the heating is then also delayed, while at higher values the energy from the electric field is almost instantaneously converted to heat.

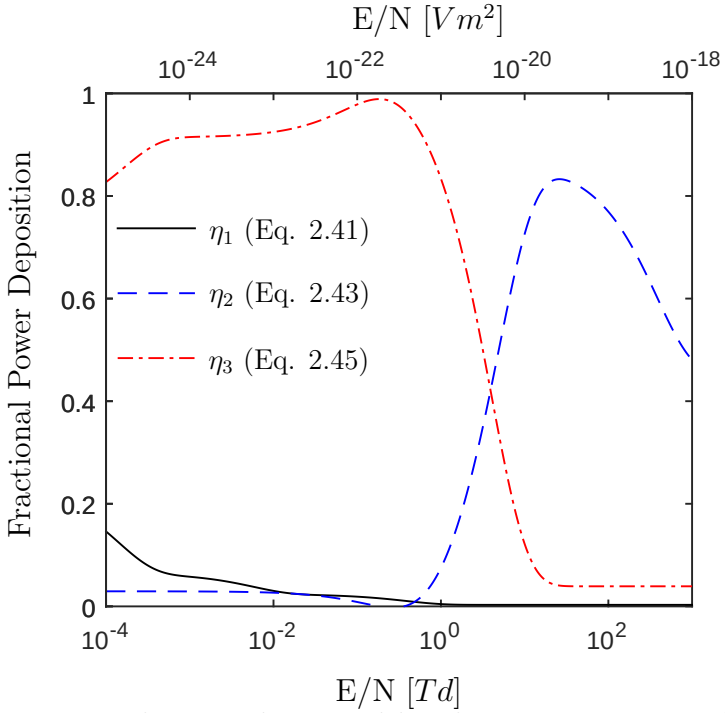

Figure 2.3: Fractional power dissipated by electrons in N_2 as a function of E/N.

2.2 Boundary conditions

2.2.1 Electric field potential (ϕ_E)

Since the electric potential is computed using Eq. 2.17 for the fluid region which may contain a plasma and Eq. 2.18 for the solid dielectric region, the coupling of these two regions at the interface must satisfy the following conditions:

- The electric field component parallel to the surface must be equal across the surface

$$(\mathbf{E}_{\parallel})_{fluid} = (\mathbf{E}_{\parallel})_{diel} \tag{2.46}$$

- The electric displacement field ($\mathbf{D} = \epsilon\mathbf{E}$) normal to the interface must also be continuous unless the surface itself has a non-zero charge in which case the following applies

$$(\mathbf{D}_{\perp})_{fluid} - (\mathbf{D}_{\perp})_{diel} = \sigma_c \mathbf{n}_{fluid} \tag{2.47}$$

Generally the permittivity of a solid dielectric is higher than that of a gas (e.g. nitrogen) and as a result the strength of the electric field is higher in the gas region than in the dielectric as shown in Figure 2.4. This means that higher values of permittivity in the dielectric result in higher values of electric field in the gas and therefore higher ionization rates.

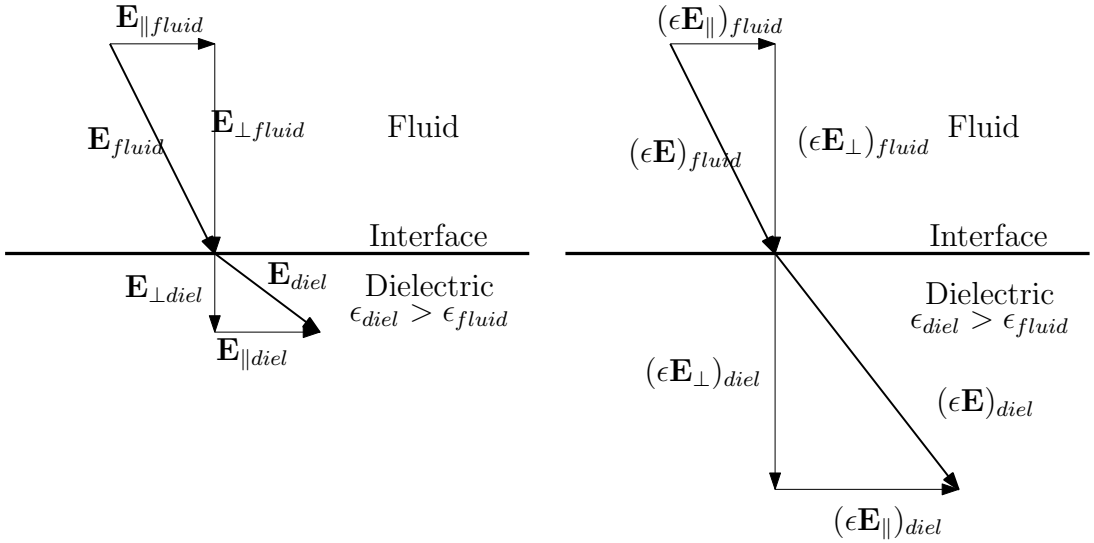

(a) Electric Field, $(\mathbf{E}_{\parallel})_{fluid} = (\mathbf{E}_{\parallel})_{diel}$

(b) Displacement Field for case with $\sigma_c = 0$, $(\epsilon\mathbf{E}_{\perp})_{fluid} = (\epsilon\mathbf{E}_{\perp})_{diel}$

Figure 2.4: The change of electric and displacement fields as they pass from one medium into another.

Since a plasma contains many charged particles which may impact the dielectric surface, it is possible to calculate a net gain/loss of accumulated surface charge (σ_c) through a time integral of the fluxes of the charged particles

$$\sigma_c = \delta_\sigma e_o \int (\mathbf{\Gamma}_p - \mathbf{\Gamma}_e) \cdot \mathbf{n} dt \tag{2.48}$$

where $\mathbf{n}$ is the surface normal on the fluid side (since the charged particles exist only on the fluid side). The term δ_σ is used to ensure that the surface charge is computed only for the fluid - dielectric interface boundary by setting the value to 1 at the interface and 0 everywhere else.

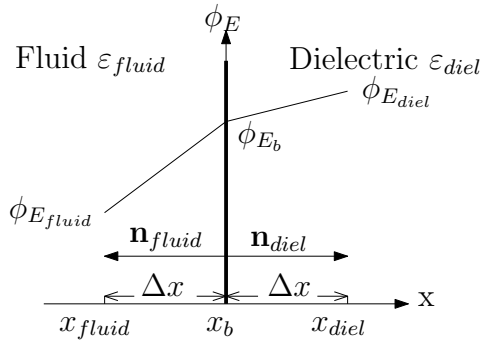

Figure 2.5: Electric potential (ϕ_E) across an interface. The interface is at x_b.

As mentioned previously the electric field is not solved for directly, but rather found from electric potential. In order to solve for the electric potential at the fluid-dielectric interface one can start from Eq. 2.47. The electric displacement field ($\mathbf{D}$) is related to the electric field ($\mathbf{E}$) and therefore the electric potential (ϕ_E) through the following relation:

$$\mathbf{D} = \varepsilon\mathbf{E} = -\varepsilon\nabla\phi_E \tag{2.49}$$

then replacing the $\mathbf{D}$ within Eq. 2.49 for a 1D geometry results in

$$\mathbf{D}_\perp = -\varepsilon\frac{d\phi_E}{dx} \tag{2.50}$$

or referring to Figure 2.5

$$\begin{aligned}(\mathbf{D}_\perp)_{fluid} &= -\varepsilon_{fluid}\frac{d\phi_{E_{fluid}}}{dx_{fluid}} = -\varepsilon_{fluid}\frac{\phi_{E_{fluid}}-\phi_{E_b}}{x_{fluid}-x_b} = -\varepsilon_{fluid}\frac{\phi_{E_{fluid}}-\phi_{E_b}}{-(x_b-x_{fluid})} \\ &= \varepsilon_{fluid}\frac{\phi_{E_{fluid}}-\phi_{E_b}}{\Delta x} = \bar{\varepsilon}_{fluid}(\phi_{E_{fluid}} - \phi_{E_b})\end{aligned} \tag{2.51}$$

where the positive direction is taken from the fluid region into the dielectric region

and $\frac{\varepsilon_{fluid}}{\Delta x}$ is replaced with $\bar{\varepsilon}_{fluid}$ for convenience. Similarly one can write,

$$\begin{aligned}(\mathbf{D}_{\perp})_{diel} &= -\varepsilon_{diel}\frac{d\phi_{E_{diel}}}{dx_{diel}} = -\varepsilon_{diel}\frac{\phi_{E_{diel}}-\phi_{E_b}}{x_{diel}-x_b} \\ &= -\varepsilon_{diel}\frac{\phi_{E_{diel}}-\phi_{E_b}}{\Delta x} = -\bar{\varepsilon}_{diel}(\phi_{E_{diel}}-\phi_{E_b})\end{aligned} \tag{2.52}$$

Inserting Eq. 2.51 and Eq. 2.52 into Eq. 2.47 yields,

$$-\bar{\varepsilon}_{fluid}(\phi_{E_{fluid}}-\phi_{E_b}) - \bar{\varepsilon}_{diel}(\phi_{E_{diel}}-\phi_{E_b}) = \sigma_c \mathbf{n}_{fluid}$$

$$\bar{\varepsilon}_{fluid}\phi_{E_{fluid}} - \bar{\varepsilon}_{fluid}\phi_{E_b} + \bar{\varepsilon}_{diel}\phi_{E_{diel}} - \bar{\varepsilon}_{diel}\phi_{E_b} = \sigma_c\frac{x_{fluid}-x_b}{\Delta x} = -\sigma_c\frac{x_b-x_{fluid}}{\Delta x} = -\sigma_c$$

$$-\phi_{E_b}(\bar{\varepsilon}_{fluid}-\bar{\varepsilon}_{diel}) = -\bar{\varepsilon}_{fluid}\phi_{E_{fluid}} - \bar{\varepsilon}_{diel}\phi_{E_{diel}} - \sigma_c$$

which results in an expression for the potential at the boundary as,

$$\phi_{E_b} = \frac{\bar{\varepsilon}_{fluid}}{\bar{\varepsilon}_{fluid}+\bar{\varepsilon}_{diel}}\phi_{E_{fluid}} + \frac{\bar{\varepsilon}_{diel}}{\bar{\varepsilon}_{fluid}+\bar{\varepsilon}_{diel}}\phi_{E_{diel}} + \frac{\sigma_c}{\bar{\varepsilon}_{fluid}+\bar{\varepsilon}_{diel}} \tag{2.53}$$

This expression represents a weighted average between the two regions with the addition of the surface charge (should it exist).

The remaining boundary conditions for ϕ_E are set to a zero gradient for the domain outer boundaries (i.e. $\frac{\partial \phi_E}{\partial \mathbf{n}} = 0$) and a set value for an electrode surface (which may also be time varying for the exposed electrode in some simulations).

2.2.2 Particle flux (Γ_k)

The conditions for the particle fluxes (Γ_k) at domain boundaries are computed from Eq. 2.22 based on the values calculated at the previous time step. The exposed electrode and the fluid - dielectric interface have to incorporate the fact that the boundary

conditions are different depending on the direction of the electric field. Figure 2.6 shows the direction of the particles moving at a surface under the effect of the electric field. By definition, positively charged particles move along the electric field lines while negatively charged particles move in the opposite direction. In addition, when positive ions strike the surface (Figure 2.6 (a)) there is a chance for an extra electron to be ejected from the surface in response, hence providing a source of free electrons that may further ionize the gas. In the case of the dielectric surface, the surface becomes positively charged by the process (Eq. 2.48).

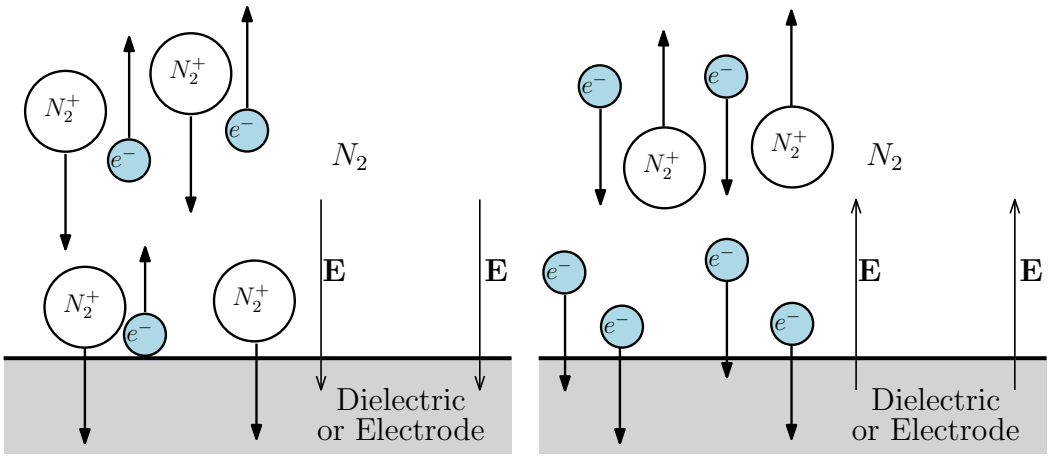

(a) $E_\perp < 0$, σ_c increases

(b) $E_\perp > 0$, σ_c decreases

Figure 2.6: Schematic of the charged particles motion under the effect of electric field.

In the case of an electric field directed away from the surface and into the fluid domain (Figure 2.6 (b)) positive ions leave the vicinity of the surface creating a shortage of ions while embedding electrons into the surface. In this case the dielectric surface becomes negatively charged. Thus the boundary conditions for the particle fluxes are represented by two sets of equations depending on the direction of the

electric field,

$$\mathbf{\Gamma}_e = \begin{cases} -\mu_e \mathbf{E} N_e & if \quad E_\perp > 0 \\ -\gamma \mathbf{\Gamma}_p & if \quad E_\perp < 0 \end{cases} \tag{2.54}$$

$$\mathbf{\Gamma}_p = \begin{cases} 0 & if \quad E_\perp > 0 \\ \mu_p \mathbf{E} N_p & if \quad E_\perp < 0 \end{cases} \tag{2.55}$$

where γ is the secondary emission coefficient (which represents the ejection of electrons through bombardment of a surface by positively charged particles).

2.2.3 Particle number density (N_k)

The continuity equation for the charged particles (Eq. 2.21) requires the calculation of boundary conditions for each charged particle species, in this case electrons (N_e) and positive ions (N_p). These equations must be consistent with the corresponding fluxes and are expressed as

$$N_e = \begin{cases} \nabla N_e = 0 & if \quad E_\perp > 0 \\ \gamma N_p \frac{\mu_p}{\mu_e} & if \quad E_\perp < 0 \end{cases} \tag{2.56}$$

where for $E_\perp < 0$ if the electron flux (Γ_e) is a fraction of the ion flux at the surface ($\Gamma_e = \gamma \Gamma_p$) one obtains the result shown (where $\Gamma_k = \mu_k E N_k$).

$$N_p = \begin{cases} 0 & if \quad E_\perp > 0 \\ \nabla N_p = 0 & if \quad E_\perp < 0 \end{cases} \tag{2.57}$$

Table 2.1 provides an overview of the boundary conditions presented in Figure 2.1

as well as the initial conditions for the two regions.

Location	Variable	Condition
Region 1: Fluid	Relative permittivity (ϵ_r*)	1
	Initial temperature (T_i)	specified
	Initial pressure (p_i)	specified
	Initial number densities (N_{e_i}, N_{p_i})	specified
	Initial electric potential (ϕ_{E_i})	specified (0 V)
Region 2: Dielectric	Relative permittivity (ϵ_r*)	specified
	Initial electric potential (ϕ_{E_i})	specified (0 V)
Exposed electrode	Applied voltage (ϕ_E)	fixed or time-dependent
	Number densities (N_e, N_p)	Eq 2.56 and 2.57
	Charged particles fluxes ($\mathbf{\Gamma}_e$, $\mathbf{\Gamma}_p$)	Eq 2.54 and 2.55
	Should σ_c be computed? (δ_σ*)	No (0)
Interface Fluid	Electric potential (ϕ_E)	coupled (see Eq 2.53)
	Number densities (N_e, N_p)	Eq 2.56 and 2.57
	Charged particles fluxes ($\mathbf{\Gamma}_e$, $\mathbf{\Gamma}_p$)	Eq 2.54 and 2.55
	Should σ_c be computed? (δ_σ*)	Yes (1)
Outer Boundaries	Electric potential (ϕ_E)	zero gradient
	Number densities (N_e, N_p)	zero gradient
	Charged particles fluxes ($\mathbf{\Gamma}_e$, $\mathbf{\Gamma}_p$)	calculated (Eq. 2.22)
	Should σ_c be computed? (δ_σ*)	No (0)
Encapsulated electrode	Applied voltage (ϕ_E)	specified (e.g. 0 V)

Table 2.1: Prescribed properties and boundary conditions. *Note: These variables are kept constant during simulations.

2.3 Numerical discretization

OpenFOAM has a variety of numerical differentiation schemes. The time differentiation was done using a first order implicit Euler scheme. All of the spacial derivatives in OpenFOAM are recast using Gauss theorem,

$$\int_v (\nabla \cdot \mathbf{a}) dv = \oint_A (\mathbf{n} \cdot \mathbf{a}) dA \tag{2.58}$$

Therefore, most of the schemes in OpenFOAM are using Gauss in their names (e.g. Gauss VanLeer).

One of the more common convective schemes available are the upwind (first order space accurate) and central differencing (second order space accurate) schemes. Both have their own advantages and disadvantages. The upwind scheme is stable, but it a first order accurate scheme and produces excessive diffusion (dissipation) error. The central differencing is second-order accurate, but for flows with large gradients (e.g. supersonic flow with shock) it produces dispersion (oscillation) error. To reduce the disadvantages from the two schemes they are sometimes combined with a weighting factor (or a limiter). One such scheme uses Van Leer limiter ($\psi(r)$) (Eq. 2.59) ([77], [78]), and in OpenFOAM this scheme is called "Gauss VanLeer".

$$\psi(r) = \frac{r + |r|}{1 + |r|} \tag{2.59}$$

The r value in Eq. 2.59 is the ratio of gradients around the integration point,

$$r = \frac{upwind\ side\ gradient}{downwind\ side\ gradient} \tag{2.60}$$

In OpenFOAM this limiter allows to switch between upwind scheme at the locations of sharp gradients and central-differencing scheme everywhere else, making the overall

scheme a second-order accurate in space. Therefore, the convective terms in the compressible flow equations (Eq. 2.1, 2.3, 2.4) and in the charged particle continuity equation (Eq. 2.21) are discretized using VanLeer scheme with Van Leer limiter ($\psi(r)$).

The Laplacian terms in Eq. 2.1, 2.4 and in Gauss' Law equation (Eq. 2.17, 2.18) are discretized using a second order Gauss linear scheme.

To improve the iterative stability of the numerical simulations, Eq. 2.21 is modified to the following,

$$\frac{\partial N_k}{\partial t} + \nabla \cdot \mathbf{V}_k^{old} N_k = S_k^{old} \tag{2.61}$$

In Eq. 2.61 the source term (S_k^{old}) is computed completely from variables at the previous time step. The flux term ($\mathbf{\Gamma}_k$) from Eq. 2.21 is replaced with $\mathbf{V}_k^{old} N_k$, where $\mathbf{V}_k^{old} = \frac{\mathbf{\Gamma}_k^{old}}{N_k^{old}}$.

The described model provides all the required information to solve for plasma generation, its propagation under an applied electric field, and its energy deposition into the surrounding gas flow.

Chapter 3

SDBD plasma geometry and code verification

To verify the implementation of the previously described equations the configuration shown in Figure 3.1 is used. The computational domain is 0.8 mm in length, 0.15 mm in height for the fluid region and the dielectric thickness is 0.05 mm. The exposed electrode is 0.1 mm in length along the dielectric surface and has 0 mm thickness while the encapsulated electrode covers the bottom of the dielectric. This geometry is also used by Boeuf [50] whose work also serves as a reference for the current work.

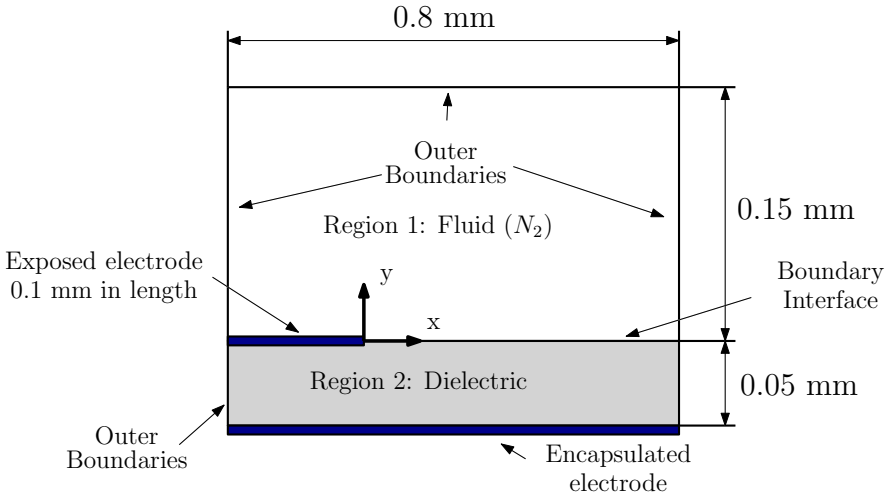

Figure 3.1: Computation domain for OpenFOAM simulations.

3.1 Mesh

Most of the simulations described in this chapter use the same mesh. The only exceptions are the simulations in the mesh sensitivity section (Section 3.4). The mesh is a pseudo - 2D structured mesh (OpenFOAM uses a single element thickness with "empty" boundary conditions in the third dimension) with 117 118 elements: 93570 elements in the fluid region and 23 548 elements in the dielectric region. The mesh has two levels of refinement as shown in Figure 3.2. The coarsest element size is 2.0 μm, and at each refinement region the size of an element is reduced by a factor of two. Therefore, the smallest element size is 0.5 μm. The resulting mesh is shown

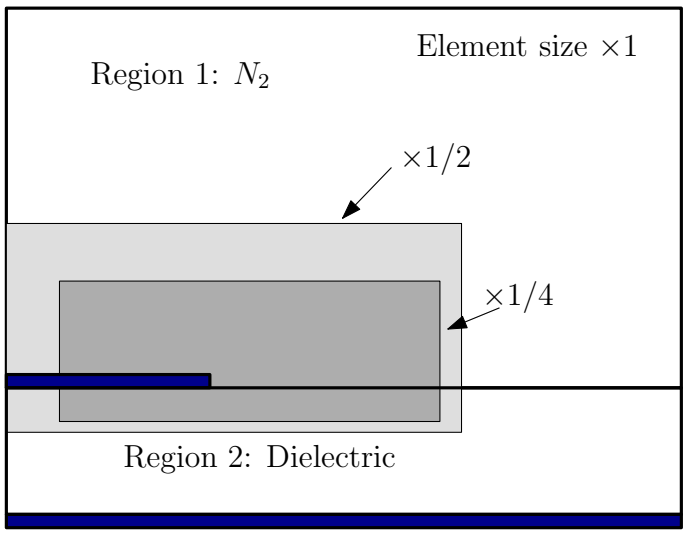

Figure 3.2: Schematic of the mesh refinement.

in Figure 3.3. From Figure 3.3(a) and 3.3(b) one can see the mesh refinement levels as compared to the overall size of the region with the highest charge density for the simulated conditions at 50 ns.

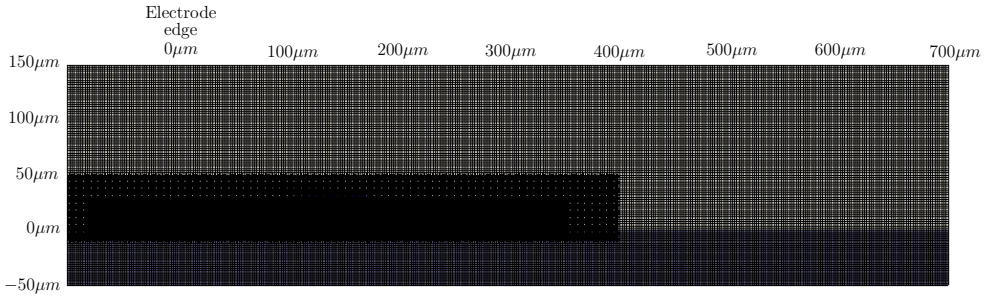

(a) Overall mesh

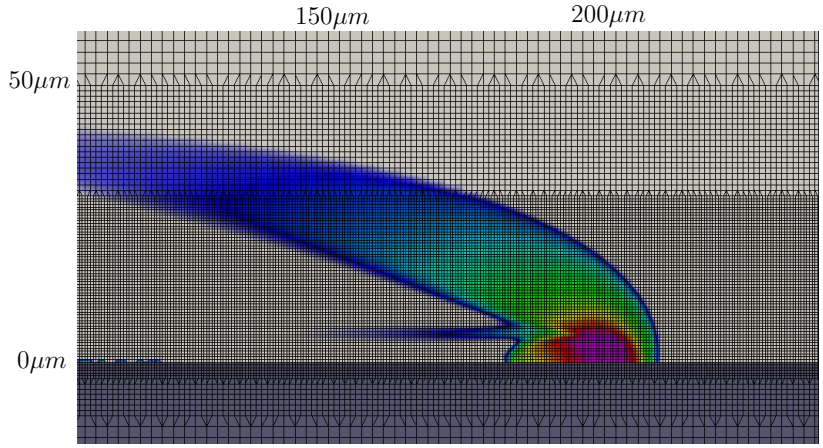

(b) Mesh: zoom in

Figure 3.3: The mesh used in the simulations.

3.2 Simulated Conditions

As per Table 2.1 which shows the generalized boundary conditions used for the plasma simulations, Table 3.1 lists the specific boundary conditions applied for most of the simulations presented in this chapter. Any deviations from the boundary conditions

Location	Variable	Value
Region 1: Nitrogen	ϵ_r*	1
	T_i	300 K
	P_i	100 kPa
	V_i	0 m/s
	N_{e_i}, N_{p_i}	10^{13} m^{-3}
	ϕ_{E_i}	0 V
Region 2: Dielectric	ϵ_r*	10
	ϕ_{E_i}	0 V
Exposed electrode	ϕ_E	1200 V
	N_e, N_p	Eq 2.56 and 2.57, $\gamma = 0.05$
	$\mathbf{\Gamma}_e$, $\mathbf{\Gamma}_p$	Eq 2.54 and 2.55, $\gamma = 0.05$
Fluid - Dielectric Interface (Fluid)	ϕ_E	coupled (see Eq 2.53)
	N_e, N_p	Eq 2.56 and 2.57, $\gamma = 0.05$
	$\mathbf{\Gamma}_e$, $\mathbf{\Gamma}_p$	Eq 2.54 and 2.55, $\gamma = 0.05$
Encapsulated electrode	ϕ_E	0 V

Table 3.1: Simulated condition. *Note: These variables are kept constant during simulations.

shown in Table 3.1 are noted in the corresponding sections. The values shown in Table 3.1 correspond to those used by both Boeuf [50] and Abdollahzadeh [73]. In this chapter all of the simulations are performed under the assumption that the bulk flow doesn't change its properties and remains at rest (velocity is 0 m/s). The fluid in the computational domain is diatomic nitrogen gas (N_2) with a temperature of 300 K, and a pressure of 100 kPa. These two values do not change throughout the

simulations. The initial values of charged particle densities are set to 10^{13} m^{-3}. The relative permittivity of dielectric is set to 10.

3.3 DBD plasma geomtery

One can separate the fluid domain into a neutral gas and a plasma region. The difference between the two regions is the presence of a high number of charged particles in the plasma region as shown in Figures 3.4 and 3.5. The figures indicate that the plasma region propagates 50 μm away from the dielectric surface for the given conditions, while the rest of the domain has a low concentration of charged particles, and therefore doesn't affect the electric field and can be treated as neutral gas.

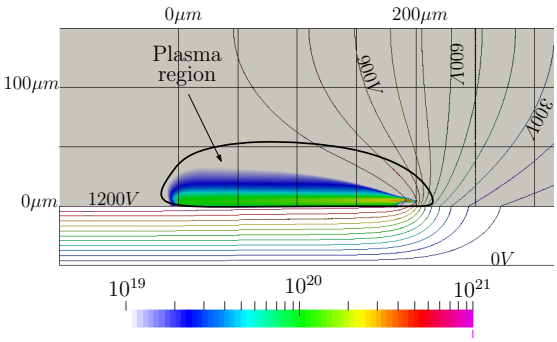

Figure 3.4: Concentration of electrons $[m^{-3}]$ at 50 ns.

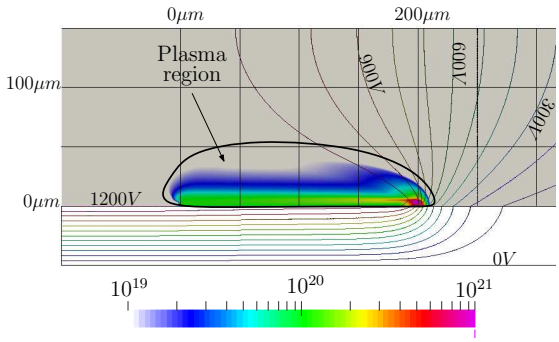

Figure 3.5: Concentration of positive ions (N_p) $[m^{-3}]$ at 50 ns.

The plasma region can be further subdivided into sheath and neutral plasma regions as shown in Figure 3.6. The sheath region is the border region of plasma where the electric field is strong, resulting in an unequal distribution of charged particles, which in turn results in a relatively high charge density (here it's defined as higher than 1 C/m^3). It is this region which also contains the highest ionization rates. The sheath portion is used to define the leading edge of the plasma and is used to judge the speed of propagation of plasma ionization front. At 50 ns after the

application of the 1 200 V to the exposed electrode, the thickness of the sheath can be seen to be about 25 μm and has reached as far 210 μm away from the edge of the exposed electrode.

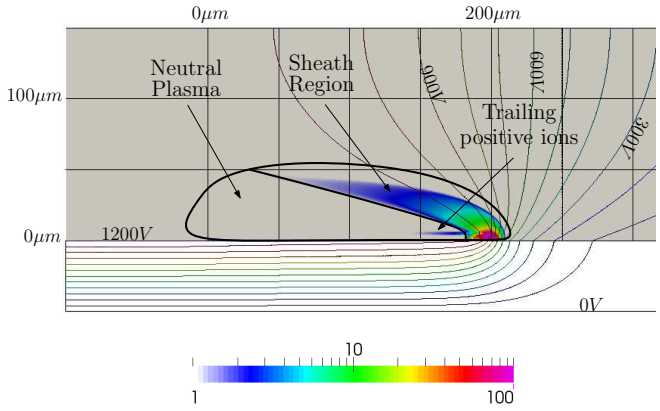

Figure 3.6: Charge density (ρ_c) $[C/m^3]$ at 50 ns. The contour lines are the electric field potential: 0 V for the bottom surface (grounded electrode) and 1 200 V for the exposed electrode.

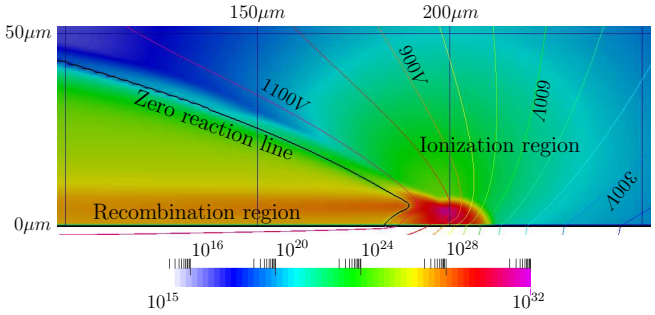

Figure 3.7: Reaction rate $[m^{-3}s^{-1}]$ at 50 ns. Maximum recombination rate (within neutral plasma region) is in the order of 10^{28} $m^{-3}s^{-1}$. Maximum ionization rate (within sheath region) is in the order of 10^{32} $m^{-3}s^{-1}$.

As mentioned before, the sheath is also the region with the highest ionization rates as shown in Figure 3.7. This figure is separated into ionization and recombination regions by a "zero reaction line". As one can observe from the figure the ionization rate is four orders of magnitude higher than the electron-ion recombination rate. However, the ionization is mainly concentrated in the sheath region at the dielectric

surface, while the recombination reactions are more diffuse and occur throughout the neutral plasma region. This also means that the trailing positive ions (indicated in Figure 3.6) can be attributed to the positive ions that remain behind the ionization front due to the low ion mobility and slower recombination rates. Figure 3.8 shows the

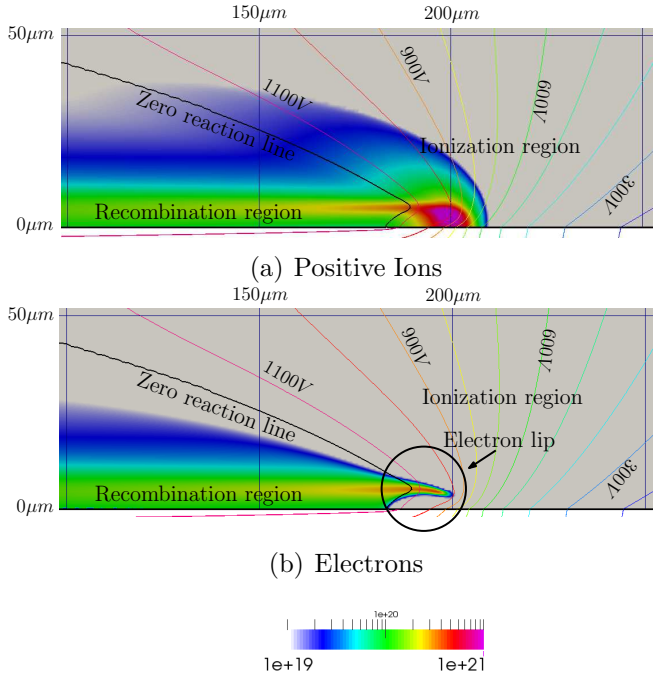

Figure 3.8: Close up view of the positive ions (N_p) and electron (N_e) concentration $[m^{-3}]$ at 50 ns in the vicinity of the plasma front.

close up view of the charged particles concentration in the vicinity of the ionization front and the trailing positive ions are clearly visible in Figure 3.8 (a). Figure 3.8 (b) shows the electron lip where the electrons in the ionization region are forced into a concentrated formation above the dielectric surface. Below of this formation the concentration of electrons is considerable lower (below 10^{19} m^{-3}) yet rapid ionization still occurs. The lack of electrons in this area which tends to reduce the ionization is compensated by a higher electric field strength (which can be observed in Figure 3.9). High electric fields increase the ionisation and thus the high electric field strength of 10^7 V/m and above surrounding the electron formation dominates the ionization rate.

Figure 3.9 also clearly shows the low electric field strength within the neutral plasma region which is shielded by the sheath region and the surface charge. However,

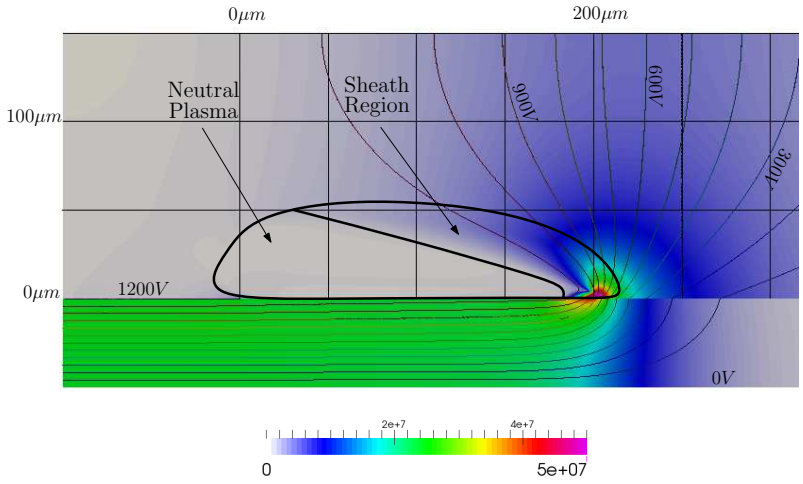

Figure 3.9: Electric field strength ($|\mathbf{E}|$) $[V/m]$ at 50 ns.

the neutral plasma region still contains a high number of charged particles as seen from Figure 3.4 and 3.5. While the maximum value of the concentration of charged particles is on the order of 10^{21} m^{-3} in the sheath region, the charged particle concentration within the neutral plasma is still on the order of 10^{20} m^{-3} (compared to 10^{13} m^{-3} initially in the gas).

Figure 3.9 also shows the discontinuity in the electric field across the dielectric surface. This is attributed to the surface charge at the dielectric surface and the difference in the electric permittivity of the dielectric and gas. To better illustrate this, Figure 3.10 shows the graphs of the vertical components of the electric and electric displacement fields along the vertical lines at three different locations: behind the plasma front (100 μm away from the trailing edge of the exposed electrode along the surface of dielectric), at the plasma front (200 μm from exposed electrode) and ahead of the plasma region (300 μm from exposed electrode). In this figure the dielectric is located between -50 and 0 μm. The electric and displacement fields are nearly constant within the dielectric at 100 μm. At this location the dielectric region

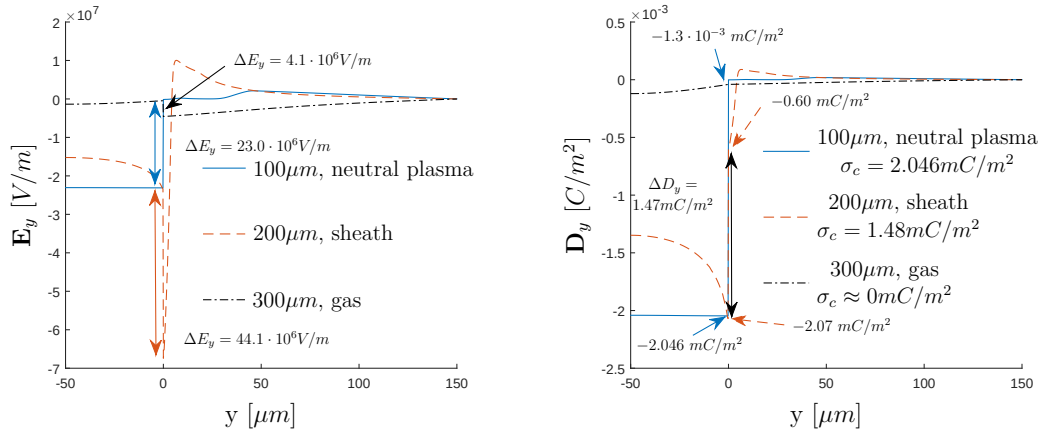

(a) Vertical component of the electric field

(b) Vertical component of the displacement field

Figure 3.10: Vertical component of electric ($\mathbf{E}_y$) and displacement fields ($\mathbf{D}_y$) at 50 ns. Note: surface charge at 100 μm is 2.046 mC/m^2, at 200 μm it is 1.48 mC/m^2 (which is approximately equal to the difference in the displacement field across the interface: -2.07 mC/m^2+0.6 mC/m^2) and at 300 μm it is 2.4·10^{-8} mC/m^2 (≈ 0).

is isolated by the plasma and surface charge above the dielectric. At the surface of the dielectric the two fields are discontinuous, which is also visible in Figure 3.9. According to Eq. 2.47 this behaviour is expected. When looking at the displacement field difference across the gas-dielectric interface ($y = 0$ μm) at $x = 100$ μm it should be equal to the surface charge at that location which is equal to 2.046 mC/m^2 . This is actually the case as shown in Figure 3.10 (b) at $x = 100$ μm. As was mentioned before the electric field within the neutral plasma is close to zero, also shown in Figure 3.10 for 100 μm line at $y \geq 0$.

For the line that passes through the sheath region (200 μm) a discontinuity is also present, but the values at the surface is different leading to a much larger variation across the gas-dielectric interface (a ΔE_y of 44.1 ·10^6 V/m for the electric field and ΔD_y of -0.6 mC/m^2 for the displacement field). However, this difference in the displacement field across the surface is still equal to the surface charge at this location as shown in Figure 3.10 at $x = 200$ μm (1.48 mC/m^2). Since this data line crosses

through the plasma front and the sheath region the electric field changes sharply near the surface within the gas domain (from $-6.7 \cdot 10^7$ V/m to $1 \cdot 10^7$ V/m) and also changes significantly within the dielectric domain (from $-1.5 \cdot 10^7$ V/m to $-2.4 \cdot 10^7$ V/m). The location ahead of the plasma front (300 μm) has nearly zero surface charge ($2.4 \cdot 10^{-8}$ mC/m^2) and therefore doesn't have any visible discontinuity in the displacement field. The discontinuity in the electric field ($\Delta E_y = 4.1 \cdot 10^6$ V/m) is still present due to the difference in the permittivity between the gas and dielectric domains.

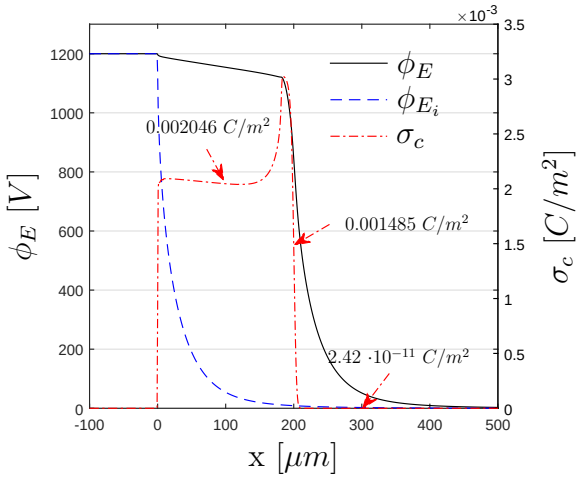

Figure 3.11: Electric potential (ϕ_E) and surface charge density (σ_c) distribution along the dielectric surface at 50 ns. The graph also shows the initial voltage (ϕ_{E_i}).

In addition to the surface charge density (σ_c), Figure 3.11 also shows the electric potential (ϕ_E) at 50 ns and the electric potential right after the start of the simulation (ϕ_{E_i}). As one can see, the surface charge acts as an extension of the exposed electrode. The spike in the surface charge corresponds to the location of the sheath region which has a significant excess of positive ions. The slope of the electric potential line (ϕ_E) between the edge of the exposed electrode and the plasma front indicates a finite conductivity of plasma. This means that as the plasma front moves further away from the electrode the voltage continues to drop leading to an eventual reduction in

the currents and the exhaustion of the ionization process.

Figures 3.12 - 3.15 show the evolution of the four parameters (ρ_c, E, N_e and N_p) in time. In Figure 3.12, within the first 20 ns one can see that a sheath region is being formed. This is indicated by the formation of the relatively consistent shape of

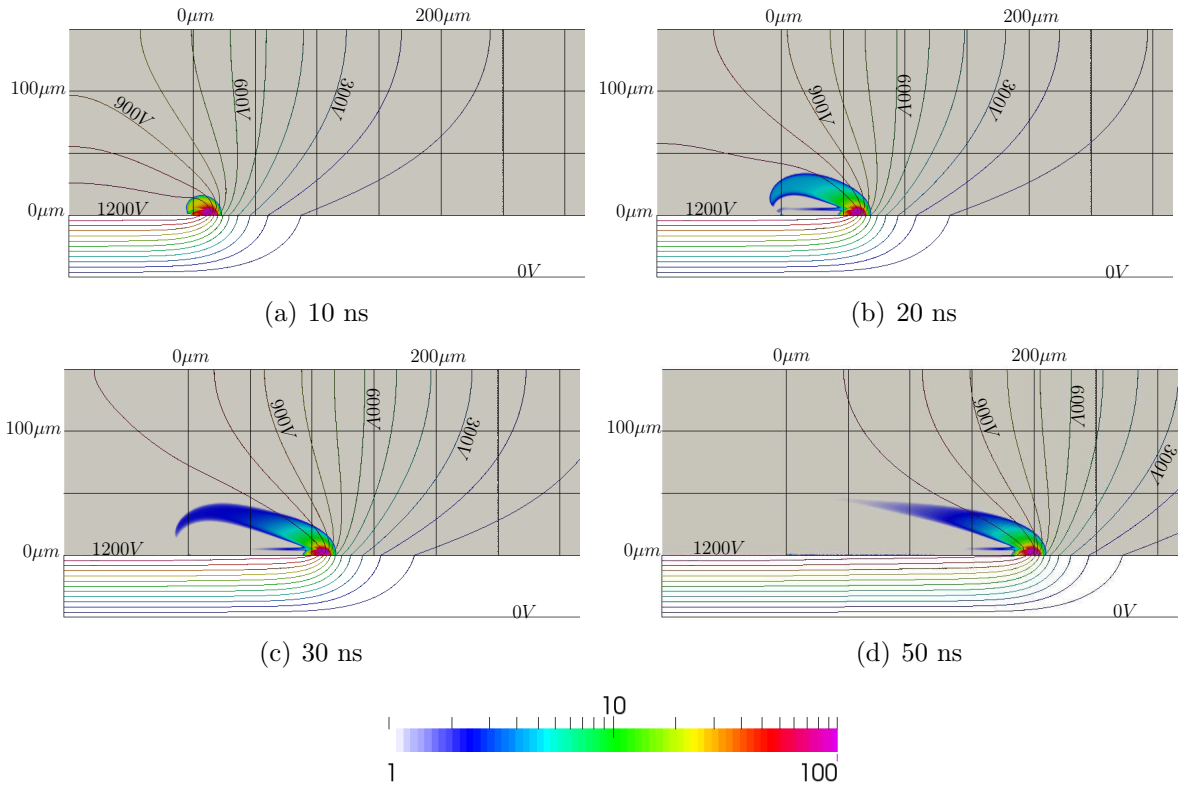

Figure 3.12: Evolution of volumetric charge density (ρ_C) distribution $[C/m^3]$. The contour lines are the electric field potential: 0 V for the bottom surface (grounded electrode) and 1 200 V for the exposed electrode. The origin of horizontal axis is located at the edge of the exposed electrode ($0\mu m$).

the charge density distribution at its rightmost extent as well as its top section (tail) above the neutral plasma region. This "tail" eventually detaches from the exposed electrode as the plasma front moves to the right (see Figure 3.12(c) and 3.12(d)). The trailing positive ions within the otherwise neutral plasma become noticeable at 20 ns in Figure 3.13 and persist until the end of simulation, though the concentration diminishes as plasma propagates further away from the electrode. This is indicated

by reduction of the length of the positive charge segment as well as the reduction in positive ions concentration Figure 3.13.

During the plasma formation process the ionization front is moving along the surface of the dielectric and away from the surface. Once formed, the sheath propagates mainly in the direction along the surface from higher potential to lower potential, charging the surface along the way and leaving a trail of charged particles behind (Figures 3.13 and 3.14). This also results in an almost uniform electric field (Figure 3.15) within the dielectric in the region behind the ionization front below the neutral plasma.

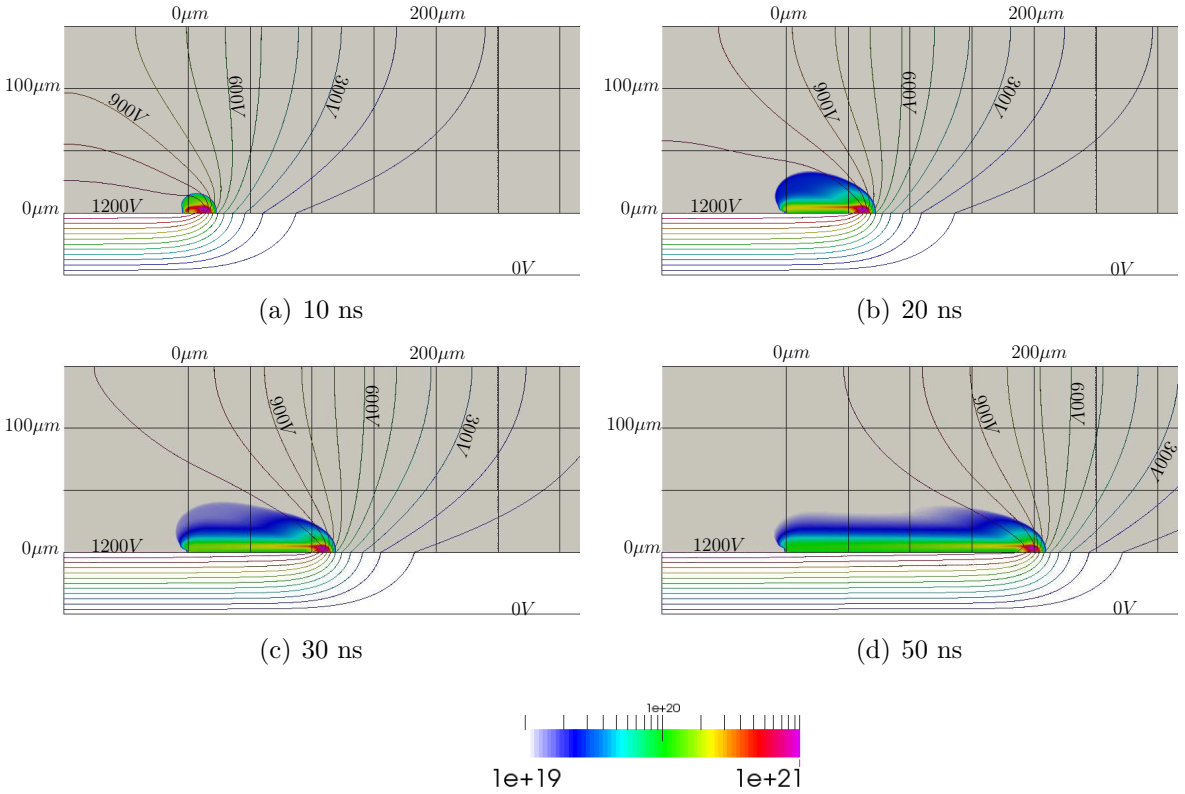

Figure 3.13: Evolution of positive ion density (N_p) distribution [m^{-3}]. The contour lines are the electric field potential: 0 V for the bottom surface (grounded electrode) and 1 200 V for the exposed electrode. The origin of horizontal axis is located at the edge of the exposed electrode ($0\mu m$).

The formation of the neutral plasma zone can be observed in Figure 3.15. At 10

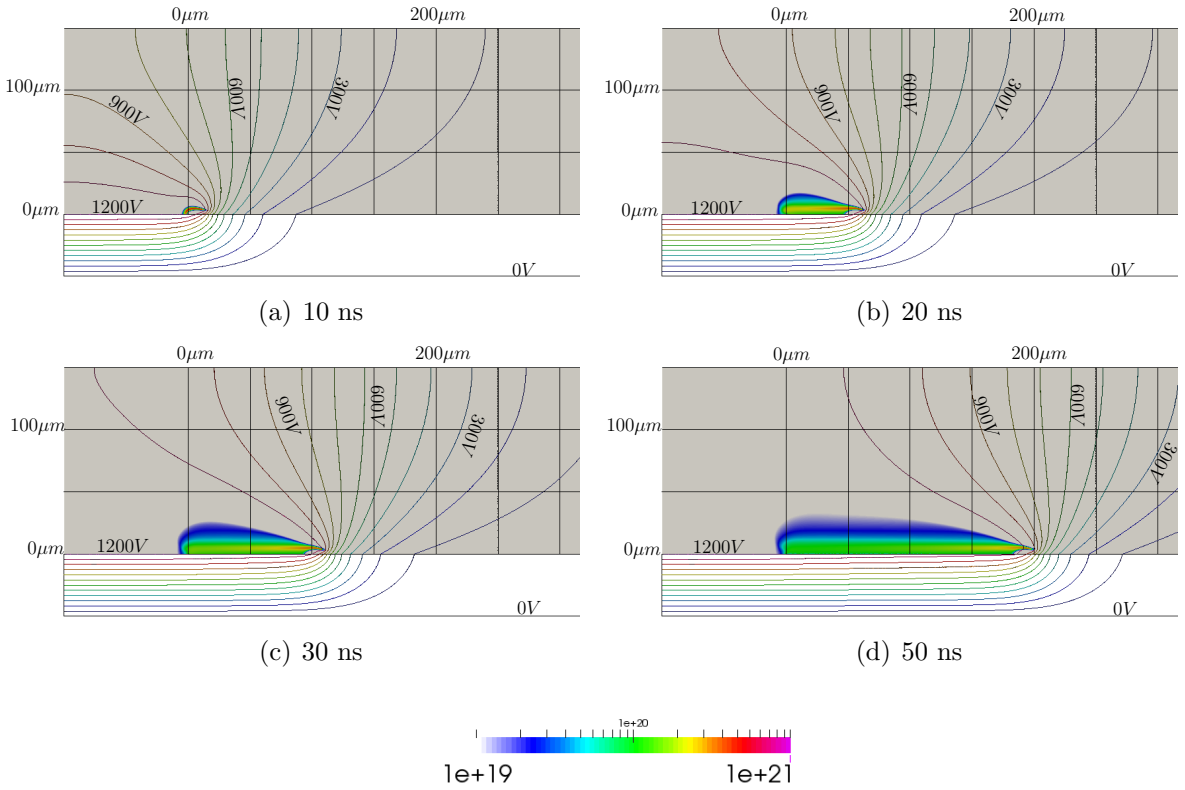

Figure 3.14: Evolution of electron density (N_e) distribution [m^{-3}]. The contour lines are the electric field potential: 0 V for the bottom surface (grounded electrode) and 1 200 V for the exposed electrode. The origin of horizontal axis is located at the edge of the exposed electrode (0 μm).

ns at the edge of the exposed electrode (0 μm) a small region of E =0 can be seen, but before this time the concentration of charged particles is too low to form a sheath region and thus shield the neutral plasma from the external electric field. At 20 ns the neutral plasma region becomes larger and continues to increase as time progresses. The electric field strength inside the dielectric directly below the electrode is equal to $2.4 \cdot 10^7$ V/m as set by the boundary conditions (1 200 V/50 μm)calculated. This value remains the same for the length of the simulation since as time progresses the edge effect moves further away from the electrode. The magnitude of the electric field within the dielectric below the neutral plasma remains very close to this value (e.g. at 50 ns and 150 μm away from the exposed electrode it is $2.32 \cdot 10^7$ V/m).

The maximum magnitude of the electric field in the sheath region reaches $8.4 \cdot 10^7$ V/m at 10 ns and drops to $7.6 \cdot 10^7$ V/m at 50 ns, while the magnitude of the electric field within neutral plasma varies from $3 \cdot 10^5$ V/m to $5 \cdot 10^5$ V/m depending on the location within the neutral plasma region. The drop in the magnitude of the electric field inside the sheath region is due to the increase in the distance from the exposed electrode and a reduction in the maximum electric potential (ϕ_E) within the sheath region.

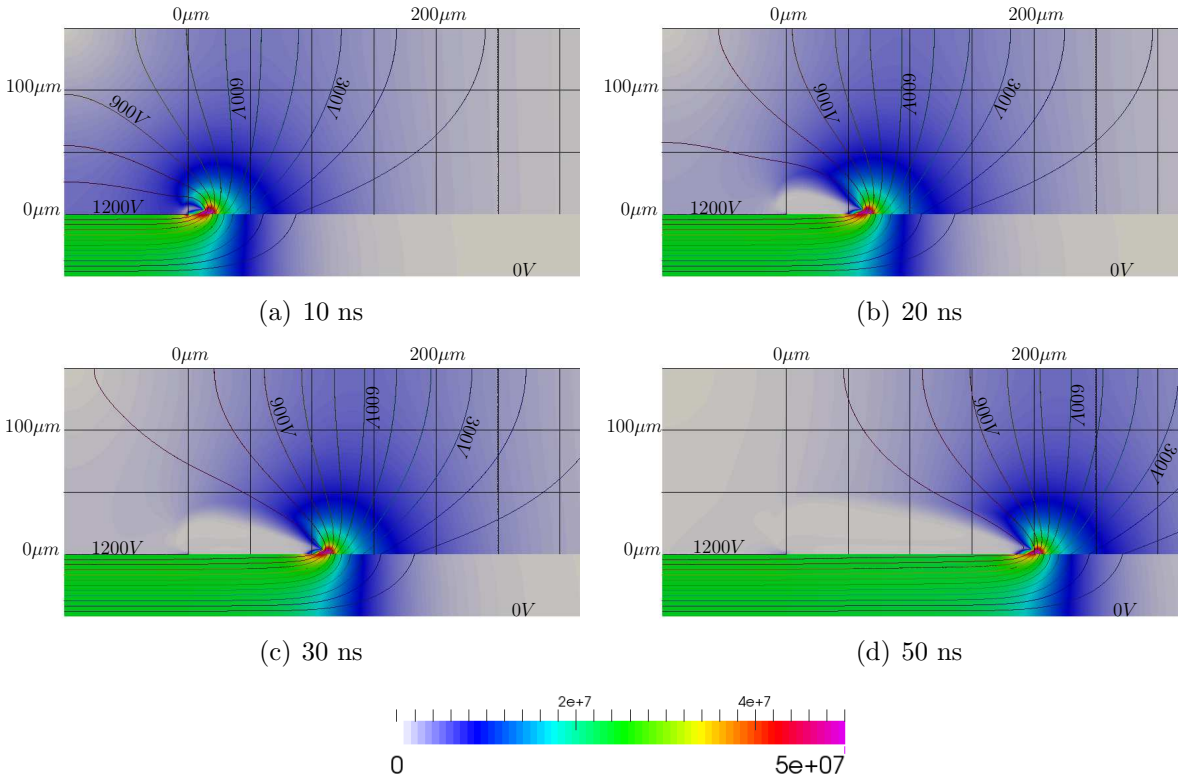

(a) 10 ns

(b) 20 ns

(c) 30 ns

(d) 50 ns

Figure 3.15: Evolution of electric field ($|\mathbf{E}|$)distribution [V/m]. The contour lines are the electric field potential: 0 V for the bottom surface (grounded electrode) and 1 200 V for the exposed electrode. The origin of horizontal axis is located at the edge of the exposed electrode ($0\mu m$).

Figure 3.16 shows the evolution of the surface charge and the electric potential along the dielectric surface. The maximum value of the surface charge is on the order of $3 \cdot 10^{-3}$ C/m^2 in the sheath region and around $2 \cdot 10^{-3}$ C/m^2 in the rest of the

plasma region. After the initial formation of the sheath region this value decreases as the ionization front moves further away from the exposed electrode. As the sheath moves away from the exposed electrode it leaves behind an approximately linear variation in ϕ_E as shown in Figure 3.16 (b),(c),and (d) with a value of of 372 V/mm within the plasma region. In the region ahead of the ionization front in the absence of an accumulated electric charge, potential rapidly approaches zero hence creating the strong electric field helping sustain the ionization process.

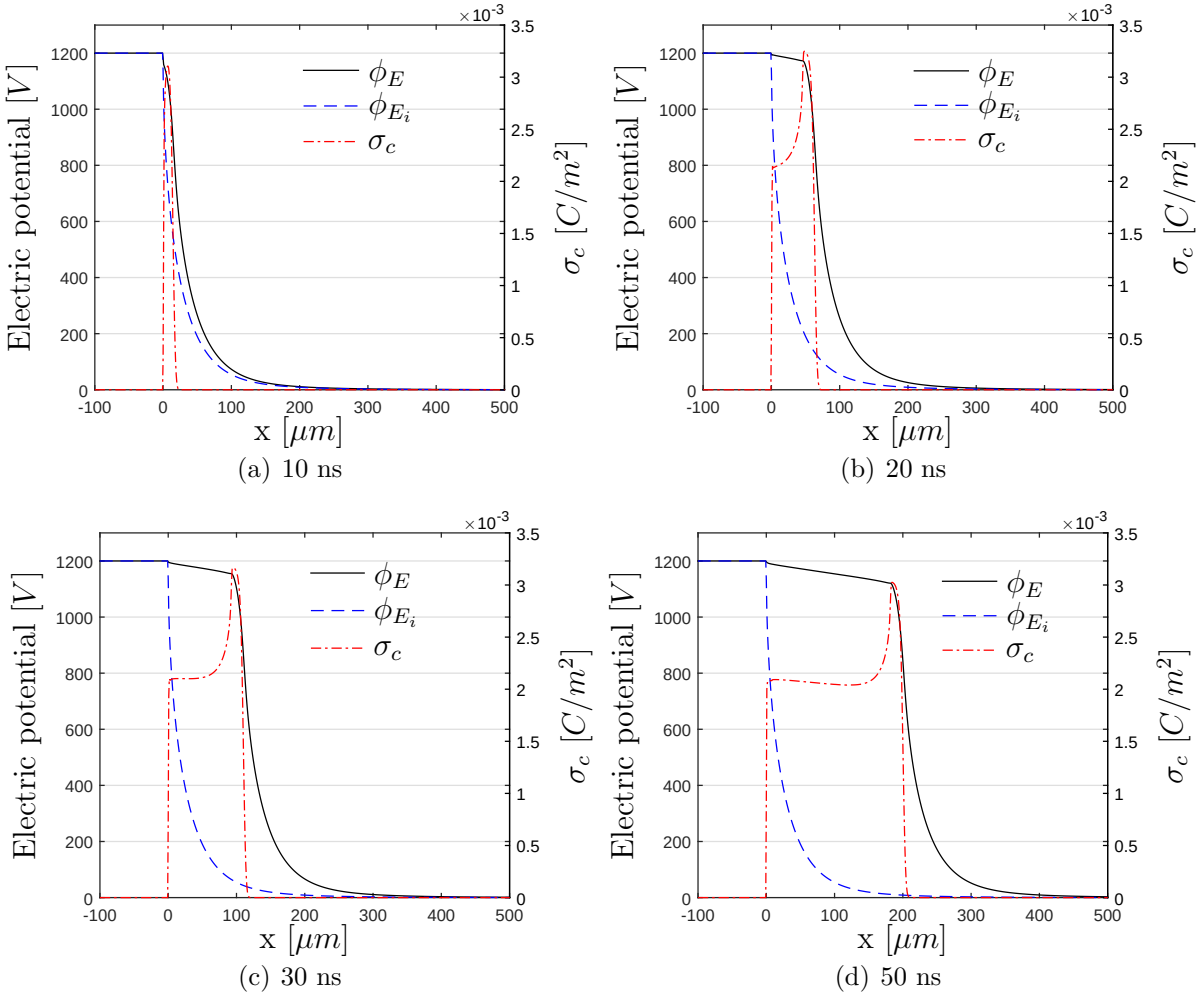

Figure 3.16: Evolution of electric potential (ϕ_E) and surface charge density (σ_c) along the dielectric surface. The graph also shows the initial voltage. (The edge of the exposed electrode is at 0 μm).

Figure 3.17 shows the approximate position of the plasma front (as measured by the sheath position) and the speed of this front's propagation. The position of the plasma front is estimated based on the maximum value in the surface charge (σ_c), horizontal (E_x) and vertical (E_y) electric field components along the surface of the dielectric. The maximum surface charge (the peaks in σ_c in Figure 3.16) corresponds to the trailing edge of the sheath region while the maximum position of the electric field components are located near the front of the sheath region. By taking the derivative of the position location with time one can obtain the speed of plasma propagation along the dielectric surface. In Figure 3.17(b) the speed is computed by taking the derivative of the position of plasma front based on E_x as location based on σ_c proved too noisy. Outside an initial spike at 10 ns the plasma front speed drops from 5 $\mu m/ns$ to 4.1 $\mu m/ns$ at 70 ns. The reduction in speed appears reasonable since the electric potential at the plasma front is reduced and therefore the ionization process is reduced (which leads to slower propagation).

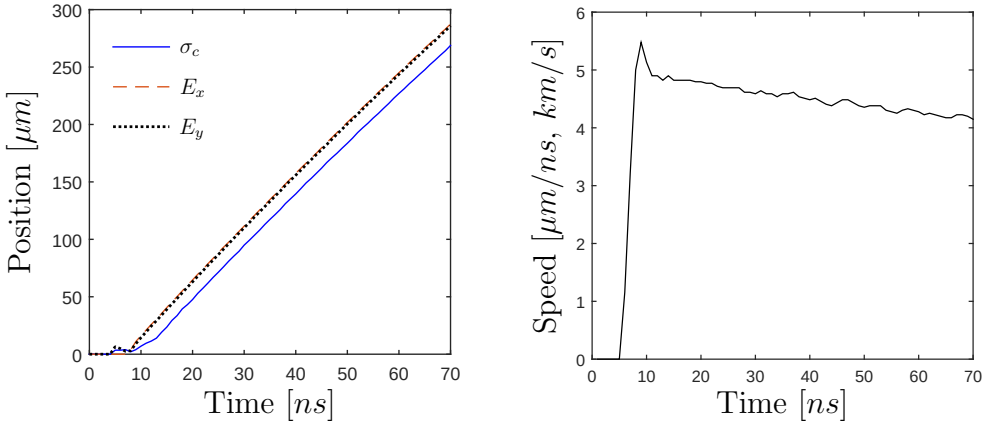

(a) Approximate position of plasma front (b) Speed of plasma front propagation

Figure 3.17: Estimates of plasma front position and its speed.

3.4 Grid convergence study

Figures 3.2 and 3.3 (Section 3.1) show the mesh refinement schematic and the mesh that is used for most of the simulations. As mentioned, there are two levels of refinement with the smallest element size being 0.5 μm. To test the effects of the mesh on the plasma results, two additional meshes are evaluated. These additional meshes add another refinement region such that the most refined mesh has 4 levels of refinement (Mesh 1 in Table 3.2). A medium mesh is also used which has 3 levels of refinement (Mesh 2 in Table 3.2) while the coarsest mesh which has 2 levels is depicted in Figure 3.3 (Mesh 3, Table 3.2). The physical limits of these additional refinement regions is

Mesh	Refinement levels	Total number of elements	Minimum element edge length (μm)
1	0, 1, 2, 3, 4	760 370	0.125
2	0, 1, 2, 3	251 870	0.25
3	0, 1, 2	105 470	0.5

Table 3.2: Description of meshes.

indicated in Table 3.3. The result is that the coarsest mesh (Mesh 3) has two levels of refinement, a total of 105 470 elements and a minimum edge length of 0.5 μm. The medium mesh (Mesh 2) has 251 870 elements with a minimum edge length of 0.25 μm and the finest mesh (Mesh 1) has 760 370 elements with a minimum edge length of 0.125 μm.

Figure 3.18 shows the overall effect of the element size on the evolution of the current through the exposed electrode. The figure has three regions (A, B, and C) showing the locations of maximum discrepancy. The errors between the three meshes are amplified in these regions due to the presence of a high rate of change of the current. Region A is at the onset of the current spike between 5 and 7 ns. The difference between Mesh 3 and the other two meshes is as high as 50 %, whereas the difference between Mesh 2 and Mesh 1 is 12 %. Region B is the peak of the current

Refinement Level	x - limits (μm)	y - limits (μm)	Element size (μm)
0	Domain	Domain	2
1	-100 to 400	-10 to 50	1
2	-80 to 350	-3 to 30	0.5
3	-70 to 330	-2.5 to 28	0.25
4	-65 to 310	-2.2 to 26	0.125

Table 3.3: Mesh refinement levels.

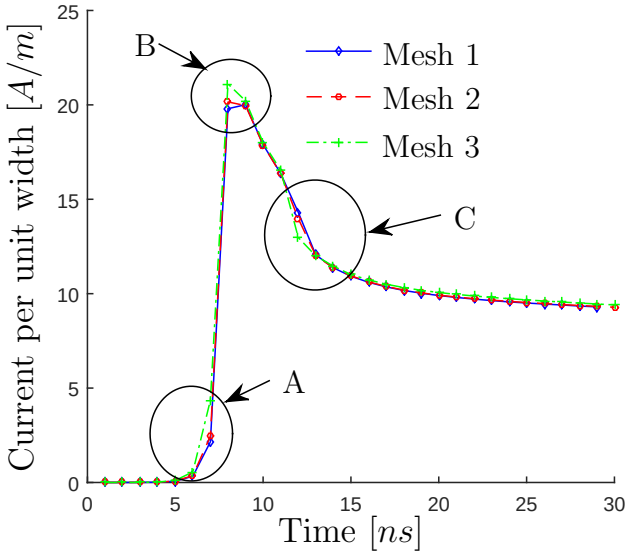

Figure 3.18: Current density per unit width for the exposed electrode for different meshes.

which occurs during 7 to 10 ns. The different element size causes a difference of 7 % between Mesh 3 and Mesh 1, and 2 % between Mesh 2 and Mesh 1. Region C occurs between the current peak and plateau. The difference for the current in this region is within 12 % when comparing Mesh 3 to Mesh 1 and 5 % when comparing Mesh 2 to Mesh 1. All of the above differences can be attributed to a delay of 0.1 ns for the ionization when comparing Mesh 3 to Mesh 1 and 2.

For further uncertainty estimation a point is selected at 20 ns, 12 μm to the right as measured from the exposed electrode edge, 3.6 μm above the dielectric surface.

At 20 ns this location corresponds to the plasma region and is shown in Figure 3.19 together with the positive ion concentration. Figure 3.20 shows a comparison between

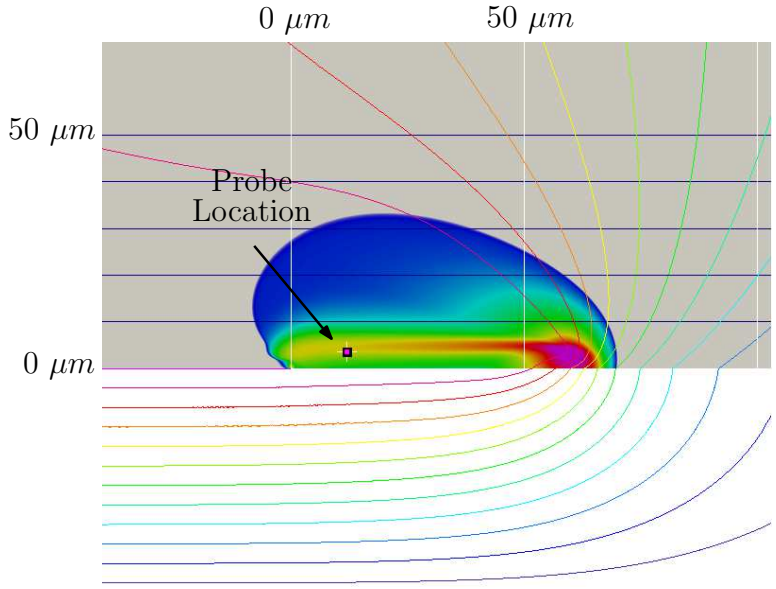

Figure 3.19: Location of of the probe with respect to the positive ion concentration(N_p) at 20 ns. It is located 12 μm away from the edge of the exposed electrode and 3.6 μm above dielectric surface.

the three meshes normalized to Mesh 1 for four variables taken at that point: electric potential (ϕ_E), electric field strength E, and the number densities of electrons (N_e) and positive ions (N_p). In addition, the surface charge accumulated on the dielectric surface by 20 ns is also included. The difference between Mesh 2 (0.25 μm) and Mesh 1 (0.125 μm) is within 1 % for all tested variables. When comparing Mesh 3 to Mesh 1 the difference varies from as high as 5 % for the electric field and accumulated charge to as low as 0.1 % for the electric potential.

Table 3.4 presents the results of a sensitivity study using procedures outlined by Freitas [79]. According to this analysis the errors for the tested values between Mesh 1 (finest) and an estimated theoretical perfect (no grid error) value (based on mesh extrapolation mentioned by Freitas [79]) is 0.4 % or less for the finest mesh based on the GCI for any variables shown in Table 3.4. For Mesh 2 (medium) the GCI is no

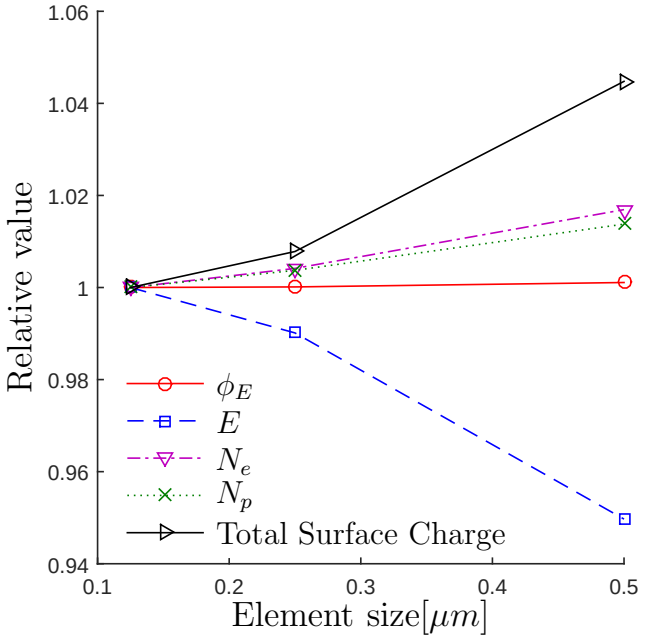

Figure 3.20: Normalized variable comparison between three meshes at 20 ns. ϕ_E, E, N_e and N_p are taken at a location shown in Figure 3.19, while .

greater than 1.65 % for all the variables considered.

	ϕ_E $[V]$	E $[10^6 V/m]$	N_e $[10^{20} m^{-3}]$	N_p $[10^{15} m^{-3}]$	Charge $[10^{-9} C/m]$
size ratio (Mesh 2 vs 1)	2				
size ratio (Mesh 3 vs 2)	2				
value (Mesh 1)	1187.88	0.4744	2.004	2.069	151.7
value (Mesh 2)	1188.03	0.4698	2.012	2.077	152.9
value (Mesh 3)	1189.17	0.4506	2.038	2.097	158.5
estimated value	1187.86	0.4760	2.000	2.064	151.3
observed order p	2.93	2.04	1.62	1.43	2.24
GCI_{Mesh_1} [%]	0.0024	0.40	0.25	0.27	0.26
GCI_{Mesh_2} [%]	0.018	1.65	0.77	0.74	1.23

Table 3.4: Grid Convergence Results.

Although the coarsest mesh (Mesh 3) differs by a maximum of approximately

5 % from estimated values as shown in the table, based on the small increases in accuracy when observing the GCI of Mesh 1 or 2, Mesh 3 is used for all the remaining simulations due to its faster computational times.

Having quantified the errors associated with the grid, the accuracy of the simulations can be verified by comparison to experiment (as is done in Chapter 6). However, the relative scarcity of detailed experimental data along with the abundance of numerical work allows for another means of verification.

3.5 Verification

As was mentioned before, Figure 3.13 shows the evolution of positive ion particles. These results in terms of plasma propagation and movement are in reasonable agreement with similar simulations performed by Abdollahzadeh et al. [73] and Boeuf et al. [50] under quiescent conditions (as described in Table 3.1). The maximum ion concentration levels (on the order of 10^{21} m^{-3}) and the behaviour of the positive ions shown in Figure 3.13 in terms of the shape and development of the plasma match the simulations of Abdollahzadeh et al. [73]. However, the ionization front is travelling at approximately 4-5 $\mu m/ns$ which is slightly higher than the value mentioned by Boeuf et al. [50] of 3 $\mu m/ns$ (where it is not specified how the plasma speed is calculated).

Figure 3.21 shows a comparison of the currents' evolution between this work and the work presented by Abdollahzadeh [73] and Boeuf [50]. The current is obtained by integrating the difference between the electron flux and the flux of positive ions along the length of the charged electrode multiplied by the elementary charge (in this case the positive ion flux is actually zero due to the boundary conditions). While the peak for the current is noticeably higher initially, it reaches values comparable to the work of others within the first 20 ns. This higher initial current could be caused by higher ionization rates which would also result in the faster propagation of the

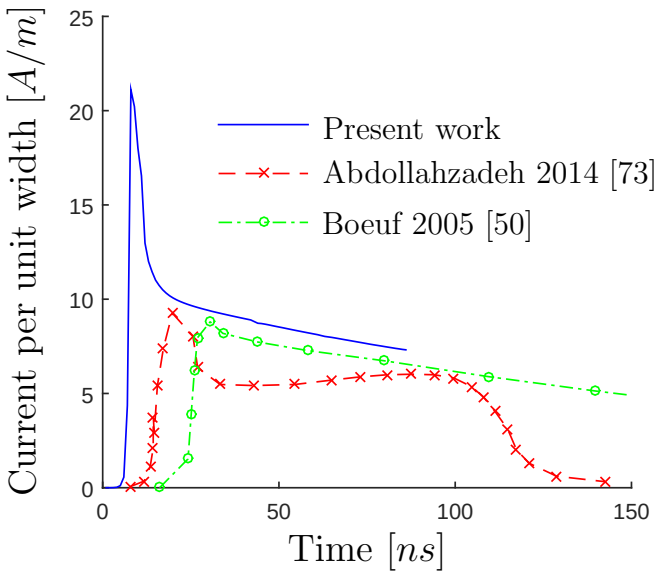

Figure 3.21: Current density per unit width for the exposed electrode (the unit of width is in the direction normal to the plane of the computational domain).

ionization front observed between the three investigations. The current simulations indicate that the maximum current per unit width is reached within the first 10 ns, while in Abdollahzadeh it happens within 20 ns and in the case of Boeuf results after 30 ns. The following section investigates the potential reasons for this discrepancy.

3.6 Parametric study

3.6.1 Effects of applied voltage wave form

The ionization process is directly related to the applied voltage at the exposed electrode. Figure 3.22 compares three different voltage profiles that are used to reach 1 200 V and include a constant 1 200 V, an arctangent curve and an incomplete sine wave (Figure 3.22(a)). For each approach, the designed voltage is reached within 25 ns or less. The main difference between the resultant currents is the delay in the initial current spike which is caused by the delay in achieving the maximum voltage.

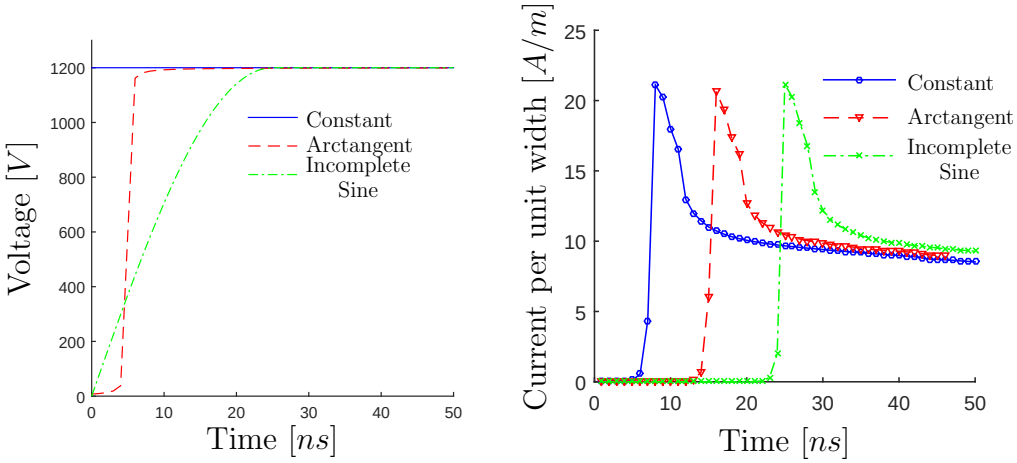

(a) Applied voltage profile at the exposed electrode

(b) Current density per unit width

Figure 3.22: Comparison of different applied voltage profiles.

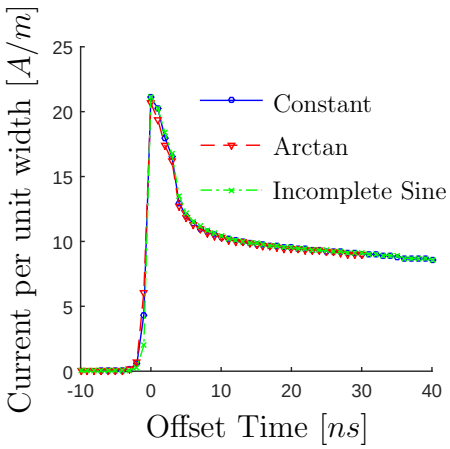

Figure 3.23: Different Voltage profiles comparison: the current density per unit width for the exposed electrode with offset time of 0 set to the location of the peak current.

The overall shape and magnitude of the spike remains approximately constant. This is more clearly observed in Figure 3.23 in which all three lines are overlaid on top of each other by offsetting the original graph by the time it takes to reach the peak current. According to these results the peak current is independent of the way the maximum applied voltage is reached.

3.6.2 Effects of initial electron/ion concentration

Since the current spike happens at the beginning of each simulation, the electron/ion density is varied to asses its effect on the results. The initial densities of both electrons and positive ions are set to be equal, and for one atmosphere it is usually assumed to be on the order of $10^{13}\ m^{-3}$ [50]. However, in certain situations this may not be the case: e.g. different pressures, residual ionization, etc.

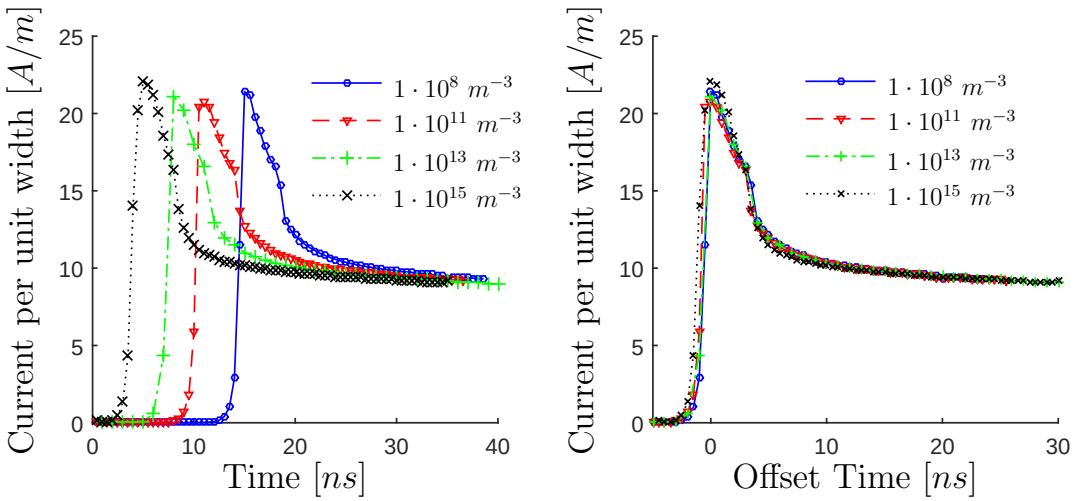

(a) The actual evolution of the discharge

(b) The graphs are offset in time to compare the profiles (the maximum is set to appear at 0 ns)

Figure 3.24: Current density per unit width for the exposed electrode - Initial particle densities.

Figure 3.24(a) shows the effect that the initial density of charged particles has on the current, while Figure 3.24(b) shows the overlaid graphs (similar to one in Figure 3.23). All other parameters (e.g. pressure, temperature, etc.) are kept the same for each simulation. As one can see from Figure 3.24(a), a lower initial number of particles leads to a time delay in the current spike. When this delay is accounted for, Figure 3.24(b) indicates that the initial concentration of charged particles only speeds up or delays the initial ionization process, but has little effect on the actual current developed. The time of the current peak varies from 5 ns for $1 \cdot 10^{15}\ m^{-3}$ to 15 ns

for $1 \cdot 10^8\ m^{-3}$. This means that for simulations of DBD configurations with short actuation time (e.g. nano-second pulse discharge actuators) the initial concentration of charged particles can have a significant impact on the results. However, for cases with longer actuation times (as is the case here) the initial concentration of the charged particles does not appear to change the resulting plasma behaviour.

3.6.3 Effects of electrode thickness on plasma development

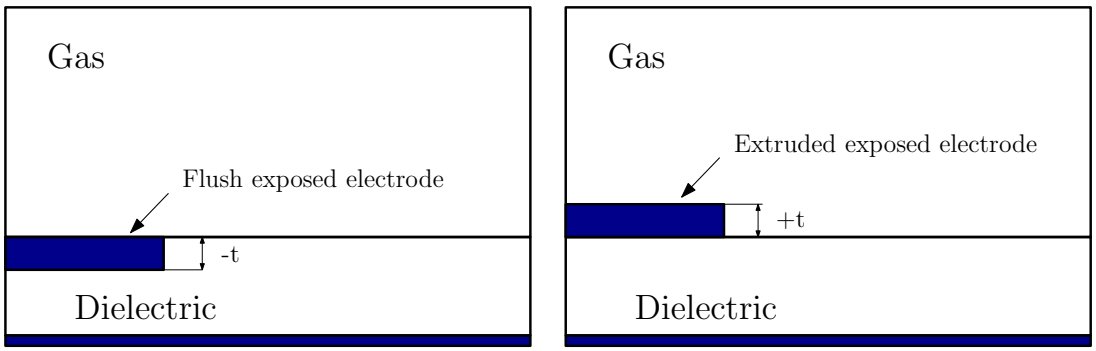

(a) Flush electrode (b) Extruded electrode

Figure 3.25: Schematics of different exposed electrode configurations.

All of the simulations in the previous sections use an exposed electrode with zero thickness. Although computationally simple, this is obviously aphysical and thus this section considers the effect of the thickness of the exposed electrode on the current per unit width. Both a flush (Figure 3.25(a)) and an extruded (Figure 3.25(b)) electrode configuration are examined. Figure 3.26(a) shows the currents when a constant 1 200 V is applied to an exposed electrode which is flush with the surface (i.e the electrode thickness is all within the dielectric). As one can see the maximum current is reduced as the thickness of the electrode is increased. Also, at the same time as the peak current is reduced the time to reach this peak is increased. The maximum current reduction can be explained by the reduction in the electric field strength at the edge of the electrode (Figure 3.26(b)), which for a zero thickness electrode peaks at $13.5 \cdot 10^7$

V/m and for an 8 μm thick electrode peaks at $6 \cdot 10^7$ V/m . As time progresses the sheath region moves further away from the edge of the electrode and the effect of the electrode thickness is reduced. This is seen in Figure 3.26(a) past approximately 30 ns when all the current curves approach the same value. It is noted that as the thickness increases the reduction in the maximum current becomes less pronounced. This suggests that past a given thickness any further increases in the thickness of the flush electrode will not result in any noticeable change in the observed maximum currents.

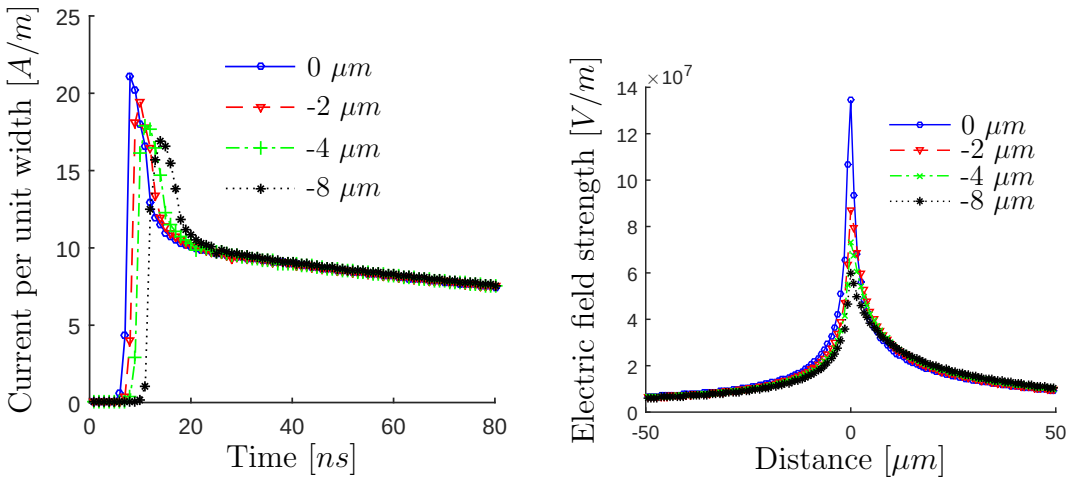

(a) Current density per unit width for the exposed electrode

(b) Electric field strength at 1 ns

Figure 3.26: Current density and electric field strength for the exposed electrodes with different thicknesses which are flush with the dielectric surface.

Figure 3.27(a) shows results for the case where the exposed electrode is protruded from the surface (i.e into the gas domain above the dielectric). As one can see the situation is different from the flush case. In this configuration there is no delay in the current peak. The peak current for the 2 μm thick electrode is slightly higher than for the 0 thickness electrode (23 A/m versus 21 A/m), while for the 4 μm thick electrode the current peaks at 8.9 A/m. After the initial current peak the current for the 4 μm thick case drops to approximately half that of the 0 μm thick electrode and

maintains this ratio for the duration of the simulation. The current for 2 μm thick electrode on the other hand initially drops to a level slightly below the 0 μm thick electrode case but then approaches the value of the of the 4 μm thick electrode at 80 ns. Figure 3.27(b) suggests that the initial electric field is slightly higher for a 2 μm extruded electrode than for a flush electrode ($15 \cdot 10^7$ V/m vs $13.5 \cdot 10^7$ V/m), which would explain the initial higher current values for the 2 μm case. However, it doesn't explain the low current values for the 4 μm case indicating an additional mechanism is present. Figure 3.28 shows the electron distribution with electric field

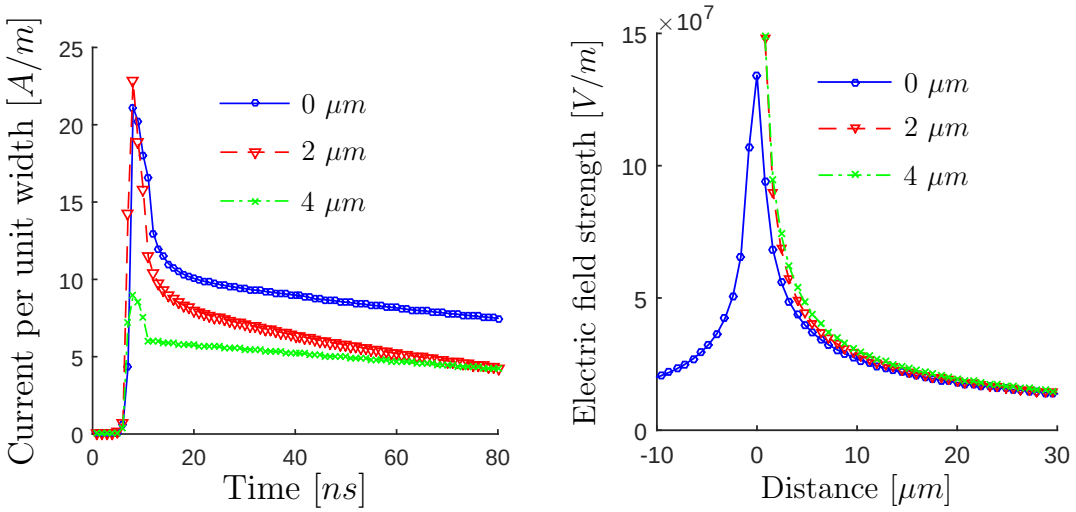

(a) Current density per unit width for the exposed electrode

(b) Electric field strength at 1 ns

Figure 3.27: Current density and electric field strength for the exposed electrodes of different thicknes which are extruded on top of the dielectric surface.

lines at 1 ns for the cases of extruded electrodes with different thickness. In the case of a zero thickness electrode the electrons tend to concentrate in the same location as high electric field (above $1.6 \cdot 10^8$ V/m). For the case of a 2 μm thickness electrode the maximum electric field encountered by the electrons is also above $1.6 \cdot 10^8$ V/m leading to an initial current spike. When the electrode thickness is set to 4 μm the maximum electric field encountered by the electrons is lower than in the previous two cases. This difference is enough to reduce the maximum current from 21-23 A/m to

8.9 A/m.

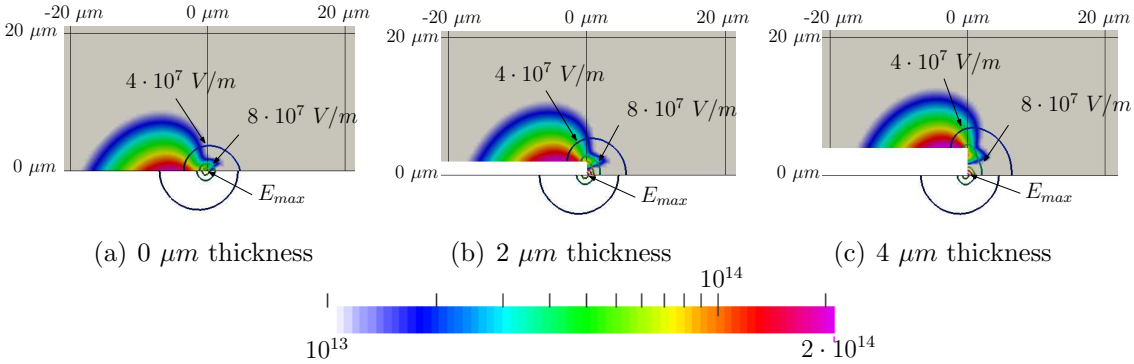

(a) 0 μm thickness (b) 2 μm thickness (c) 4 μm thickness

Figure 3.28: Comparison of electron concentration (N_e) and electric field (**E**) distribution at 1 ns for the extruded electrodes with different thickness. The electric field lines are in steps of $4 \cdot 10^7\ V/m$.

In summary, the change in the geometry of the exposed electrode changes the initial electric field distribution, which in turn has an impact on the initial plasma formation and in the case of an extruded electrode it also affects the later stages of plasma propagation. While the zero thickness electrode produces a large current spike, the simulations described in the next chapters are still performed using a zero thickness electrode.

Chapter 4

Simulation Results - Quiescent Flow - Effects of voltage sine wave on plasma development

For the continuous use of a SDBD PA, usually a periodic voltage waveform is used. Many research groups have tested different waveforms from sine waves in the kilohertz [18,37,50] or megahertz range [45] to nanosecond pulses in kilohertz range [3]. A test case with a sine voltage waveform applied at the exposed electrode will be analysed here to evaluate the plasma development for a DBD over a several cycles of this type of operation. The sine wave has an amplitude of 1200 V and period of 100 ns (10 MHz). The 10 MHz frequency is selected in the interest of time as each cycle takes approximately 80 hours to simulate (time steps are on the order of $1 \cdot 10^{-14}$ s). The results of a total of four periods are presented in this chapter. All boundary conditions are the same as shown in Table 3.1 (Section 3.2) (except for the exposed electrode which has the voltage sine wave applied as described above), including the initial ion and electron concentration of 10^{13} m^{-3} and a zero applied voltage at the grounded electrode. The domain size is changed to accommodate a larger plasma region, and it is set to 1 400 μm (gas and dielectric) in the horizontal direction and 300 μm in

vertical direction (gas domain). The refinement regions are also extended so as to maintain the same distance away from the outer boundaries.

4.1 Full sine wave cycle

Figure 4.1 shows the current and voltage comparison between a constant voltage and a single period of the sine wave. The first quarter phase of this cycle looks similar to 10 ns of a constant voltage when examining the current per unit width, with a similar peak value only delayed as seen Figure 4.1 (a). As mentioned in Section 3.6.1, this

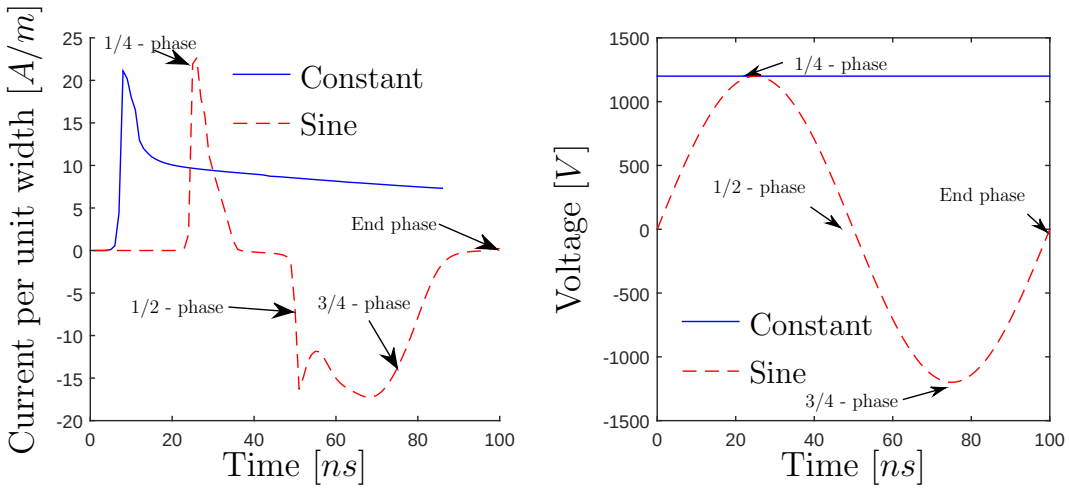

(a) Current

(b) Applied voltage profile

Figure 4.1: Current per unit width for the exposed electrode for different voltage profiles.

delay is due to the time it takes for the voltage to reach its peak value (see Figure 4.1 (b)). Past the quarter phase point the voltage starts to drop and so does the current. However, the current reaches zero at approximately 38 ns which is before the voltage reaches zero (50 ns) after which the current starts to lead the voltage. Since the dielectric acts as a capacitor and the plasma has some resistance to the current, the SDBD PA acts as a resistive-capacitive circuit (or RC-circuit). For RC-circuits it is typical for the current to lead the voltage. Therefore the current spike to a value of

approximately -15 A/m before the voltage reaches zero (1/2-phase) is expected . Once the voltage reaches its minimal value (3/4-phase) the current is already decreasing in magnitude. On this side of the voltage curve the current again approaches zero before the voltage does. One should also note that the circuit is "open" during the initial 22 ns of the sine wave since the voltage and electron concentration are too low to cause significant ionization and thus current discharge. Therefore there is no current during that time.

4.1.1 1/4-phase

During the first 1/4-phase of the sine wave the voltage rises to its peak value of 1200 V on the exposed electrode. Figure 4.2 shows the concentration of positive ions and electrons at 1/4-phase of the sine wave (25 ns). In addition, the concentration of ions and electrons for the case with a constant voltage at 8 ns are also included for comparison. As one can see the constant voltage case has an extra region of positive ions (Region A in Figure 4.2(a)), while the concentration of electrons is nearly identical for the two cases. The difference in the concentration of ions can

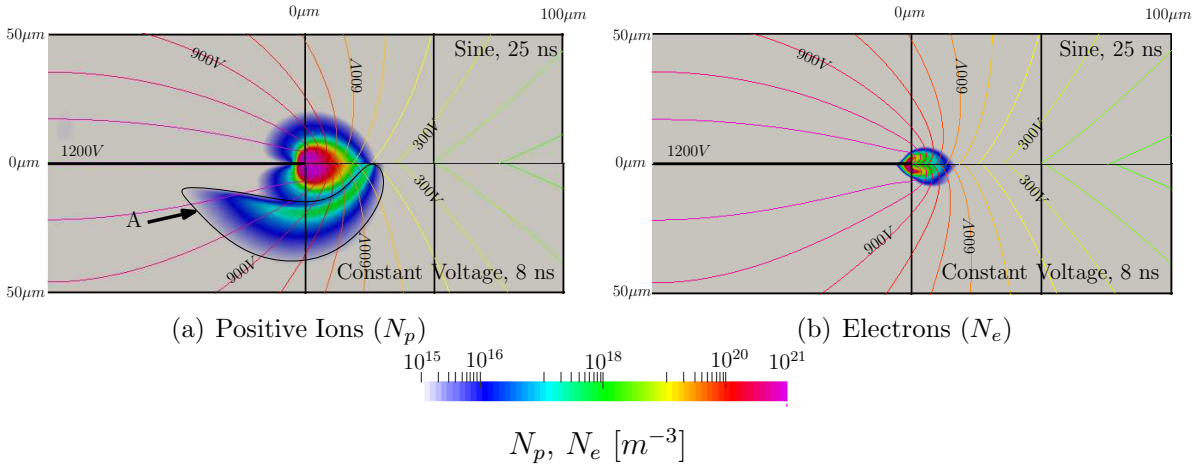

Figure 4.2: Concentration of charged particles at 1/4-phase with comparison to to constant voltage case.

be attributed to the initial concentration and the time needed to reach this state.

For the constant voltage case it takes only 8 ns for the ionization process to pick up, while for the sine-wave voltage it takes 25 ns. During the first 20 ns of the sine-wave the electric field is relatively weak and doesn't have enough strength to significantly affect the ions or cause the ionization process to begin. In the case of a constant voltage, the strong electric field is able to push the ions away from the surface of the electrode before the ionization process is significant enough for plasma to form. Once the plasma is formed it shields these ions from the electric field thereby preventing the dispersion of Region A.

4.1.2 1/2-phase

At the 1/2-phase of the cycle the voltage on the exposed electrode is reduced to 0 V. Between 1/4-phase and 1/2-phase the plasma behaves similarly to the constant voltage, that is the plasma continues to propagate away from the exposed electrode while charging the dielectric surface. However, as the voltage on the exposed electrode starts to drop, the dielectric surface ends up with the higher electric potential than the electrode itself causing a reversal in the current flow (which is observed in Figure 4.1 (a)). Figure 4.3 provides comparison of the concentration of ions and electrons between the constant voltage profile and the 1/2-phase (50 ns) of the sine-wave, when the voltage is at zero and the current has already reversed its direction. Using the ionization delay identified in Figure 4.2 (a) of approximately 17 ns, by the time the sine-wave voltage has reached the 1/2-phase voltage, the corresponding results for constant voltage are at 33 ns. At this point the profiles differ significantly. In the case of the constant voltage the plasma front propagates forward and the dielectric surface under the plasma has a surface potential of approximately 1200 V. For the sine-wave the voltage on the exposed electrode is at 0 V, while the maximum potential on the dielectric surface is 473 V. In addition, one can note that the direction of plasma flow is reversed: the maximum ion concentration and the electron lip are directed towards

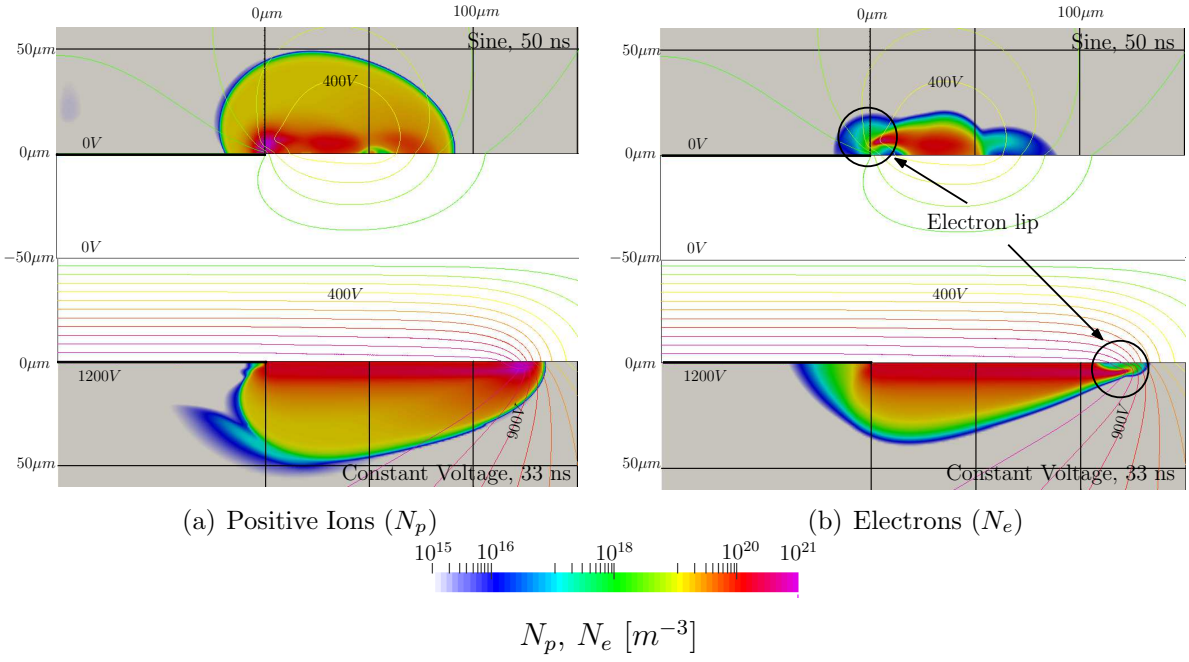

(a) Positive Ions (N_p)

(b) Electrons (N_e)

Figure 4.3: Concentration of charged particles at 1/2-phase with comparison to to constant voltage case.

the exposed electrode, while the rightmost extent seems to be depleting. This agrees with the current profile in Figure 4.1(a).

4.1.3 3/4-phase

Figure 4.4 shows the distribution of charged particles for the 3/4-phase and compares it to the constant voltage case. Even though the plasma under both a constant and a sine-wave voltage has a significantly different shape, the maximum concentration of positive ions is still on the order of 10^{21} m^{-3} for the two cases. The maximum concentration of electrons, however, is an order of magnitude lower at the 3/4-phase (10^{20} m^{-3} vs 10^{21} m^{-3}).

In Figure 4.4(a) Region B is noted which surround a region of positive ions approximately the same size ad extent of the positive ion region in Figure 4.3 (a). This region has moved slightly left along the electrode surface but has maintained a height of approximately 50 μm (same as 1/2-phase) and a length of approximately 124 μm

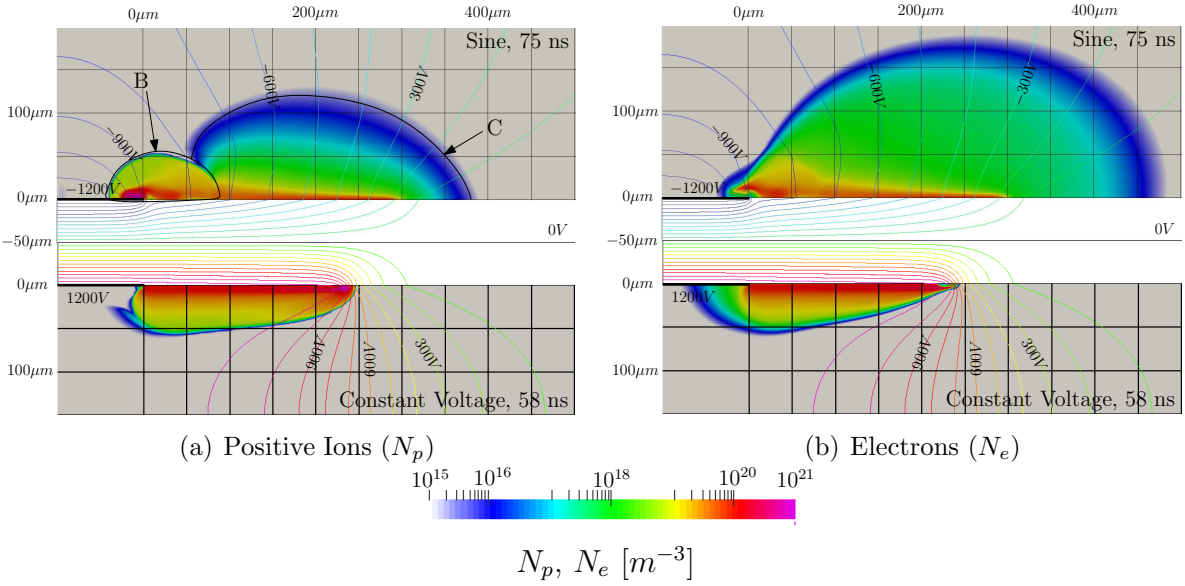

Figure 4.4: Concentration of charged particles at 3/4-phase with comparison to to constant voltage case.

(112 μm for 1/2-phase). This movement is consistent with direction of the applied voltage during this phase of the sine wave. However, in addition to the ions in Region B there is also a newly formed ion cloud - Region C. Region C has a lower ion concentration and is spread out further than Region B.

When comparing the electron distribution of the 3/4-phase (Figure 4.4 (b)) to the 1/2-phase (Figure 4.3 (b)) one notes that the electrons are spread out to a much larger area above the dielectric at 3/4-phase. This is because the dielectric surface becomes negatively charged due to oncoming electrons are repelled from the negatively charged exposed electrode. As the surface becomes more negatively charged more electrons are propelled further away from the electrode. Due to their high mobility, the electrons are dispersed in a wide angle away from the electrode resulting in a larger cloud of electrons thus allowing ionization of the neutral gas further away from the dielectric surface. Therefore, one obtains a positive ion cloud in region C which covers a region further than 100 μm away from the dielectric as compared to approximately 50 μm. The area of the highest concentration of electrons and ions still remains close to the

dielectric surface (within 25 μm) in both a constant and sine-wave applied voltage.

At this point it becomes harder to identify the sheath region while the plasma front and its direction become harder to quantify given the more diffuse nature of plasma cloud. As such, it is beneficial to talk about the extent of the plasma defined here as the presence of a significant quantity of charged particles (above 10^{15} m^{-3}).

4.1.4 End phase

At the end of the sine-wave cycle the applied voltage on the exposed electrode returns to zero. Figure 4.5 shows the concentration of charged particles at that time. The maximum concentration of charged particles is reduced when compared to the

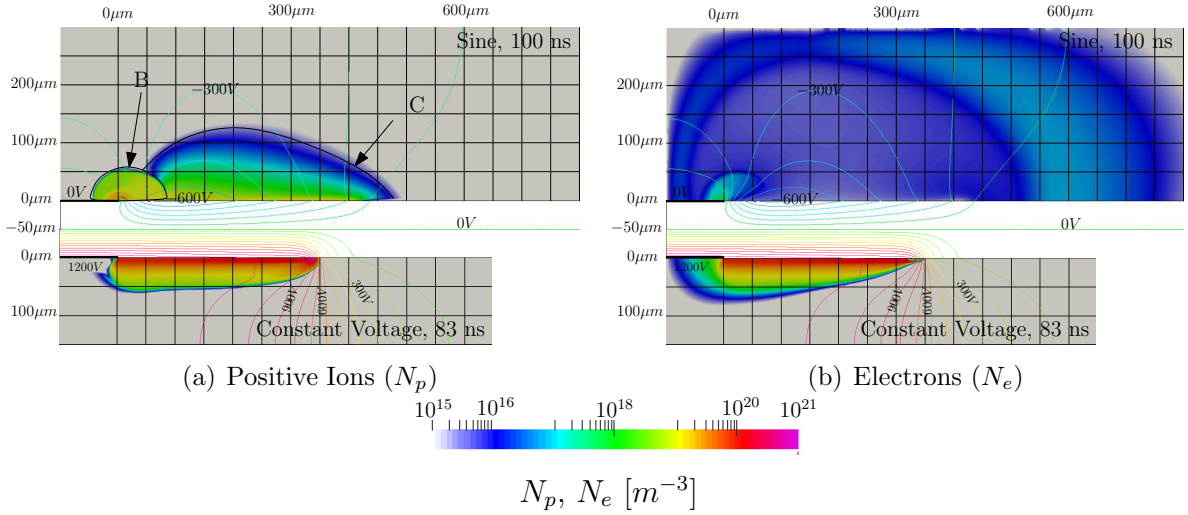

Figure 4.5: Concentration of charged particles at 3/4-phase with comparison to to constant voltage case.

previous 3/4-phase (from $5.5 \cdot 10^{20}$ m^{-3} to $4.8 \cdot 10^{19}$ m^{-3} for ions and from $9.8 \cdot 10^{19}$ m^{-3} to $6.9 \cdot 10^{17}$ m^{-3} for electrons), though the overall shape of the positive ion cloud remains approximately the same. Regions B and C can still be identified. On the other hand, the electrons are dispersed a significant distance away from the dielectric surface which now has a residual negative charge of approximately 600 V. Due to this some of the electrons are absorbed through the exposed electrode, while others are

pushed towards the domain boundaries. Due to the high mobility of the electrons their concentration is significantly lower than that of the positive ions ($6.9 \cdot 10^{17}\ m^{-3}$ for electrons and $4.8 \cdot 10^{19}\ m^{-3}$ for ions). The electron concentration, however, is still four orders of magnitude higher than the initial value ($10^{13}\ m^{-3}$) and covers a much larger area than in the case of constant voltage at the same time after ionization. This means that the next cycle will have higher initial ionization rates than those seen for a constant applied voltage, or even those that consider another sine-wave voltage but starting again from the initial no-plasma conditions.

4.2 Multiple cycles

Figure 4.6 shows the current and applied voltage at the exposed electrode for four cycles. One can note that the currents vary from cycle to cycle. The maximum current (on the order of 90 A/m) occurs during the positive part of the second cycle and is significantly higher than that observed in the initial cycle (22.7 A/m). After the maximum in the second cycle the currents are reduced to approximately 40 A/m for the third and fourth cycles. As mentioned in the previous section, the concentration of electrons and ions at the end of the first cycle is significantly higher and more spread out than when starting the DBD initially. This facilitates ionization during the second cycle thus leading to a higher current spike. This also indicates that at

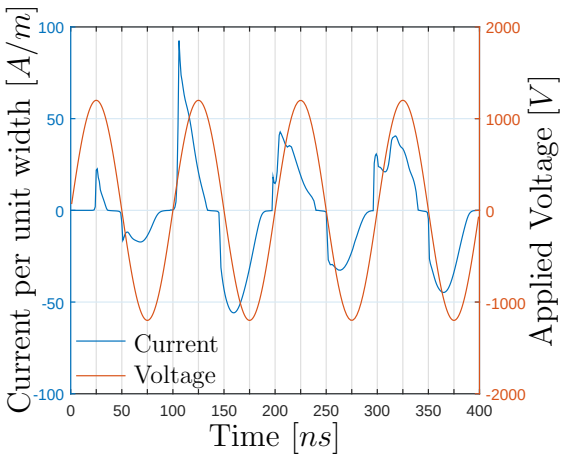

Figure 4.6: Current density per unit width of the exposed electrode for sine wave with multiple cycles.

least for this configuration the first two cycles are not representative of the average operation of the plasma actuator. Figure 4.7 - 4.8 further support this statement.

Figures 4.7 and 4.8 show the positive ion and electron density for four cycles of the sine wave. During the first half of the second cycle the plasma propagates 500 μm (Figure 4.7 and 4.8 (e) and (f)) from the edge of the exposed electrode in a manner similar to the that seen in Figures 4.2 and 4.3. The plasma has a well defined

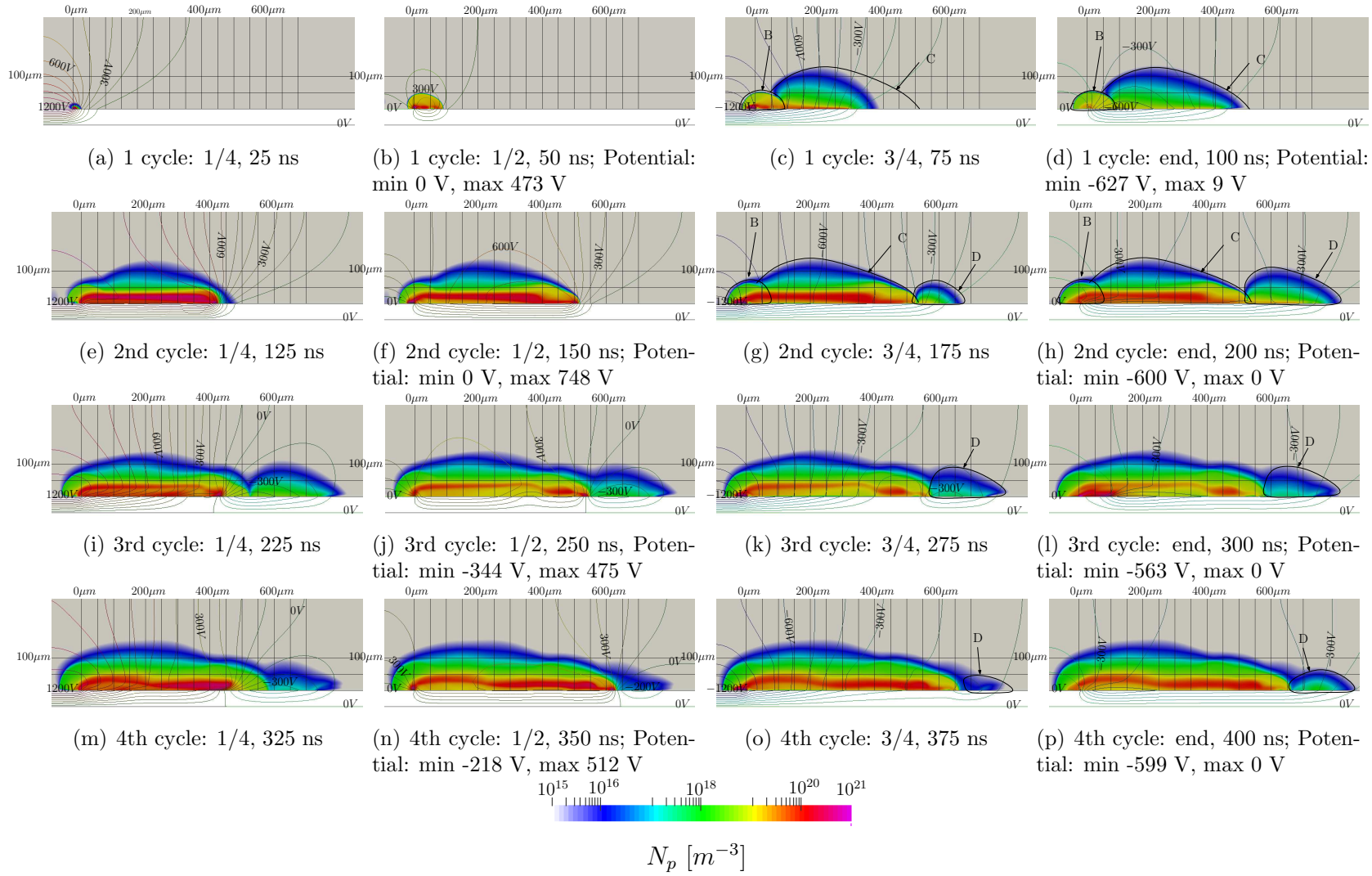

(a) 1 cycle: 1/4, 25 ns

(b) 1 cycle: 1/2, 50 ns; Potential: min 0 V, max 473 V

(c) 1 cycle: 3/4, 75 ns

(d) 1 cycle: end, 100 ns; Potential: min -627 V, max 9 V

(e) 2nd cycle: 1/4, 125 ns

(f) 2nd cycle: 1/2, 150 ns; Potential: min 0 V, max 748 V

(g) 2nd cycle: 3/4, 175 ns

(h) 2nd cycle: end, 200 ns; Potential: min -600 V, max 0 V

(i) 3rd cycle: 1/4, 225 ns

(j) 3rd cycle: 1/2, 250 ns, Potential: min -344 V, max 475 V

(k) 3rd cycle: 3/4, 275 ns

(l) 3rd cycle: end, 300 ns; Potential: min -563 V, max 0 V

(m) 4th cycle: 1/4, 325 ns

(n) 4th cycle: 1/2, 350 ns; Potential: min -218 V, max 512 V

(o) 4th cycle: 3/4, 375 ns

(p) 4th cycle: end, 400 ns; Potential: min -599 V, max 0 V

Figure 4.7: Evolution of positive ion density distribution $[m^{-3}]$. The contour lines are the electric field potential with 0 V for bottom surface (grounded electrode) and 100 V difference between the lines. The exposed electrode is at 1200 V at 1/4-phase, -1200 V at 3/4-phase, 0 V at 1/2-phase and at the end of each cycle.

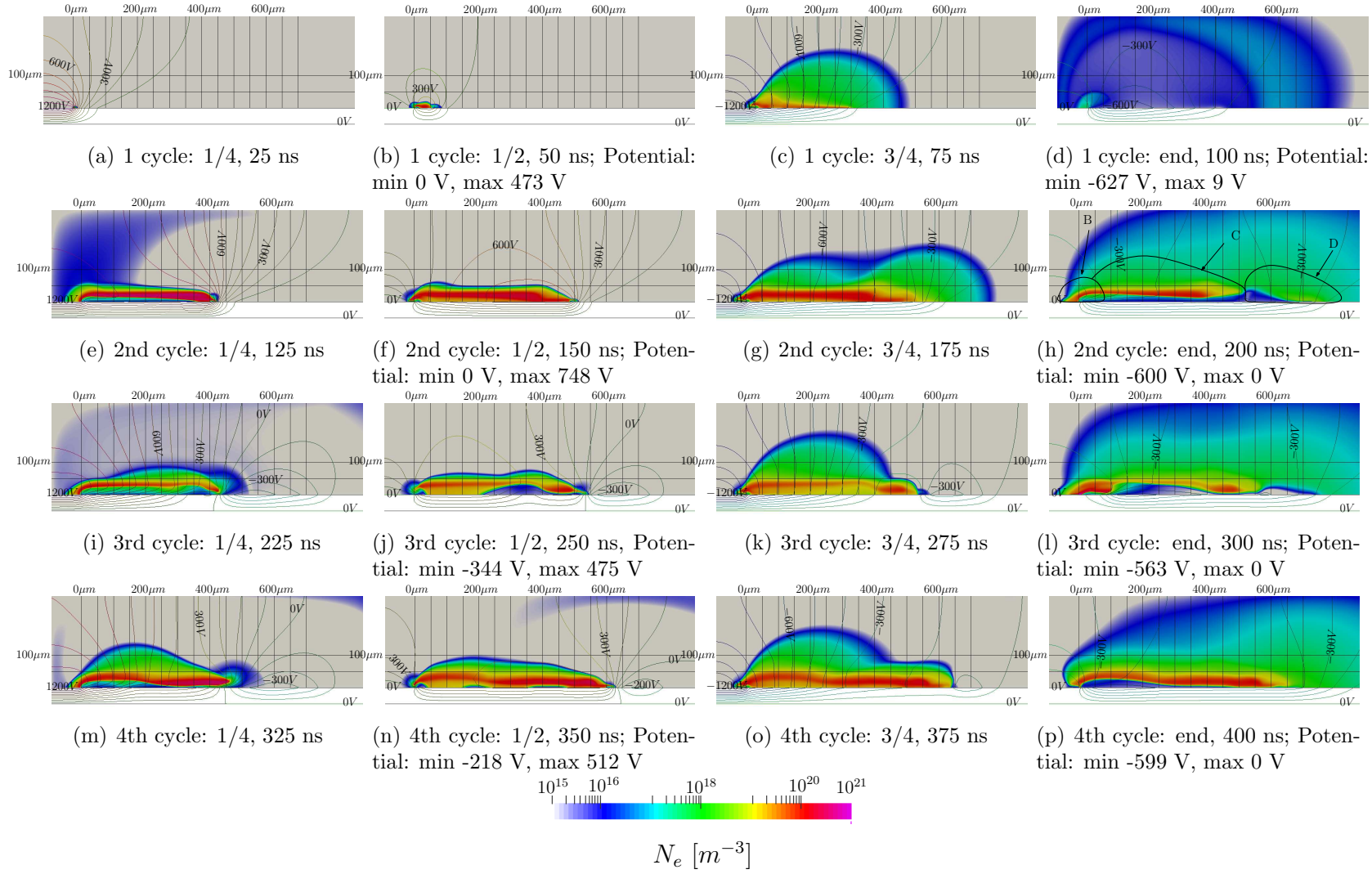

(a) 1 cycle: 1/4, 25 ns

(b) 1 cycle: 1/2, 50 ns; Potential: min 0 V, max 473 V

(c) 1 cycle: 3/4, 75 ns

(d) 1 cycle: end, 100 ns; Potential: min -627 V, max 9 V

(e) 2nd cycle: 1/4, 125 ns

(f) 2nd cycle: 1/2, 150 ns; Potential: min 0 V, max 748 V

(g) 2nd cycle: 3/4, 175 ns

(h) 2nd cycle: end, 200 ns; Potential: min -600 V, max 0 V

(i) 3rd cycle: 1/4, 225 ns

(j) 3rd cycle: 1/2, 250 ns, Potential: min -344 V, max 475 V

(k) 3rd cycle: 3/4, 275 ns

(l) 3rd cycle: end, 300 ns; Potential: min -563 V, max 0 V

(m) 4th cycle: 1/4, 325 ns

(n) 4th cycle: 1/2, 350 ns; Potential: min -218 V, max 512 V

(o) 4th cycle: 3/4, 375 ns

(p) 4th cycle: end, 400 ns; Potential: min -599 V, max 0 V

Figure 4.8: Evolution of electron density distribution $[m^{-3}]$. The contour lines are the electric field potential with 0 V for bottom surface (grounded electrode) and 100 V difference between the lines. The exposed electrode is at 1200 V at 1/4-phase, -1200 V at 3/4-phase, 0 V at 1/2-phase and at the end of each cycle.

sheath region for the 1/4-phase of the second cycle and is able to charge the dielectric surface behind the plasma front to shield itself from the electric field. The positive ion Regions B and C (Figure 4.5 and Figure 4.7 (d)) have combined into a single cloud. At the 1/2-phase of the second cycle (Figure 4.7 and 4.8(f)) the dielectric is positively charged and the maximum residual potential is at 748 V.

The electron density also has similar features during the 1/4 - and 1/2- phases of cycles 1 and 2 although for the 2nd cycle the overall extent of the electron cloud is significantly larger. However, in Figure 4.8 (e) the maximum concentration is still close to the surface and the electron lip is visible at the plasma front. At the 1/2-phase point the electron lip has changed position to the exposed electrode (Figure 4.8 (f)) indicating a reversal of the current as seen Figure 4.3.

During the 3/4-phase of the second cycle (Figure 4.7(g)) the positive ions form two distinct clouds similar to those seen during the the 1st cycle. One extends from 0 μm to 500 μm (Region B and C) and the other from 500 μm onwards (Region D). The first cloud (Region B and C) has a similar shape as the concentration at the end of the positive part of the cycle (Figure 4.7(f)), but with lower maximum concentration. The second cloud (Region D) is formed as if the end of the first cloud acts as the edge of the exposed electrode and thus shape of the second cloud is similar to Region C of the first cycle (Figure 4.4, Figure 4.7(c)). However, the high value of the residual positive potential at 1/2-phase point (748 V) reduces the extent of positive ion cloud propagation along the dielectric during the negative part of this 2nd cycle making Region D somewhat smaller than Region C in the 1st cycle (Figure 4.7(g) and Figure 4.7(c)).

Since electrons are much lighter than positive ions they end up covering a larger region (Figure 4.8(h)) than the positive ions by the end of the 2nd cycle, similar to the behaviour observed for the first cycle (Figure 4.8(d)). However, the negative residual voltage in the second cloud region (due to the negatively charged dielectric in

Region D) results in a relatively low concentration of electrons. This means there is a lack of available electrons for ionization in this region. The lack of electrons, large distance from the edge of the second cloud to the exposed electrode and residual voltage of -600 V at the end of the second cycle further impede the propagation of positive ions during the following cycles.

During the third and fourth cycles (Figure 4.7 from (i) to (p)) the positive ions don't propagate much further than during the second cycle indicating that for the given test configuration the plasma is reaching its propagation limit. Figure 4.6 also suggests that the system has achieved an approximately stable (or steady) operational state with a maximum current during the positive and negative parts of the cycles of approximately 43 and -32 A/m for the 3rd cycle and 40 and -45 A/m for the 4th cycle.

The low residual voltage, lack of electrons for ionization in Region D, and a relatively large distance from the exposed electrode again at an applied voltage of 1200 V results in a situation where there is not enough potential to create another plasma sheath to increase the size of the main body of the positive ions at the beginning of the 3rd cycle and beyond (compare Figure 4.7(e) to Figures 4.7(i) and (m)). Even by the end of the positive part of the fourth cycle (Figure 4.7(n)) the residual potential in the second cloud remains at -218 V. Comparing Figures 4.7(m) to (p) with Figures 4.7(i) to (l) indicates that during the 4th cycle the positive ion cloud behaves in a manner similar to that observed during the 3rd cycle again suggesting that an approximate steady state is being reached. In the case of the electron density, the second cloud is not as distinct and is merged with the first cloud by the end of the fourth cycle (Figure 4.8(p)).

Figure 4.9 shows the surface charge for each of the cycles at quarter-phase points. If there is not enough charged particles flowing towards the surface to neutralise the surface charge during voltage phase changes, then the next cycle would be affected by

the presence of these charges, through the residual potential that is generated by these surface charges. As one can see from Figure 4.9, in the region further than 500 μm away from the electrode after the 2nd cycle the surface is negatively charged through all phases. According to Figure 4.9(a) the surface is positively charged for the first 400 μm after the first cycle (the only exception being a small region from 300 to 375 μm during the 3rd cycle which has a small negative charge). From 400 to 900 μm at the 1/4-phase, cycles three and four have a significant negatively charged surface which restricts further plasma propagation. The higher magnitude of the negative surface charges results in stronger potential which pushes the electrons away from the surface resulting in regions of low electron concentration near dielectric surface and larger electron clouds dispersed throughout the domain at the end of each cycle (Figure 4.8 (d), (h), (l), (p)).

Figure 4.9(b) shows that past the first cycle the dielectric surface is predominantly positively charged but that by the 3/4-phase point the surface has become predominantly negatively charged (Figure 4.9(c)). This is consistent with the movement of both the positive ions and electrons under the changing applied electric field. Figure 4.9(d) shows a significant difference in the surface charge distribution between the 1st and 2nd cycles. However, the difference in the surface charge distribution between the 2nd and 3rd cycles is smaller and continues to decrease even further between the 3rd and 4th cycles further suggesting a quasi-steady state is being reached.

As illustrated in this chapter a periodically applied voltage can lead to plasma behaviour that changes from cycle to cycle and thus care needs to be taken to address these differences. The results for current per unit width, the positive ion and electron densities, and the surface charge all suggest that these differences start to decrees past the 2nd cycle and approach a steady state behaviour by cycle four.

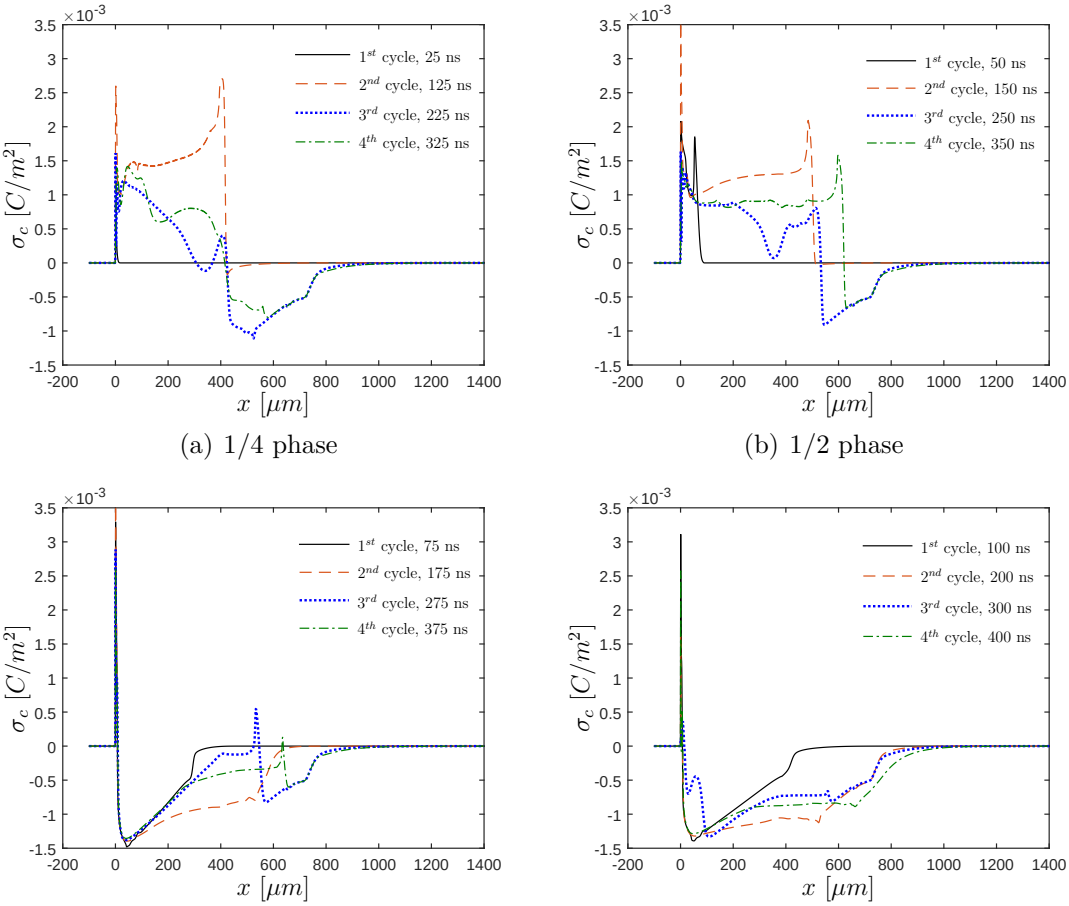

(a) 1/4 phase

(b) 1/2 phase

(c) 3/4 phase

(d) End phase

Figure 4.9: Comparison of surface charge density between different cycles.

Chapter 5

Simulation Results: Supersonic flow - Shock Effect on Plasma

5.1 Initial and Boundary Conditions for Test Cases

To study what happens to a plasma when it encounters a shock the pressure and temperature in the fluid region are separated into two regions representing conditions ahead (P_1, T_1) and behind (P_2, T_2) a normal shock as shown in Figure 5.1. The upstream pressure (P_1) and temperature (T_1) are set to 100 kPa and 300 K for all the simulations, while the downstream pressures and temperatures are found using the normal shock equations. Table 5.1 lists the simulated shock cases.

Mach Number	Pressure (P_2) [kPa]	Temperature (T_2) [K]
1.3	180.5	357.3
1.5	245.8	396.1
2.0	450.0	506.3

Table 5.1: Pressure and temperature for the fluid region downstream of the shock for the considered Mach numbers.

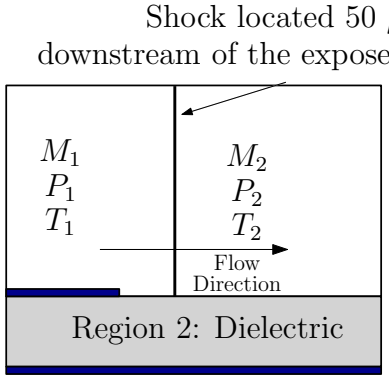

Figure 5.1: Computation domain for the simulations with shock located 50 μm downstream of the exposed electrode.

These simulations do not model the effect of the plasma actuator on the fluid flow and as such the pressure and temperature remain constant throughout the simulations. The domain size is the same as the one shown in Figure 3.1 with a flush exposed electrode of 0 mm thickness. The applied voltage at the exposed electrode is a constant 1200 V and the grounded electrode is set to 0 V. The fluid domain contains neutral particles (N_2), positive ions and electrons. The initial concentration of charged particles is set to 10^{13} m^{-3}. The mesh is the same as the one described in Section 3.1 and contains 117 118 elements in the fluid region, 23 548 elements in the dielectric region and the minimum element size is 0.5 μm.

5.2 Normal Shock Results

Figures 5.2 to 5.4 show the evolution of the positive ion concentration for the three Mach number considered compared to a no-shock (Mach 0) solution. Figure 5.2 indicates that at Mach 1.3 the ionization front is slowed down as it passes through the shock which becomes noticeable by 50 ns (Figure 5.2(d)). However the distribution of the positive ions is similar to the case without a shock. The effect of the shock is more pronounced at a Mach number 1.5. The reduction in the speed of the plasma sheath

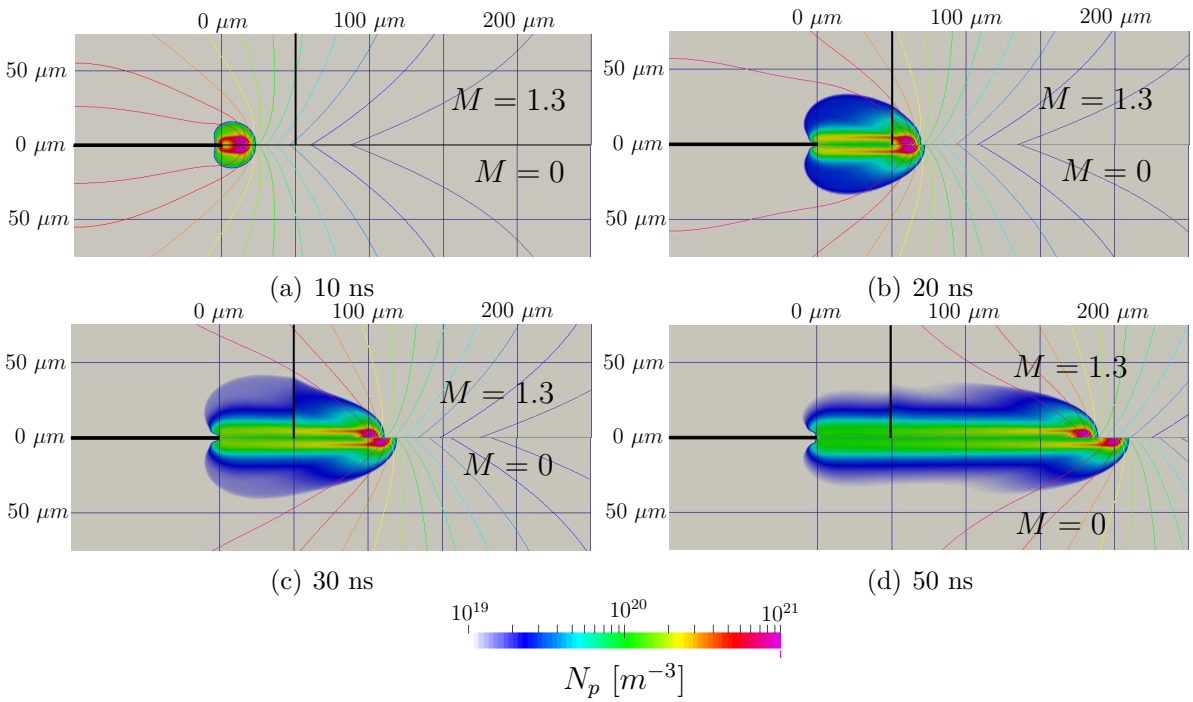

Figure 5.2: Evolution of positive ion density distribution $[m^{-3}]$ for shock case with Mach 1.3 compared against quiescent flow case. The contour lines are the electric field potential: 0 V for grounded electrode and 1200 V for the exposed electrode. The origin of horizontal axis is located at the edge of the exposed electrode $(0\mu m)$.

becomes noticeable the moment the plasma reaches the shock (20 ns, Figure 5.3(b)). The results at 30 and 50 ns also show that the positive ions do not reach as far along the dielectric surface as in the case of no-shock. However, unlike at Mach 1.3, in the case Mach 1.5 the positive ions propagate upwards along the dowstream side of the shock itself. This is also the case at Mach 2 (Figure 5.4) as once the plasma front reaches the shock, the propagation speed starts to drop and the positive ions start to propagate upwards along the shock itself. For the weaker shock strengths (Mach 1.3, Mach 1.5) the high concentration of ions (above 10^{21} m^{-3}) behind the shock indicate that the ionization process is still able to continue. However, at Mach 2 the concentration of positive ions drops to below approximately 10^{21} m^{-3} by 30 ns and at 50 ns the maximum positive ion concentration only reaches 10^{20} m^{-3} while at the dielectric surface-shock intersection the concentration of positive ions drops to below

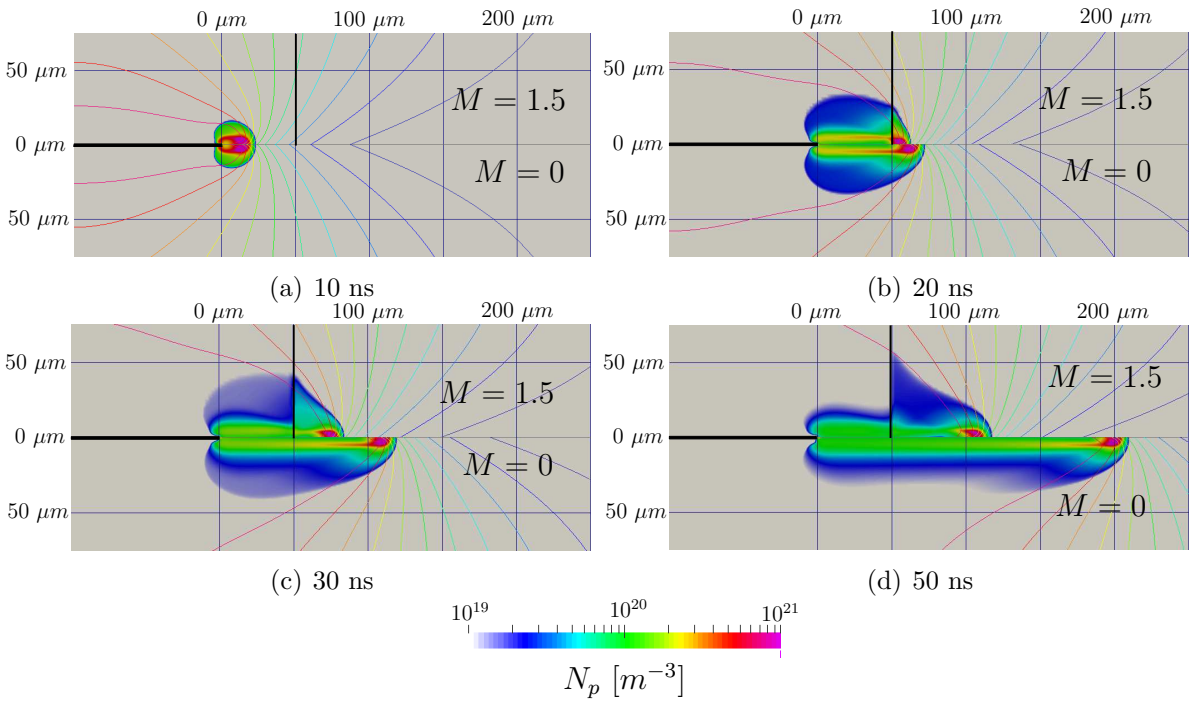

Figure 5.3: Evolution of positive ion density distribution $[m^{-3}]$ for shock case with Mach 1.5 compared against quiescent flow case. The contour lines are the electric field potential: 0 V for grounded electrode and 1200 V for the exposed electrode. The origin of horizontal axis is located at the edge of the exposed electrode $(0\mu m)$.

10^{19} m^{-3}. It should be noted that for the Mach 2 case the value of E/P drops from 2400 $(V/m)/Pa$ ahead of the shock to 533 $(V/m)/Pa$ behind the shock.

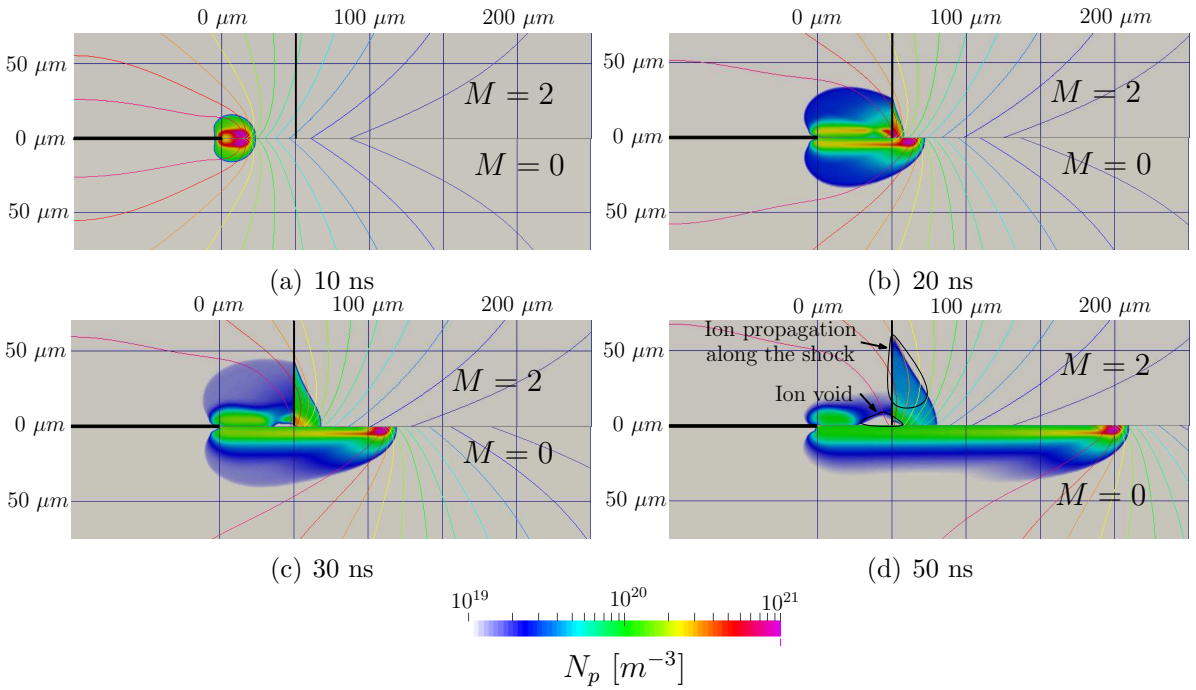

Figure 5.4: Evolution of positive ion density distribution $[m^{-3}]$ for shock case with Mach 2 compared against quiescent flow case. The contour lines are the electric field potential: 0 V for grounded electrode and 1200 V for the exposed electrode. The origin of horizontal axis is located at the edge of the exposed electrode $(0\mu m)$.

One might assume that such a severe reduction in positive ion concentration is due to a lack of ionization, but as shown in Figure 5.5, ionization is still occurring at 50 ns. Furthermore, the rate of ionization is comparable both before and after the shock at approximately 10^{30} $m^{-3}s^{-1}$. Although the ionization is still occurring, the maximum magnitude of ionization at 50 ns is below the maximum value observed at 20 ns by a few orders of magnitude leading to the reduction in the observed plasma propagation speed. However, because ionization is still occurring, the positive ion void observed at Mach 2 at 50 ns (Figure 5.4(d)) requires further explanation.

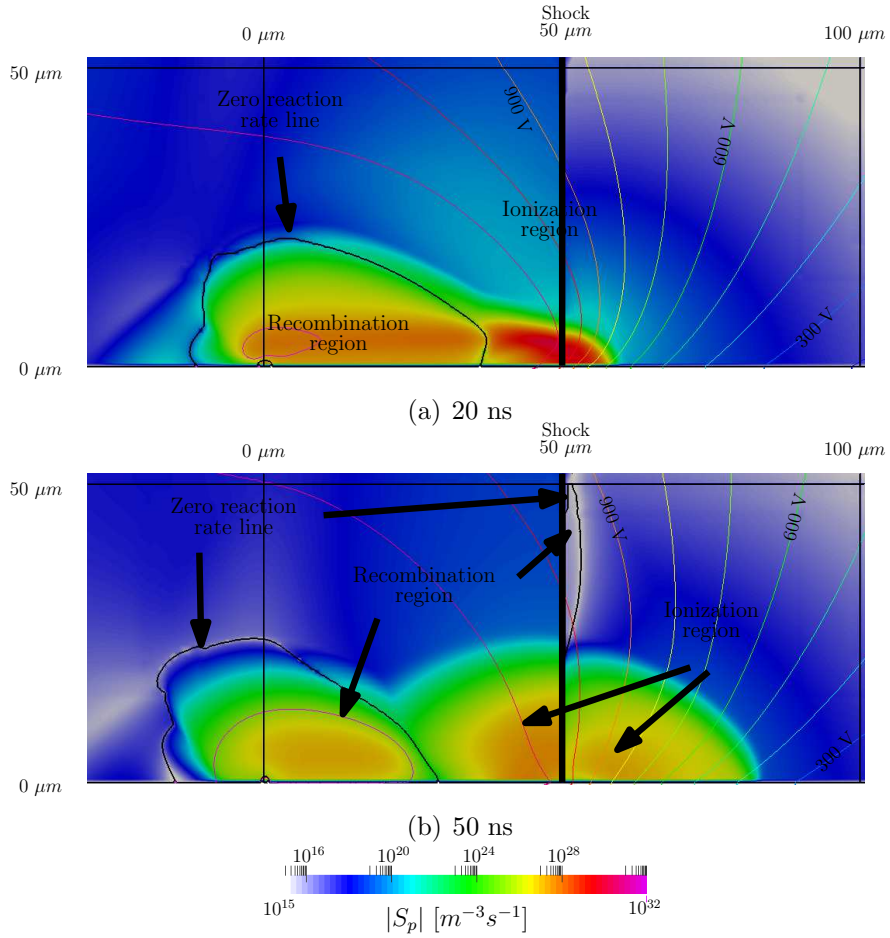

Figure 5.5: Mach 2 ionization/recombination rate.

Figure 5.6 is similar Figure 5.5 but shows the ionization/recombination rate divided by the magnitude of the ions' velocities (including the vectors of the ions'

velocities at both 20 ns and 50 ns). As one can see this ratio is a few orders of magnitude higher within the plasma region near shock at 20 ns than at 50 ns (10^{29} m^{-4} vs 10^{23} m^{-4}). This means that positive ion production is significantly higher than ion migration at 20 ns while at 50 ns positive ion migration becomes a more significant factor. Due to the shape of the electric potential lines, positive ions are forced not simply from the region upstream of the shock into the downstream region, but also upwards and away from the dielectric leading to the lack of positive ions observed at the root of the shock observed in Figure 5.4(d). The propagation of positive ions along the shock and their persistent presence there is a result of the positive ions being forced downstream by the electric field combined with the lack of electrons with which these ions could recombine as shown by the evolution of electron distribution (Figure 5.7). Furthermore, the lower mobility of the positive ions in the downstream region due to higher gas density created by the shock (the ion mobility is inversely proportional to the gas density, Eq. 2.29) means that the positive ions that migrate into this region tend to stay there.

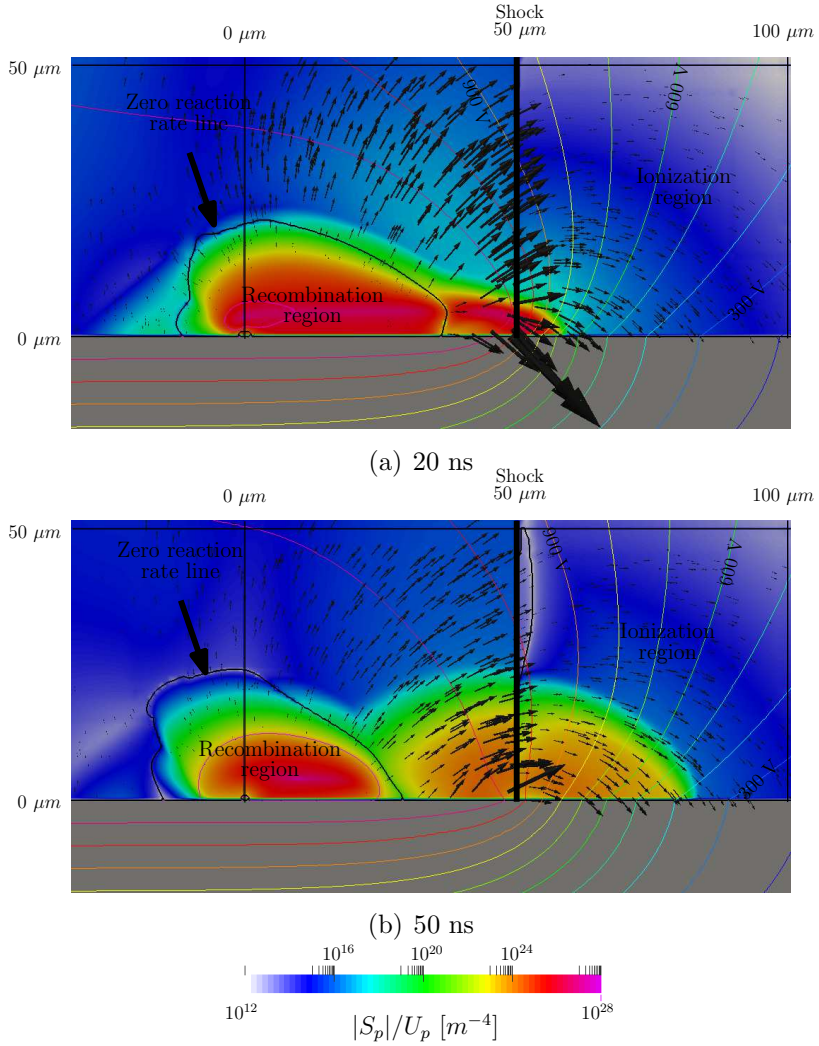

Figure 5.6: Mach 2, ionization/recombination rate devided by ion speed.

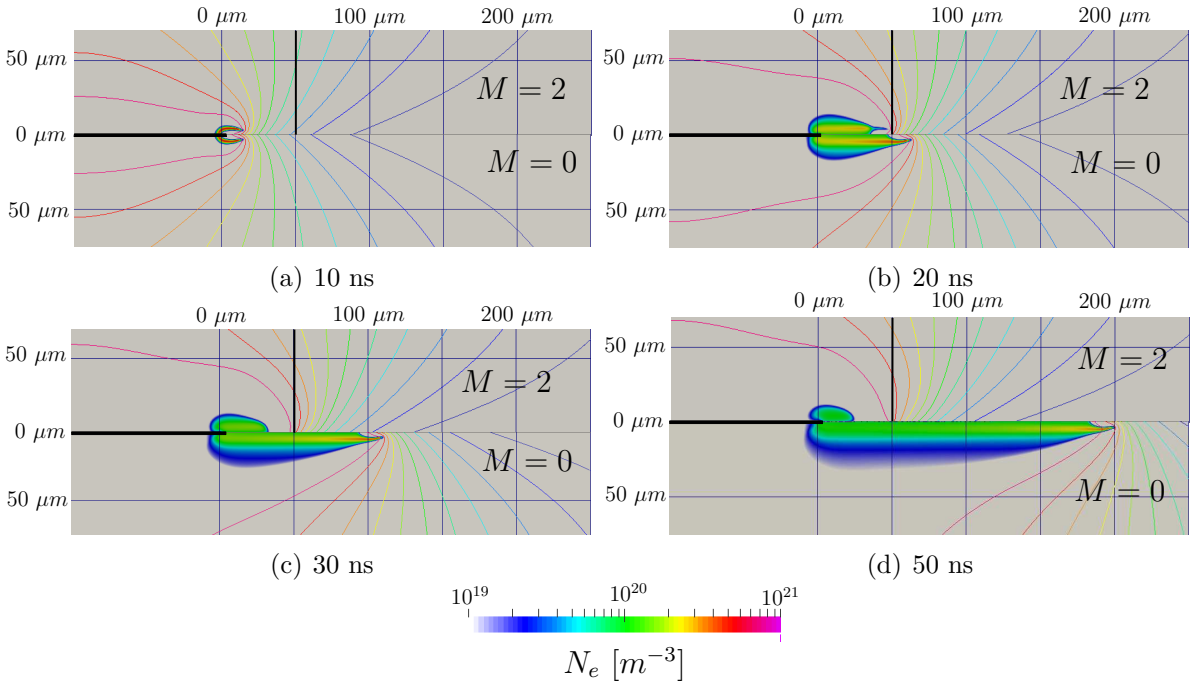

Figure 5.7: Evolution of electron density distribution $[m^{-3}]$ for shock case with Mach 2 compared against quiescent flow case. The contour lines are the electric field potential: 0 V for grounded electrode and 1200 V for the exposed electrode. The origin of horizontal axis is located at the edge of the exposed electrode $(0\mu m)$.

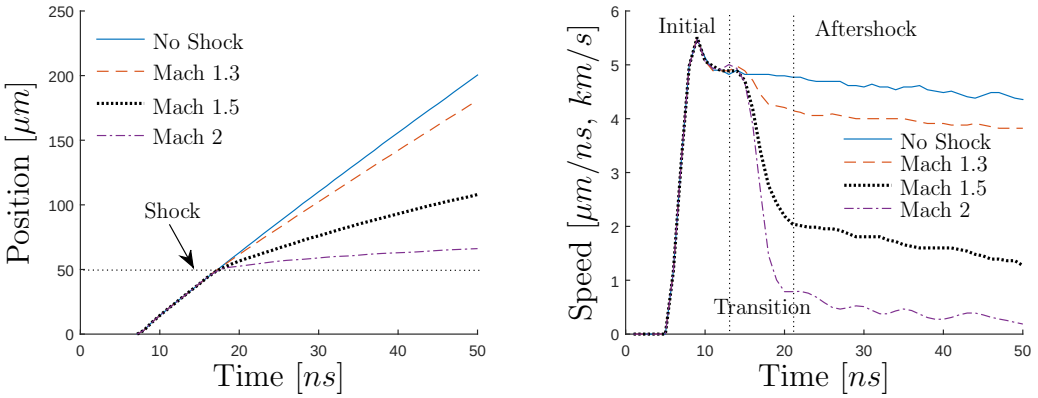

(a) Approximate position of plasma front

(b) Speed of plasma front propagation

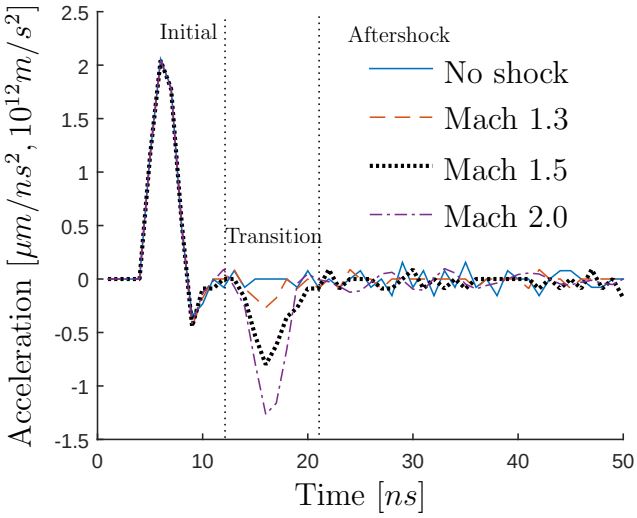

(c) Acceleration of plasma front propagation

Figure 5.8: Estimates of plasma front position and its speed for different shock conditions.

Figure 5.8 shows the position, speed, and acceleration of the plasma sheath for the Mach numbers considered. From Figure 5.8(a) one can see that it takes approximately 17 ns for the plasma to reach the shock before the shock alters the plasma behaviour. Prior to this time the plasma front behaves in the same fashion as seen in Figure 3.17(b) where once the ionization starts the plasma front speed peaks at approximately at 5.5 km/s at then settles to an approximately constant value of 5 km/s as shown in Figure 5.8(b). Also shown from the plasma front speed graph one

Mach Number	Transition (nm/ns^2)	After-shock (nm/ns^2)
<1	-78	-12
1.3	-267	-14
1.5	-800	-24
2.0	-1264	-19

Table 5.2: Plasma front acceleration as it passes through the shock (transition) and once it passed through the shock (after-shock).

can define three phases: initial (same as no-shock case, 0- 13 ns), transition (13-21), after-shock (after 21 ns). During the initial phase the plasma front position, speed and acceleration behaviours are approximately identical between the four test cases, since the plasma front is yet to reach the shock.

The transition phase of the graphs corresponds to when the plasma front passes through the shock (13-21 ns). During this period the acceleration graph indicates the main difference between the four cases, with Mach 2 showing the highest deceleration, which corresponds to the steepest slope on the speed graph after the initial phase. Table 5.2 shows that the peak acceleration during transition varies from -267 nm/ns^2 at Mach 1.3 to -1264 nm/ns^2 at Mach 2. This due to the fact that the ionization process in the downstream region is reduced due to the higher pressure and density of the medium behind the shock, which leads to a reduction of the plasma front propagation speed. This speed change happens only during the transition through the shock, hence the extra deceleration during this period. This deceleration peak is proportional to the strength of the shock and thus the Mach number.

The after-shock region starts after 21 ns and can be characterised by a low magnitude deceleration of the plasma front of approximately 12 to 24 nm/ns^2. This value is independent of the Mack number and even the presence of the shock.

The plasma speed reduction due to the presence of a shock is also reflected in the current per unit width as shown in Figure 5.9. In Chapter 3 it was shown that

after an initial peak the current per unit width decays at an approximate constant rate (Figure 3.18 and 5.9 no-shock). Figure 5.9 shows that the presence of a shock adds and additional step drop in the current. The stronger the shock the larger this second drop in the current. For example, at Mach 1.3 as the plasma hits the shock (at approximately 17 ns) the current suddenly drops from approximately 11 A/m to 8.6 A/m, while there is no such change for the no-shock case. After this sudden step change both the Mach 1.3 and no-shock cases exhibit a gradual lowering of the current. It can also be observed that the second step drop in current increases with increasing Mach number where at Mach 1.5 this difference is between approximately 11 A/m to 4.1 A/m, while at Mach 2 it drops to 0.9 A/m.

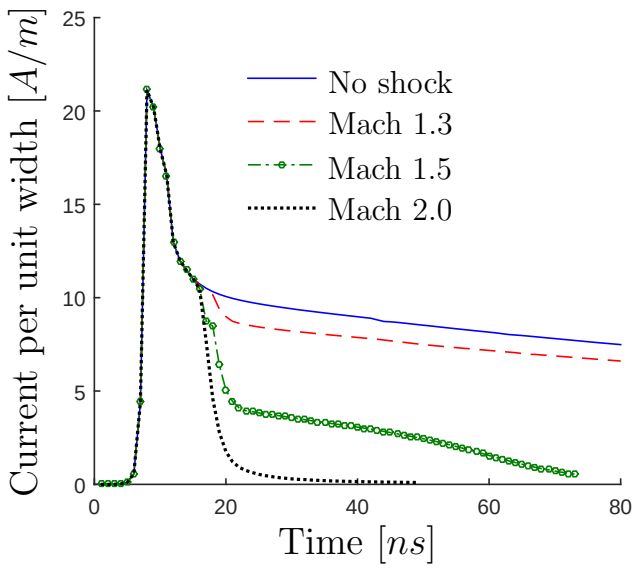

Figure 5.9: Current density as a function of time for different Mach numbers.

Figure 5.10 shows the ratio of the electric field strength to the pressure for Mach 1.5 and no-shock cases (where recalling that the ionization parameter α is a function of this ratio, see Eq. 2.32). As seen from Figure 5.10(a) at 10 ns the region upstream of the shock (between the edge of the exposed electrode and the shock) is the same for the case with and without shock with the ratio reaching as high as 1000 (V/m)/Pa.

However, downstream of the shock this value is an order of magnitude lower for the Mach 1.5 case than for the no-shock case indicating that at the start as plasma begins to approach the shock location the ionization process is slowed. By 20 and 30 ns (Figures 5.10(b) and (c)) the plasma front has passed through the shock and peak E/p values between the shock and no-shock cases are different by approximately 500 (V/m)/Pa. Furthermore the distribution of the electric-field-to-pressure ratio at the plasma front is no longer the same between the two cases. There is another region of elevated values just upstream of the shock location 50 μm above the dielectric surface in the Mach 1.5 case. Despite this region of high E/P this does not result in high levels of ionization due to lack of electrons above 25 μm as shown in Figure 5.11. Therefore this provides an additional indication that any increase in the concentration of positive ions in the region immediately downstream of the shock and well above the dielectric is due to diffusion and not ionization.

However, this region disappears by 50 ns (Figure 5.10(d)) as the electric field in this region ahead of the shock weakens as the plasma sheath moves further downstream.

Figure 5.12 shows the charge densities between Mach 1.5 and no-shock case. The maximum value of the charge density is maintained above 100 C/m^3 for both cases as both the ion and electron densities are reduced by the same amount when a shock is present. At 10 ns the distribution of the charge density is the same between the two cases (shock at Mach 1.5 and no-shock). At 20 ns the distribution of the charged particles upstream of the shock is similar between the two cases, while downstream of the shock the charge density for the shock case starts to lag behind the no-shock case. At 30 and 50 ns (Figure 5.12(c) and (d) this lag becomes even more obvious indicating a reduction in plasma front propagation speed as discussed earlier. In addition, the tail of the charge density for the shock case is pushed further away from the dielectric surface passing the 50 μm indicator, whereas in the no-shock case the tail doesn't move that far away from the dielectric surface. This is related to the

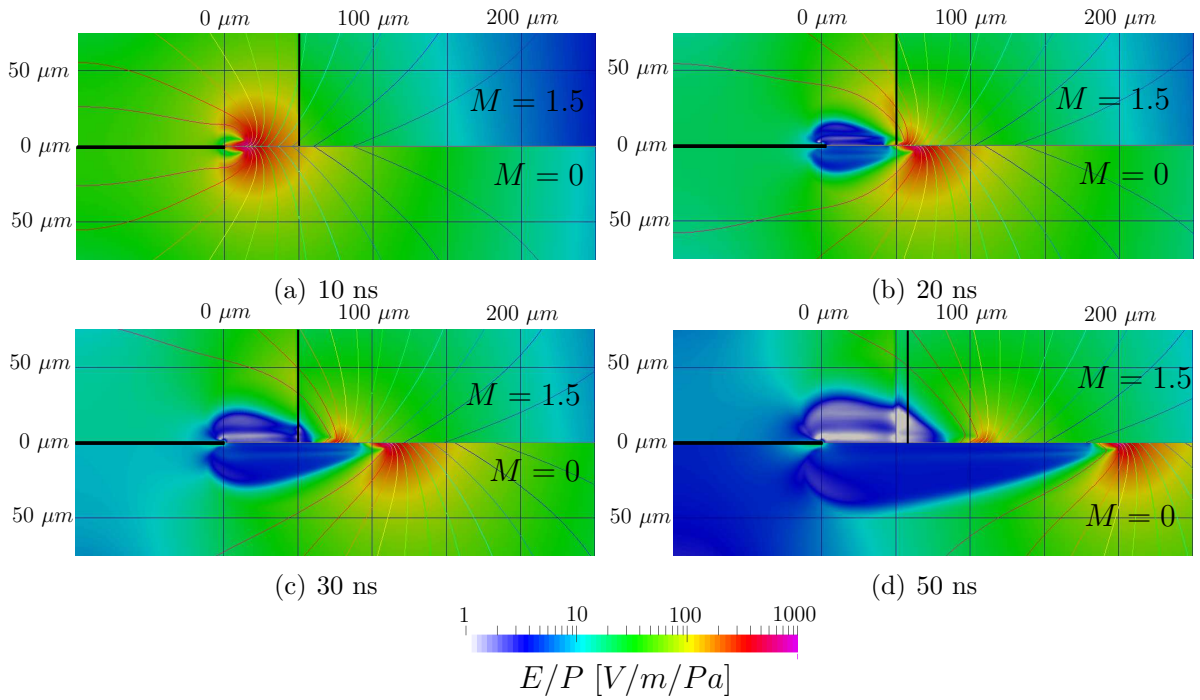

Figure 5.10: Electric field to pressure ratio distribution $[V/m/Pa]$ for shock case with Mach 1.5 compared against quiescent flow case. The contour lines are the electric field potential: 0 V for grounded electrode and 1200 V for the exposed electrode. The origin of horizontal axis is located at the edge of the exposed electrode ($0\mu m$).

absence of significant electron concentration above 25 μm and the ions being forced further away from dielectric surface.

Based on these results a shock located in a path of a plasma generated by SDBD PA is detrimental to plasma generation and propagation. In the case of a strong enough shock (e.g. normal shocks at Mach 2 and above) the plasma propagation is limited to the diffusion of positive ions created before the shock is reached (as opposed to the continuous generation of positive ions within a plasma sheath). The presence of a shock (independent of its strength) changes the E/P field such that a region of high concentration of positive ions is generated directly downstream of the shock further away from the dielectric when compared to a no-shock case. The cases presented in this section only consider frozen flow and do not incorporate the effects that a plasma has on the flow itself. The next section considers the case were the

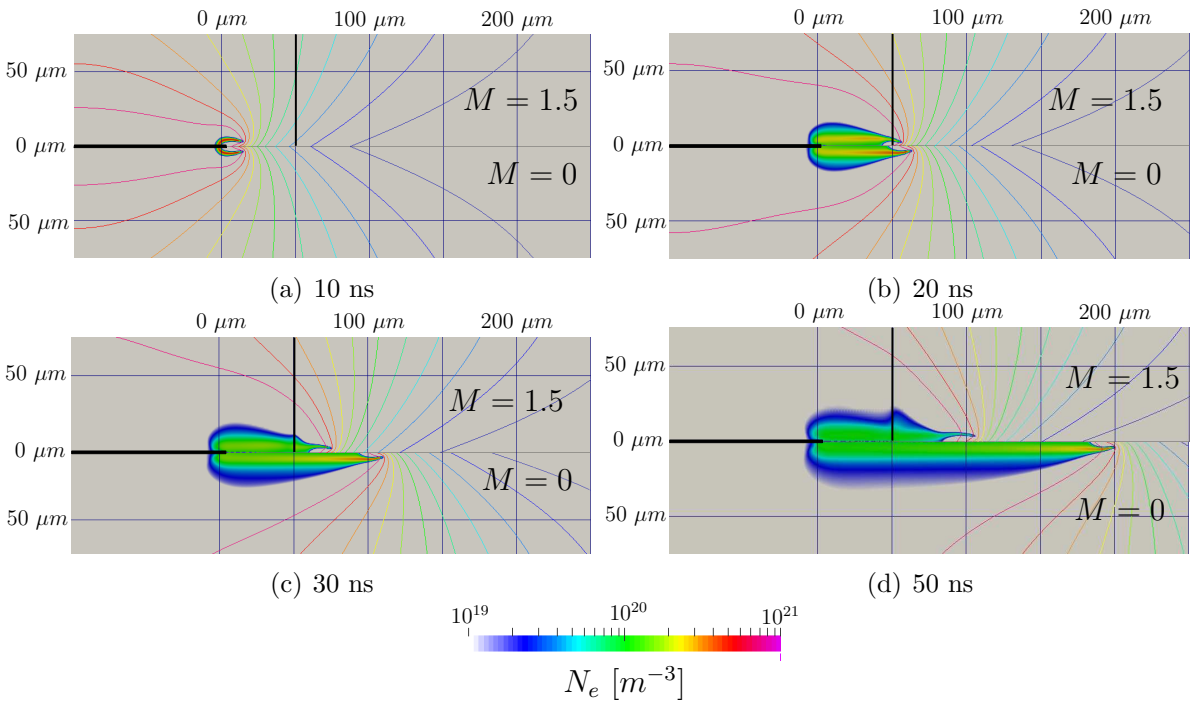

Figure 5.11: Evolution of electron density distribution $[m^{-3}]$ for shock case with Mach 1.5 compared against quiescent flow case. The contour lines are the electric field potential: 0 V for grounded electrode and 1200 V for the exposed electrode. The origin of horizontal axis is located at the edge of the exposed electrode $(0\mu m)$.

interactions between the flow and the plasma are modelled.

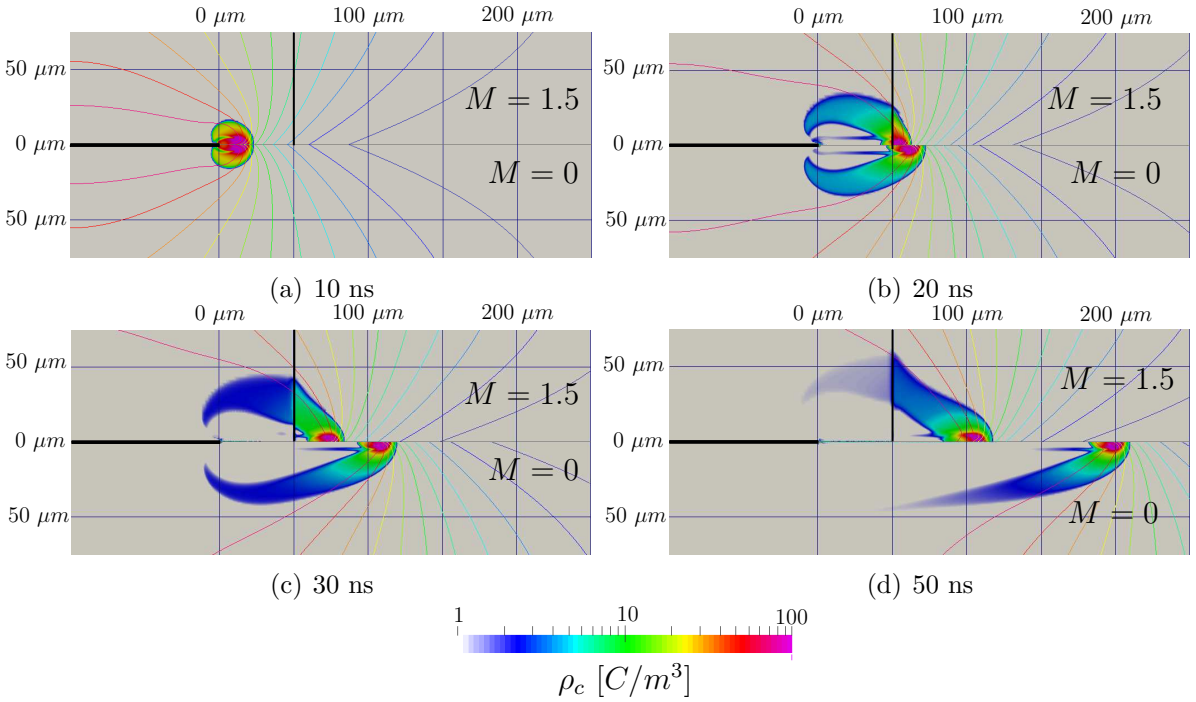

Figure 5.12: Evolution of charge density distribution $[C/m^3]$ for shock case with Mach 1.5 compared against quiescent flow case. The contour lines are the electric field potential: 0 V for grounded electrode and 1200 V for the exposed electrode. The origin of horizontal axis is located at the edge of the exposed electrode $(0\mu m)$.

Chapter 6

Coupling of background supersonic flow and plasma calculations

The previous chapter describes the results for a hypothetical supersonic flow situation with the fluid properties held constant. This chapter presents results where the plasma and supersonic flow interact with each other (i.e. the fluid properties are updated as the plasma evolves). An experiment described by Nishihara [3] serves as the basis for this analysis. Nishihara et al. [3] performed an experiment by placing a PA on a 12° wedge inside a supersonic wind tunnel as shown in Figure 6.1(a), 6.1(b). The experiment was performed in a wind tunnel that operates using dry air at plenum pressure of 0.5 - 1 atm. The conditions at the test section were measured at 38 torr (5.07 kPa) and 2.2-2.3 Mach. The plenum pressure was at 400 torr (53.3 kPa). The shock is generated by a 12°, 7 mm wedge with spanwise width of 3.2 cm (the channel width was 4 cm). The electrodes were 0.4 mm thick copper foil tape, 20 mm in length and 5 mm in width. The dielectric was made out of two layers of Kapton tape for a total dielectric thickness of 0.2 mm. The exact voltage profile for this experiment was not shown, however, the authors mentioned that the power supply operates in pulse mode at 1 kHz repetition rate, with maximum pulse peak of 20 kV and pulse duration of 50-100 ns. This corresponds to a maximum electric field strength within

the dielectric of 10^8 V/m. The maximum electric field strength in the air region is estimated to be $3.5 \cdot 10^8$ V/m by using Eq. 2.47 (Kapton has dielectric constant of 3.5 [80]). Based on the oblique shock equations the pressure downstream of the shock is 9.34 - 10.1 kPa. These values correspond to E/p values of 34.5 - 37.5 kV/m/Pa for the downstream region and 69 kV/m/Pa for the upstream region of the shock.

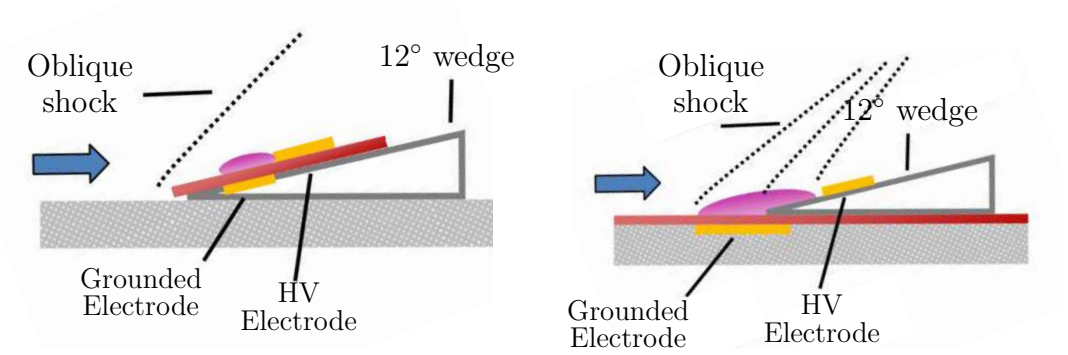

(a) Configuration A, the grounded electrode is 5 mm wide

(b) Configuration B, , the grounded electrode is 10 mm wide

Figure 6.1: One of the experimental configurations presented by Nishihara [3]. The length of the wedge is 7 mm in length. The grounded electrode is 0.4 mm thick copper foil, which is 5 or 10 mm wide. The exposed electrode is also 0.4 mm copper foil, which is 5 mm wide. The dielectric is a 2 layer Kapton tape with a combined thickness of 0.2 mm.

6.1 Wedge Flow: Geometry and Test Conditions

The simulated geometry is a 2D wedge at 12° (Figure 6.2). The domain size is 600 μm for the flat surface upstream of the wedge, 700 μm downstream of the wedge corner along the horizontal line, and 500 μm in vertical direction. The dielectric thickness is set to 50 μm. The mesh size is 392 652 elements and 795 004 nodes with the minimum element size of 0.5 μm. The applied voltage is a constant 1 200 V. The relative permittivity of the dielectric is set to 5. The ambient temperature is set to 300 K and the pressure is set to 100 kPa. The free-stream velocity is set to 694 m/s, which corresponds to 1.97 Mach for nitrogen gas. The fluid flow also requires

Parameter	Free-stream	After-shock
Mach Number	1.97	1.537
Static Pressure [kPa]	100	187.88
Static Temperature [K]	300	361.84
Speed [m/s]	694.87	595.40
E_{max} [V/m]	$1.2{\cdot}10^8$	$1.2{\cdot}10^8$
E/P_{max} [V/m/Pa]	1200	638.7
Wedge angle		12 °
Shock angle		42.23 °

Table 6.1: Properties of the fluid region ahead and after the oblique shock.

a boundary condition for velocity at the surface. There are two possibilities: free-slip and no-slip. Both of these cases are presented in the sections below. Table 6.1 provides with the theoretical flow properties for the supersonic flow across an oblique shock of 12° for Mach 1.97.

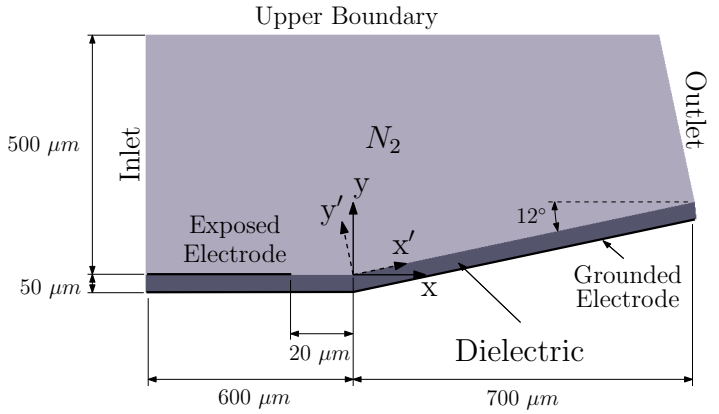

Figure 6.2: Computational domain for plasma-shock interaction simulation. The electrode edge is 20 μm upstream of the wedge. The grounded electrode is along the entirety of the dielecrtic bottom surface. The wedge is 0.7 mm long which is 10 times smaller than the experimatal setup by Nishihara (Figure 6.1).

The simulated conditions are reflective of Nishihara geometry, but adjusted to a scale feasible for the computational resources available. They are equivalent to

examining the highlighted region in Figure 6.1. However, due to numerical stability issues some of the flow conditions have been adjusted (e.g. free stream pressure in the simulation is set to 100 kPa, while in experimental work it is 5 kPa) and therefore only qualitative comparisons will be made for verification purposes.

6.2 Wedge Flow Results: Free Slip

To evaluate the effects of the interaction between a plasma and a gas flow without the complexity of a boundary layer the wedge geometry is simulated at Mach 1.97 with free-slip conditions. Figures 6.3 and 6.4 show the pressure and temperature conditions before the plasma actuator is activated. The pressure at the inlet is 100 kPa and downstream of the shock it is 187.7 kPa (the theoretically predicated value is 187.9 kPa). The temperature at the inlet is set to 300 K and downstream it reaches 361.7 K (the theoretically predicated value is 361.8 K). These results were obtained by using OpenFOAM and running the sonicFoam solver with the boundary conditions mentioned in the previous section until a steady state is reached (which is achieved at 200 μs). The exposed electrode is set to a constant 1 200 V for the remainder of the simulation. The simulation is advanced 200 ns of simulated time as this is enough to observe the effects of plasma-shock interaction.

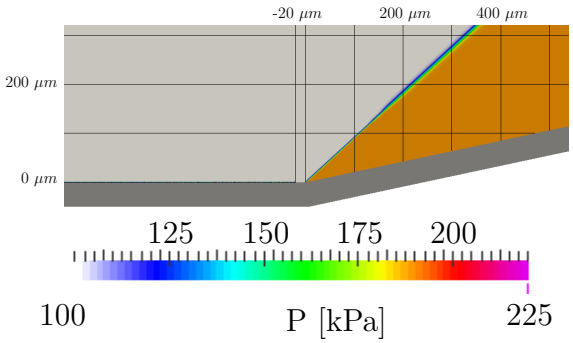

Figure 6.3: Initial pressure distribution.

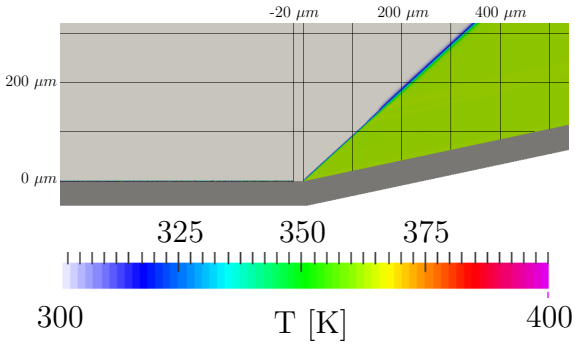

Figure 6.4: Initial temperature distribution.

Figures 6.5 and 6.6 show the plasma parameters such as ions and electron number density evolution. According to Figure 6.5 the plasma is being quenched by the presence of the shock, similar to the flat plate simulations with shock given the drop in maximum E/P to approximately 639 (V/m)/Pa, which is between 533 (V/m)/Pa and 976 (V/m)/Pa observed in Section 5.2 for Mach 2 and Mach 1.5, respectively. This causes a reduction in the effect that the plasma can have on the shock itself. At 30 ns Figure 6.5(b) shows that in the region just downstream of the shock and significantly above the dielectric there is a region of an increased positive ion concentration. This makes it appear as though the positive ion concentration rises across the shock as is also seen in the flat plate shock case at Mach 2 in Figure 5.4(c). Additionally in the normal shock case when the plasma passes through a shock at Mach 2 a void is created upstream of the shock (Figure 5.4(d)). In the case of the wedge shock shown here a void is seen at 200 ns only in this case it is located 50-100 μm behind the shock. This difference in location is due to the difference in the geometry of the electric field which influences where the positive ions can migrate. After the reduction of the ionization process (50 ns), the positive ion cloud continues to increase in size and decrease in concentration due to diffusion where at 100 ns and 200 ns the cloud propagates downstream bounded by the shock and the dielectric surface.

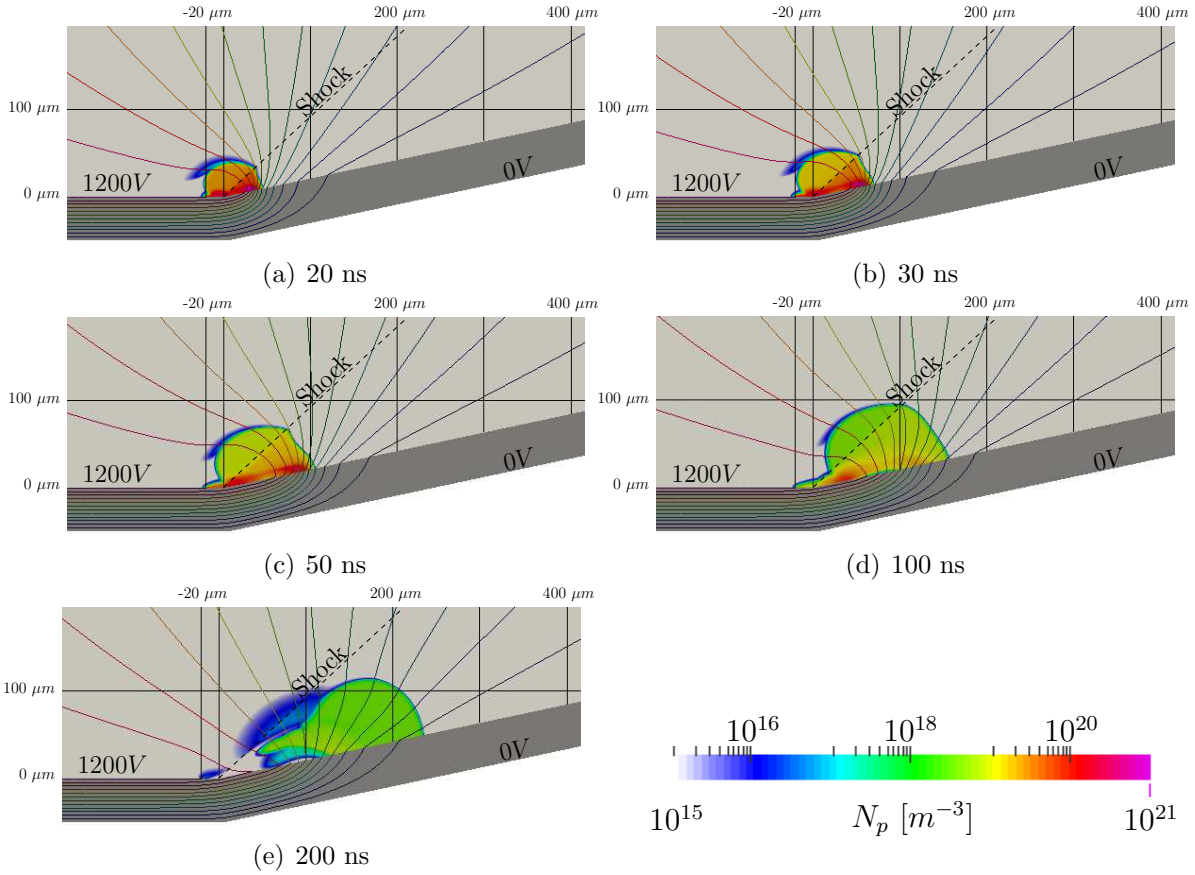

(a) 20 ns

(b) 30 ns

(c) 50 ns

(d) 100 ns

(e) 200 ns

Figure 6.5: Positive ion concentration (N_p) $[m^{-3}]$.

Up to 50 ns the electrons behave similarly to the case without a shock, with a high concentration of electrons within the plasma near the dielectric surface with a lip (similar to Figure 3.8(b)) within the sheath region (Figure 6.6(a) and (b)). However, at 50 ns the concentration of electrons is visibly reduced indicating a reduction in the intensity of ionization processes (Figure 6.6(c)). By 200 ns the electron concentration drops below $10^{16}\ m^{-3}$. This indicates that the positive ions present at 200 ns (Figure 6.5(e)) are those that are created before the plasma sheath is extinguished at 50 ns.

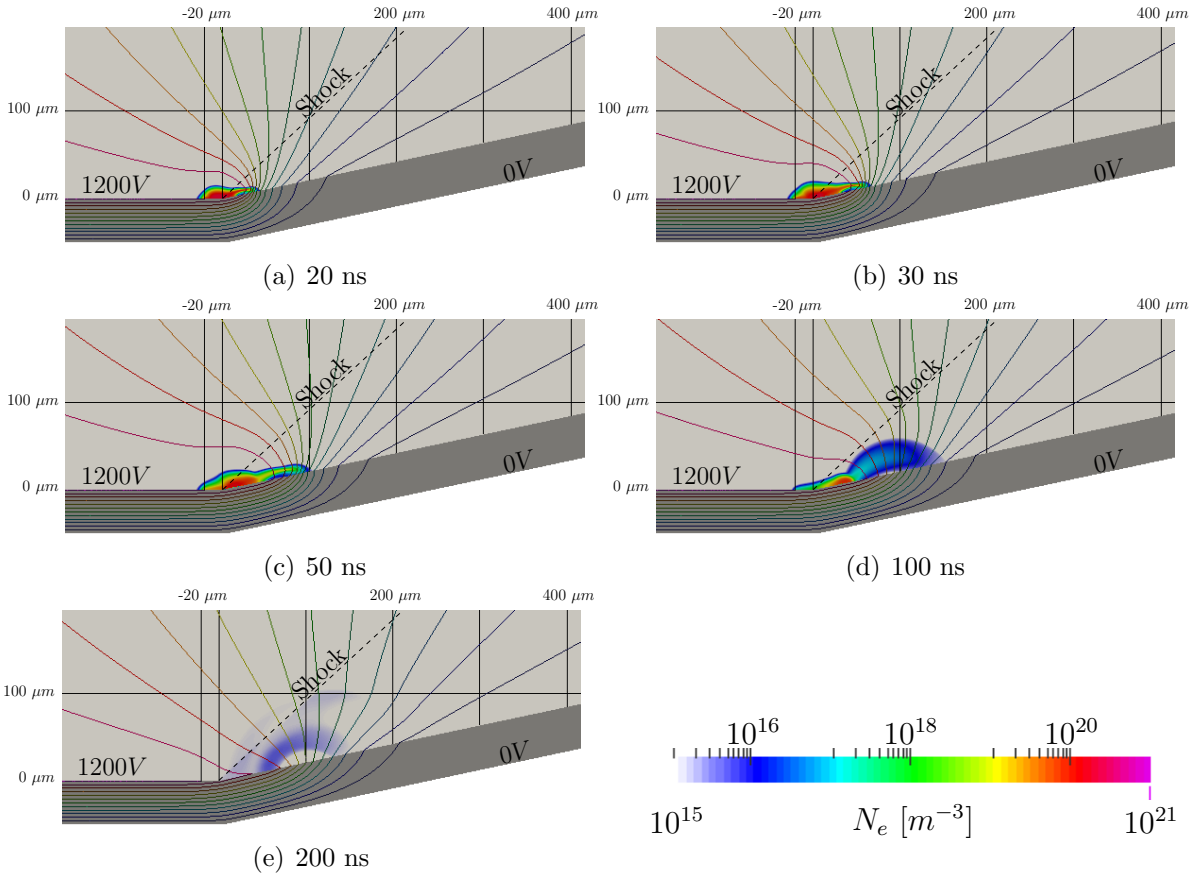

Figure 6.6: Electron concentration (N_e) $[m^{-3}]$.

While enough plasma exists to carry current, this current flowing through the plasma results in Joule heating of the surrounding gas. Due to Joule heating the temperature rise near the surface is as high as 55 K initially (Figure 6.7(a)), but cools down within 200 ns to a maximum of 45 K with most of the region being within

35 K of the initial value (Figure 6.7(e)). Due to the sudden increase in temperature a pressure wave is formed. This causes an additional temperature rise of 5 K at the pressure wave itself which is followed by as much as a 10 K decrease in temperature within the expansion wave that follows (both waves are discussed below).

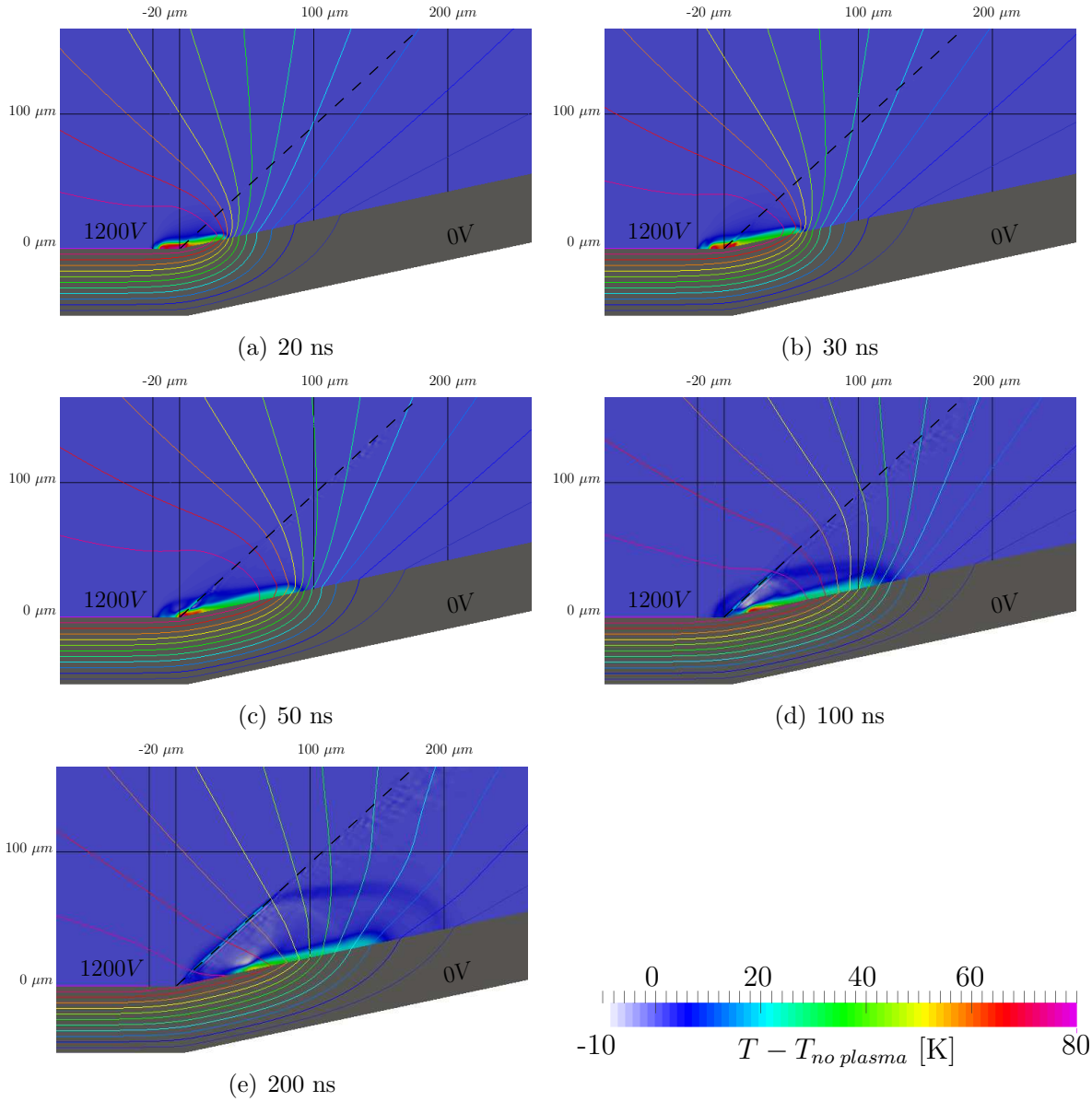

(a) 20 ns

(b) 30 ns

(c) 50 ns

(d) 100 ns

(e) 200 ns

Figure 6.7: Temperature change [K]. Free-stream temperature is at 300 K.

Figure 6.8 shows the initial and final pressure distribution for the free-slip case. At 200 ns of SDBD PA operation a weak pressure wave is visible downstream of the shock. For better visualization the difference in the flow properties (pressure, temperature and velocity) is calculated against a simulation of the flow without a plasma. Figure 6.9 shows this difference for the pressure. This figure clearly shows the effect that

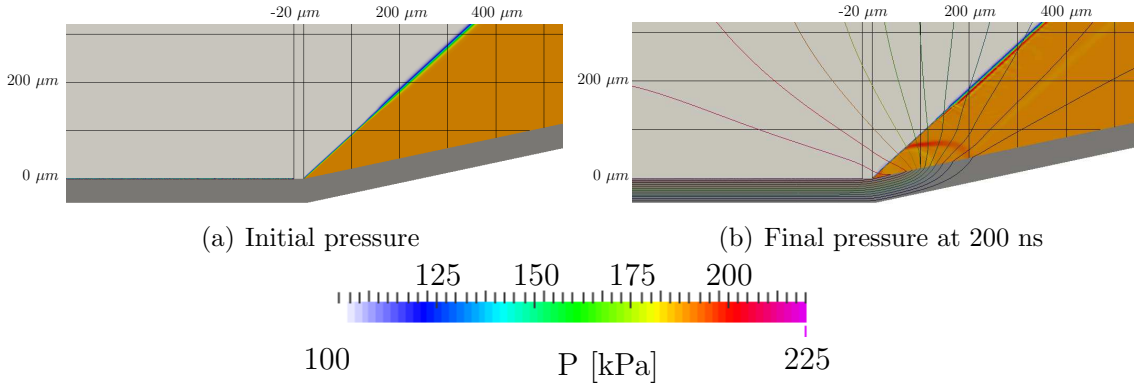

(a) Initial pressure (b) Final pressure at 200 ns

Figure 6.8: Initial pressure and pressure at 200 ns.

the plasma actuator has on the flow. At 20 ns a pressure region with an increase of 25 kPa is formed which continues to propagate downstream of the electrode as well as away from the surface. The pressure wave originates at the location of initial plasma formation, that is at the trailing edge of the exposed electrode. It is relatively weak compared to the strength of the shock (25 kPa vs 88 kPa pressure rise across the shock). While during the first 100 ns there is a region with elevated pressure (compared to the free-stream), this pressure region dissipates by 200 ns with little to no movement of the shock itself. Downstream of the shock the positive pressure wave originating from the actuator continues to propagate along the shock wave and the dielectric surface, though the strength of this pressure wave decreases to a maximum ΔP of 10.5 kPa at 200 ns. This pressure wave is followed by a low pressure region with a maximum pressure reduction of 4 kPa with most of the region being at 1 kPa below the initial value.

Figure 6.10 shows the changes in the velocity due to the operation of the PA in

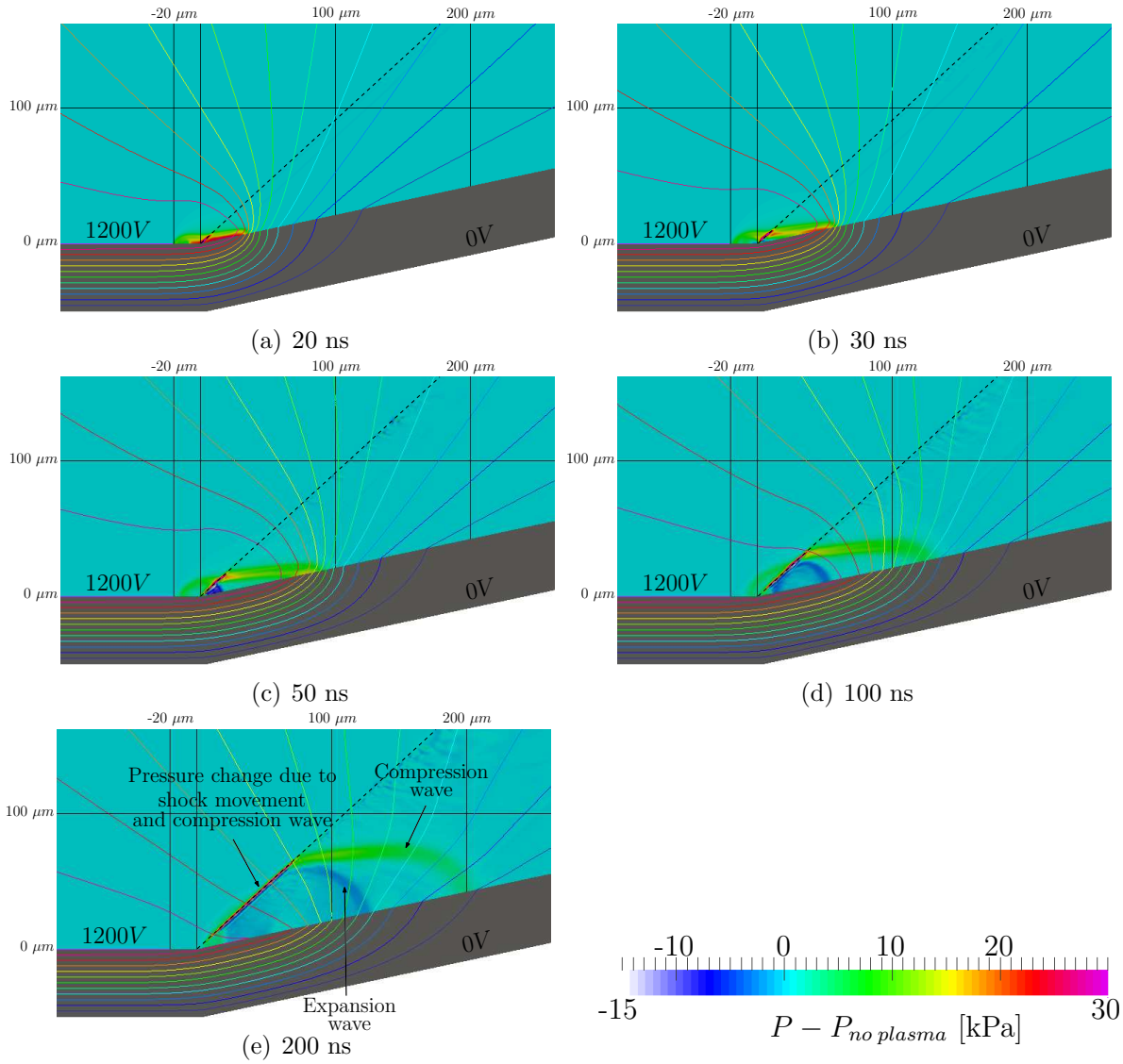

Figure 6.9: Pressure change [kPa]. Free-stream pressure is at 100 kPa.

terms of magnitude and direction. The maximum velocity change does not exceed 23 m/s (less than 5 %) within the first 30 ns (Figure 6.10(a,b)) and the change drops to below 15 m/s for the pressure wave front. Near the surface this change is even smaller (below 8 m/s). Figure 6.10 also shows the change in velocity towards the upstream direction indicating a reduction in the speed of the gas flow in those regions. These regions are mainly concentrated close to the surface of the dielectric as shown in Figures 6.10(a-d). In addition, the large magnitude change along the shock indicates

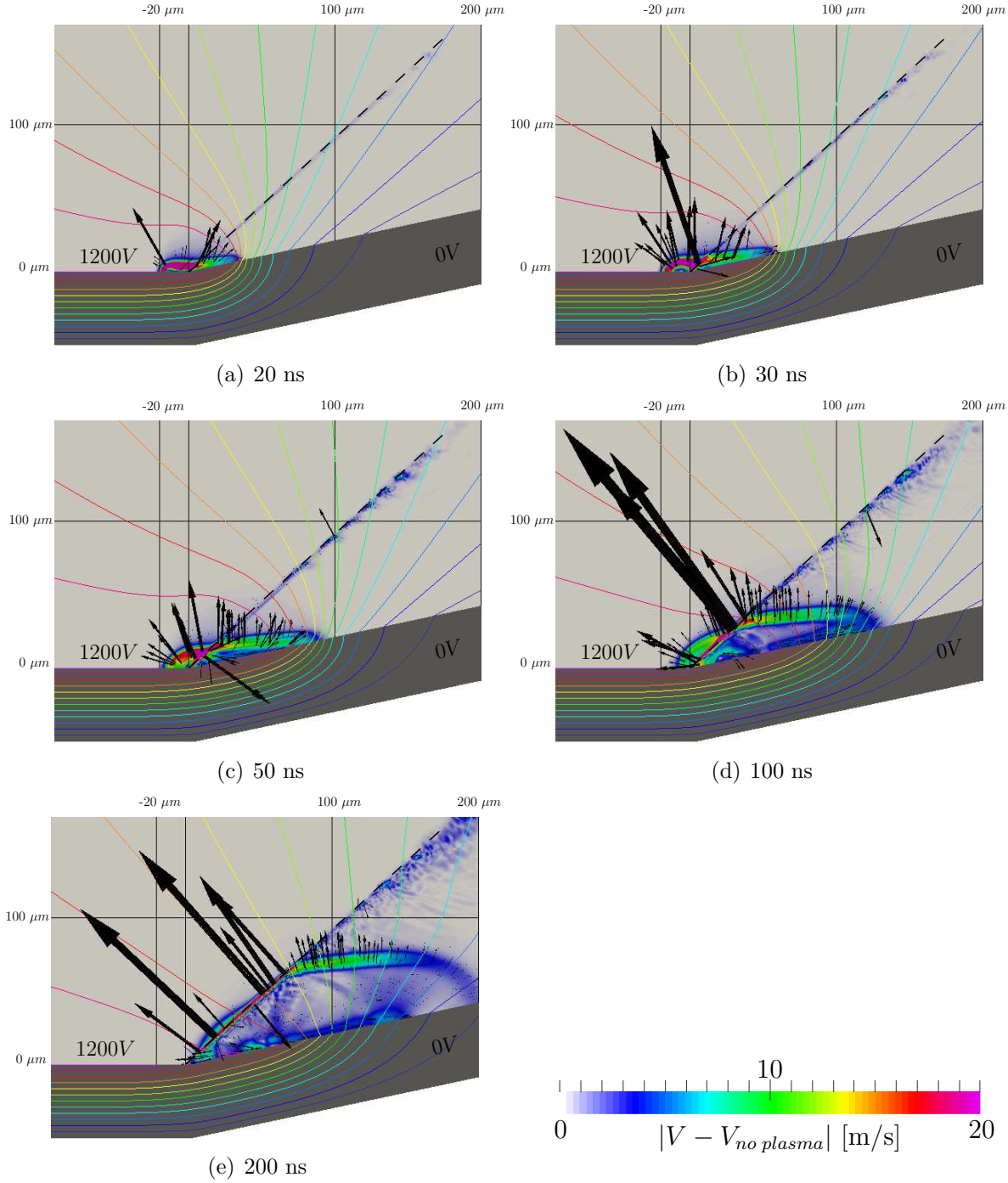

Figure 6.10: Velocity change from no-plasma conditions [m/s] ($\Delta\mathbf{V} = \mathbf{V} - \mathbf{V}_{no\ plasma}$). Free-stream speed is at 694 m/s, which corresponds to Mach 2.

some fluctuations in the position of the shock although this motion doesn't exceed 5 μm.

In the idealized case (no boundary layer) of a wedge shock the plasma is shown as being quenched by the shock at these conditions with very little effect on the shock itself. The effect of the plasma is mainly concentrated downstream of the shock in the form of a weak pressure wave (with a maximum pressure rise of 15 kPa) travelling along the downstream side of the shock and along the dielectric surface. This is similar to what Nishihara presents in his work, though at a different size and time scale (Figure 6.11).

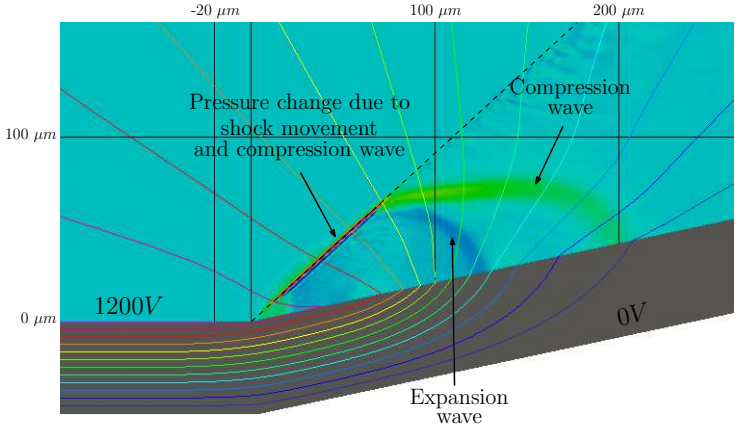

(a) Simulation, Pressure change at 200 ns

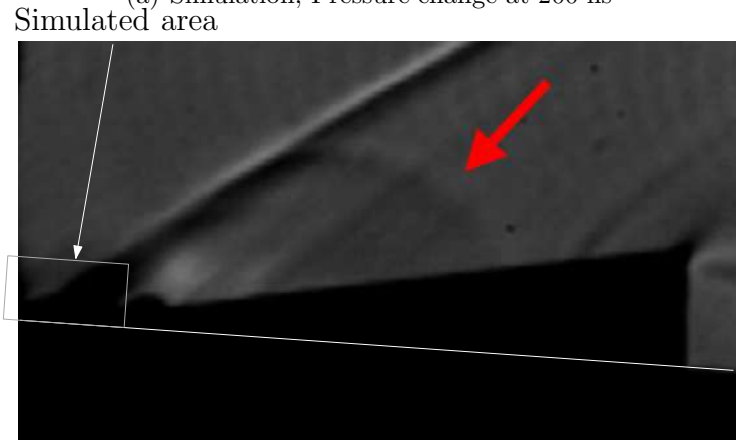

(b) Experimental results at 10 μs, Configuration A

Figure 6.11: Comparison of simulated and experimental [3] pressure waves.

6.3 Wedge Flow Results: No-Slip with Boundary Layer

Unlike the ideal shock case, a flow with a boundary layer has subsonic flow near the surface. To simulate this condition the inlet of the domain is modified to have a velocity profile which corresponds to the von Karman laminar flow approximation [81] described by Eq. 6.1:

$$V[m/s] = \begin{cases} 694.4 & if \quad y > 15 \cdot 10^{-6} m \\ 694.4 \left(\frac{2y}{15 \cdot 10^{-6}} - \left(\frac{y}{15 \cdot 10^{-6}} \right)^2 \right) & otherwise \end{cases} \tag{6.1}$$

where y is the vertical distance from the electrode surface.

The profile from Eq. 6.1 is shown in Figure 6.12.

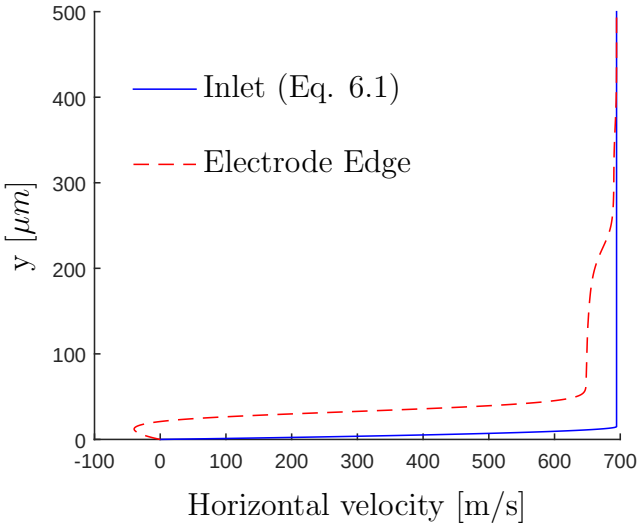

Figure 6.12: Initial horizontal velocity profile at the inlet and the separation buble at the electrode edge.

The result of this boundary layer is a velocity flow field with a flow recirculation at the wedge as shown in Figure 6.13. The recirculation is also visible from the velocity profile in Figure 6.12 at the exposed electrode edge location. Due to this recirculation

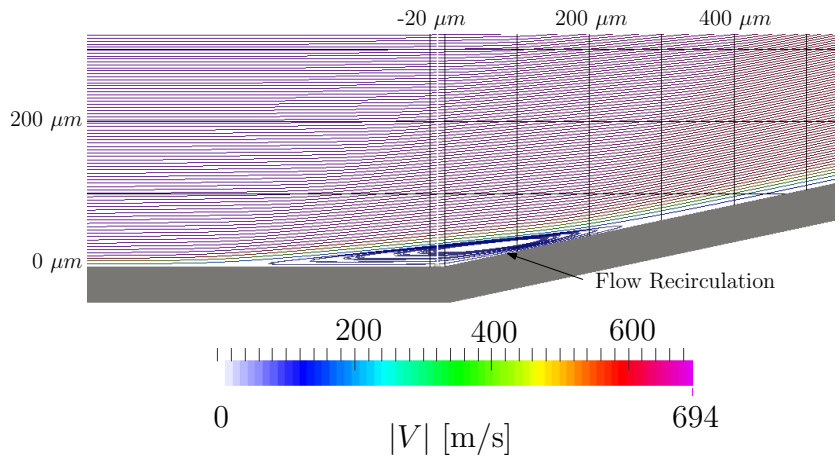

Figure 6.13: Initial Speed [m/s]. Free-stream speed is at 694 m/s, which corresponds to Mach 1.97.

the previously single shock is separated into two weaker and less pronounced shocks which can be seen in Figures 6.14 and 6.15. Figure 6.15 compares the pressures

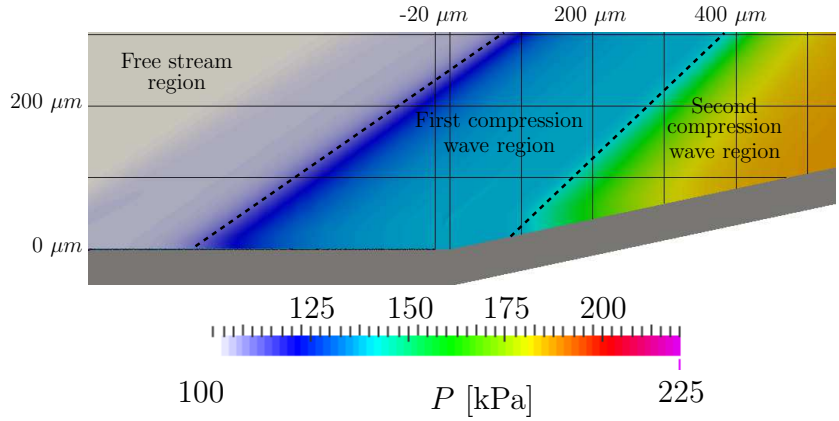

Figure 6.14: Initial Pressure [Pa]. Free-stream pressure is at 100 kPa.

along the dielectric surface between free-slip and no-slip cases. In the free-slip case the shock is clearly visible at the wedge location (x = 0 μm) by a sharp increase in the pressure. In the case of the no-slip simulation with boundary layer the pressure rise happens in a much smoother manner: it starts upstream of the wedge (x = -400 μm) and reaches values similar to free-slip case further downstream (x = 600 μm). This pressure profile can be represented by two distinguishable compression regions: the first one ending at 100 μm downstream of the corner location and a second one

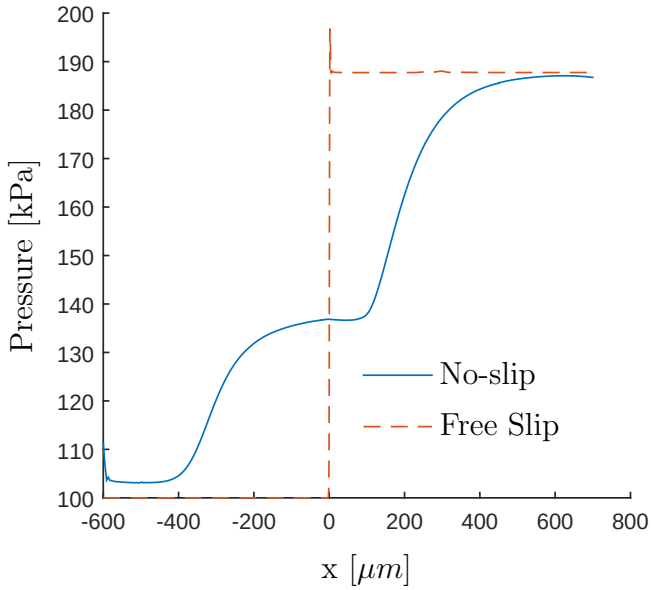

Figure 6.15: Pressure along the exposed electrode and dielectric interface.

starting at this location and continuing to x = 600 μm.

While the boundary layer is not visible in the pressure figure, the upper edge of the boundary is clearly visible in the temperature profile. The inlet for the temperature is set to a constant 300 K, while the gas-dielectric interface is set to have no heat flux (insulation). The initial thickness of the boundary layer was set to 15 μm through velocity profile, but at the flow recirculation region the boundary layer thickens to as much as 50 μm in the vicinity of the edge of the exposed electrode (x = -20 μm). This means that, at least initially, the plasma is fully inside the boundary layer.

Unlike the previous case with an idealized shock, here the plasma is located mostly inside the boundary layer region which doesn't have any sharp pressure gradients. The absence of a significant sudden pressure change means that the plasma doesn't exhibit a sudden weakening as it progresses along the dielectric surface, which can be seen from Figures 6.17 and 6.18. That means there is no plasma extinction due to the presence of the boundary layer. Figure 6.17 shows the positive ion concentration for 50, 100 and 140 ns. This distribution behaves similarly to the no-shock flat plate

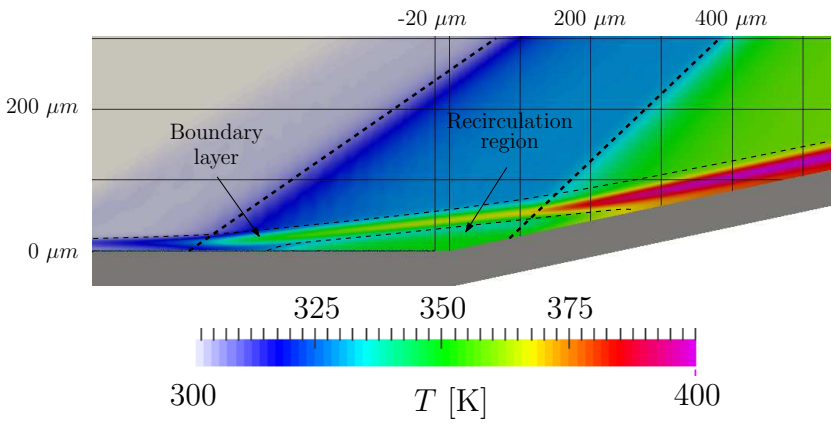

Figure 6.16: Initial Temperature [K] . Free-stream temperature is at 300 K. The figure shows only a portion of the computational domain.

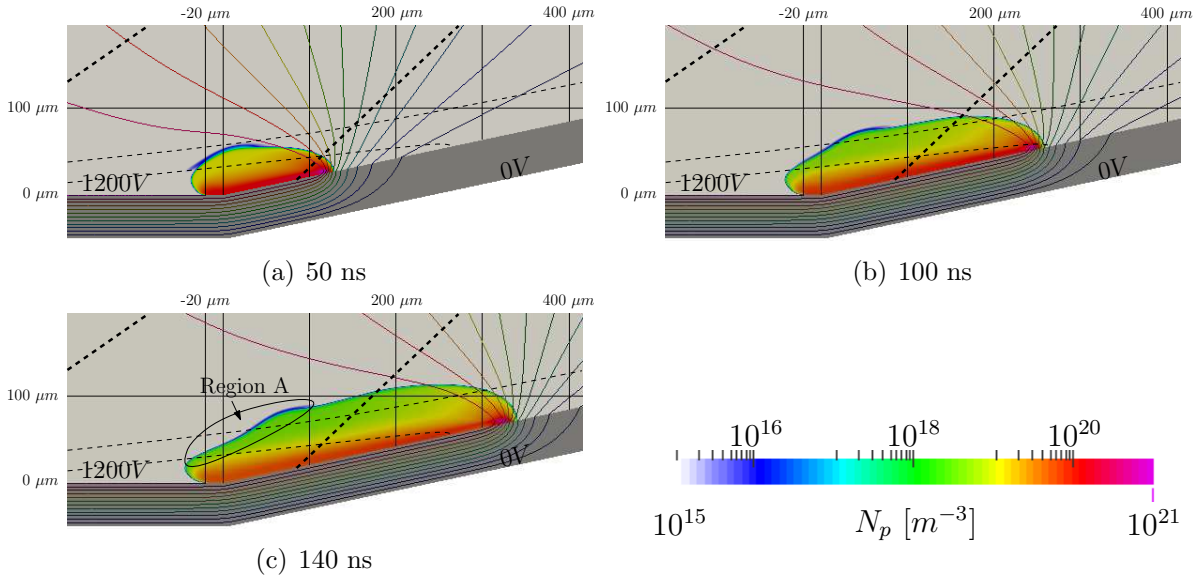

Figure 6.17: Positive Ions concentration $[m^{-3}]$.

case, though the plasma propagation is slower due to a higher pressure within the plasma region and a lower value of the dielectric permittivity (5 here vs 10 in the flat plate case). The higher pressure results in a lower value of E/P where the ionization is a function of this value as was discussed in Section 5.2. The higher value of the dielectric permittivity results in a stronger electric field in the gas region due to the continuity of electric displacement field as mentioned in Section 2.2.1. Due to the combination of these two factors, in the case of the wedge shock with a boundary

layer the plasma covers 140 μm from the electrode edge after 50 ns, while in the flat plate case at 100 kPa the sheath is at 200 μm mark by that time (Figure 3.5).

The positive ion distribution in the case of a flow with a boundary layer also shows an extra feature that is not present in the free-slip and no-flow cases. This feature appears as a bump in the profile (or more accurately an absence of ions just outside the recirculation zone) and is indicated as Region A in Figure 6.17(c). The electric field in Region A is very weak, therefore the ions are easily carried with the bulk flow (this is also true for electrons). Since the bulk flow is faster outside the boundary layer, the ions in the region are also moving faster the further they are from the walls, hence the appearance of a "bump".

The concentration of electrons (Figure 6.18) also indicates a continuous ionization process even at 140 ns with a maximum concentration on the order of 10^{20} m^{-3} at that point. The shape of the electrons cloud is similar to that of the positive ions (with the exception of the sheath region).

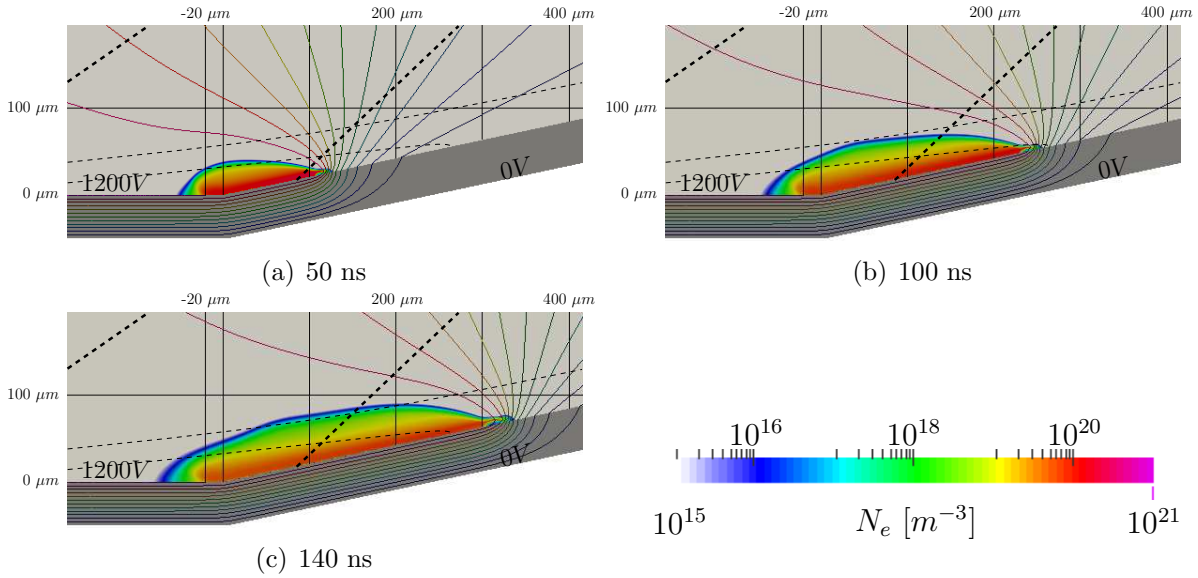

Figure 6.18: Electrons concentration $[m^{-3}]$.

While the effect of the flow on plasma development in the presence of the boundary layer is not as noticeable as in the case without the boundary layer, the effect

that the plasma has on the flow is stronger. The difference in flow properties (pressure, temperature and velocity) is calculated against a simulation of the flow without plasma in Figures 6.19 - 6.21.

Figure 6.19 shows the temperature change rise due to the operation of plasma actuator. After the initial current spike the gas temperature within the plasma rises by more than 100 K at the edge of the electrode (Figure 6.19(a)). As the plasma front propagates along the dielectric, the temperature rise within the neutral plasma region varies from 10 K to 40 K right at the surface of the dielectric. The maximum temperature rise occurs at the edge of the exposed electrode and initially exceeds 100 K, though by 140 ns this value drops to 55 K. In addition to the temperature rise at the surface of the dielectric, Figure 6.19 shows a wave of temperature rise of 10 K propagating away from the dielectric surface. This is the pressure wave which occurs due to the sudden heating generated from the operation of the plasma actuator. The pressure wave is shown in more detail in Figure 6.20. Similar to the free-slip case (Section 6.2) the change in temperature can be attributed to Joule heating as already mentioned, and a temperature rise due to the passage of the pressure wave that is generated due to the sudden temperature rise in the sheath region. The change in temperature due to the pressure wave doesn't exceed 10 K.

Due to continuous generation of plasma, the pressure wave is continuously generated within the sheath region up to the point of termination of the plasma computations (140 ns, Figure 6.20(c)). While the value of the pressure change is similar to the free-slip case (here $\Delta P \approx 13\ kPa$, while for free-slip it is approximately 15 kPa), the extent of the pressure wave propagation is significantly larger. Similar to the free-slip case the region bound by the pressure wave also has an expansion wave that originates at the edge of the exposed electrode, but it doesn't follow the shape of the compression wave. Instead, the expansion wave propagates away from the exposed electrode edge while maintaining a circular shape.

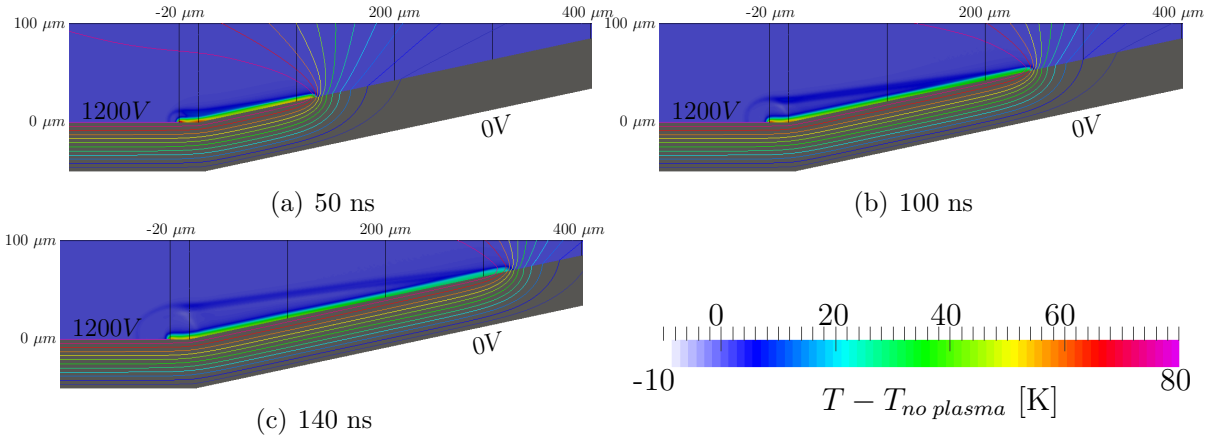

Figure 6.19: Temperature change [K] due to operation of plasma actuator. Free-stream temperature is at 300 K. The temperature difference is calculated against the simulation of the flow without plasma.

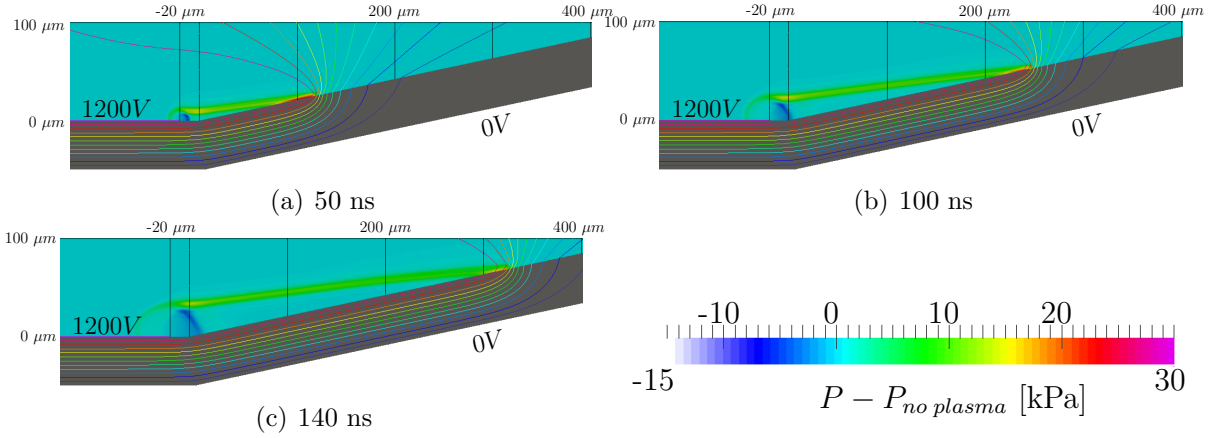

Figure 6.20: Pressure change [Pa]. Free-stream pressure is at 100 kPa.

Figure 6.21 shows the change in velocity field. The maximum change happens at the location directly above the edge of the electrode. The location of this maximum velocity change drifts upward with the pressure wave and drops to 21 m/s by 140 ns, while for the most part of the velocity change is below 15 m/s. The shape of the velocity change is similar to that of the pressure wave.

Figure 6.22 compares the pressure and temperature changes along the dielectric surface for no-slip (boundary layer) and free-slip cases at 100 ns. The pressure graph

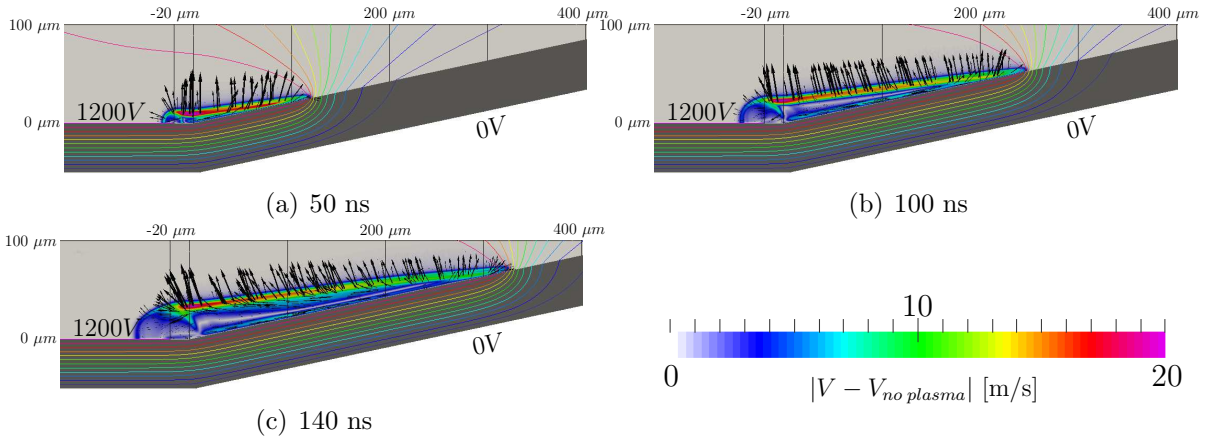

Figure 6.21: Velocity difference from the initial conditions [m/s]. Free-stream velocity is at 694 m/s, which corresponds to Mach 1.97.

indicates that the no-slip case generates a significantly stronger pressure wave at 100 ns. This is expected since in the case of free-slip (no boundary layer) the plasma is already quenched at that point and starts to diffuse, while in the case of no-slip the plasma continues to propagate. The temperature change graph indicates that the maximum temperature change is comparable between the two cases. However, since the plasma propagates further in the case of the flow with the boundary layer (no-slip) a larger portion of the flow is heated in that case.

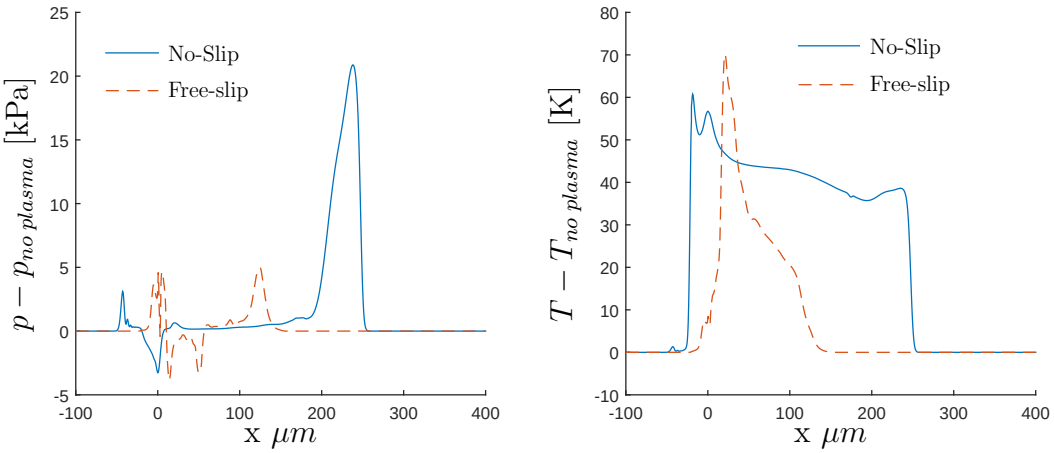

Figure 6.22: Comparison between no-slip and free-slip cases at 100 ns.

Figure 6.23 shows the change in the velocity profiles normal to the surface due to the operation of a PA. The graphs show the difference in ΔV between the no-slip and free-slip conditions at three locations within the simulation (-20 μm, 0 μm, and 100 μm, the 0 μm location is at the beginning of the wedge, and the profile is normal to the plane of the exposed electrode). According to the profile at the edge of the exposed electrode (-20 μm), 100 ns after the start of the simulations there are no noticeable effects on the velocity along the surface for the free-slip condition. In the case of the no-slip conditions a PA seems to generate a flow that counters the separation bubble: close to the surface the flow is accelerated forwards and towards the surface (positive ΔV_x and negative ΔV_y), while further away from the surface the flow is accelerated backward and away from the surface (negative ΔV_x and positive ΔV_y). This is also the case for the no-slip flow at the wedge corner (0 μm). The vertical speed change (ΔV_y) at this location is twice that of the electrode edge (20 m/s vs 10 m/s), while the horizontal velocity is of similar magnitude (2 m/s). Further downstream (100 μm in x-direction from the wedge corner, Figure 6.23(c)) flow is accelerated by an extra 10–15 m/s both in the forward (positive ΔV_x) and away from the surface (positive ΔV_y) directions. This accelerated portion of the flow is moved further away from the surface by 140 ns, which also matches the position of the pressure wave (Figure 6.20). In the case of the free-slip simulation, the velocity change is somewhat similar to the no-slip case, but it is located closer to the surface at the wedge corner location and further away from the surface at the 100 μm location.

The velocity-change profiles further show that PA is more effective at flow actuation for no-slip case, since PA operates at lower pressures.

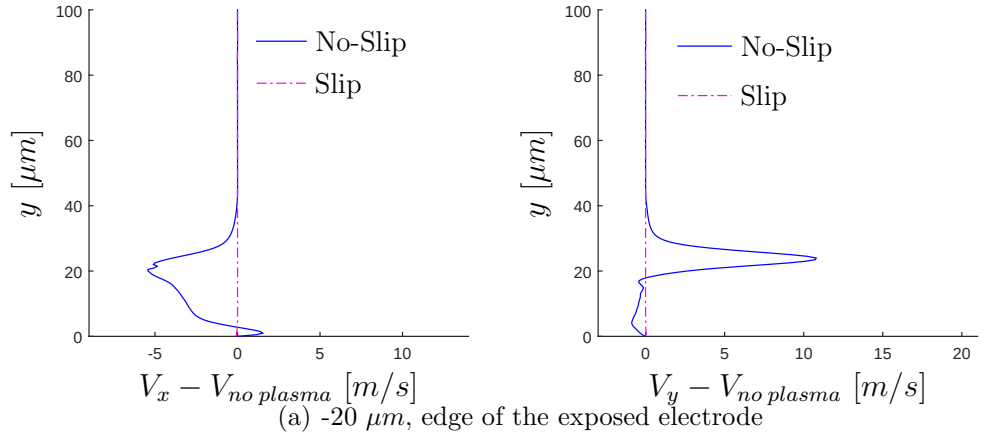

(a) -20 μm, edge of the exposed electrode

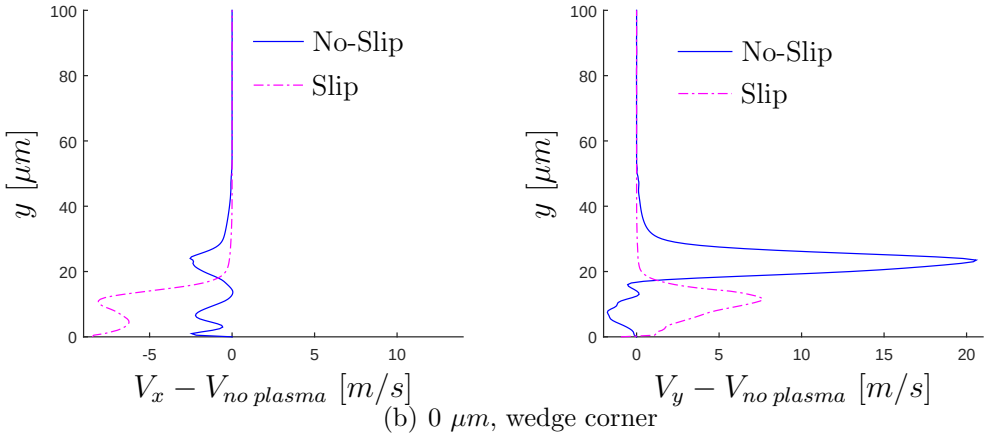

(b) 0 μm, wedge corner

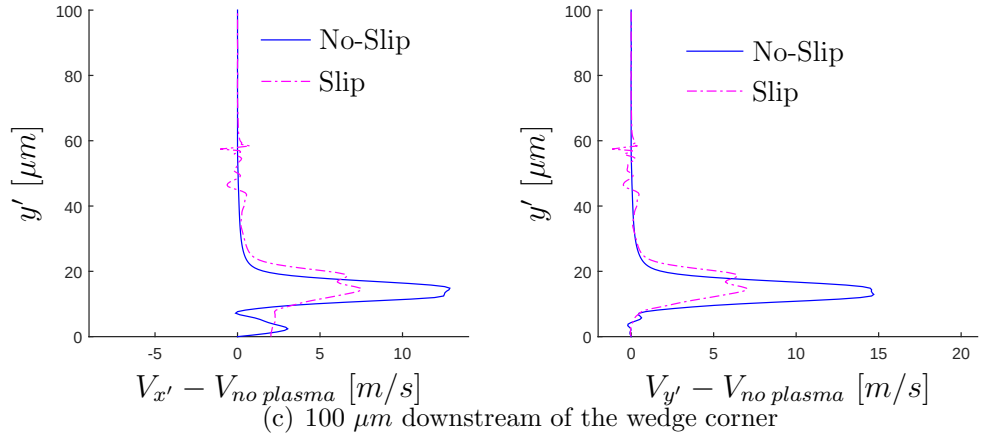

(c) 100 μm downstream of the wedge corner

Figure 6.23: Horizontal (V_x) and vertical (V_y) velocity differences along three different vertical lines at 100 ns. Normal direction y (and y') is measured from the dielectric surface.

Figure 6.24 shows the side-by-side comparison of the simulated PA in supersonic flow with a boundary layer and Configuration B of the Nishihara's experiment. What can be observed is that the "Geometry B" from Nishihara generates a series of shocks ahead of the wedge due to the physical presence of the exposed electrodes. In addition, the pressure wave generated by the PA has a prolonged structure similar to the simulation results for the case with a boundary layer. However, the time scale is noticeably different between the simulations and the experimental data, therefore this comparison should be taken with caution.

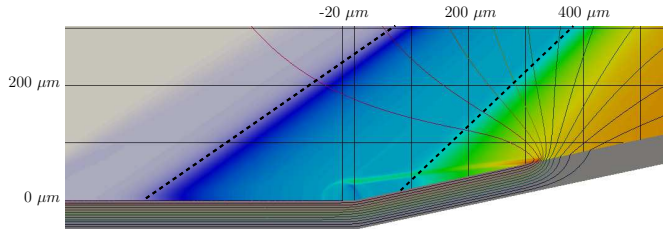

(a) Simulation: Boundary layer, final pressure at 140 ns

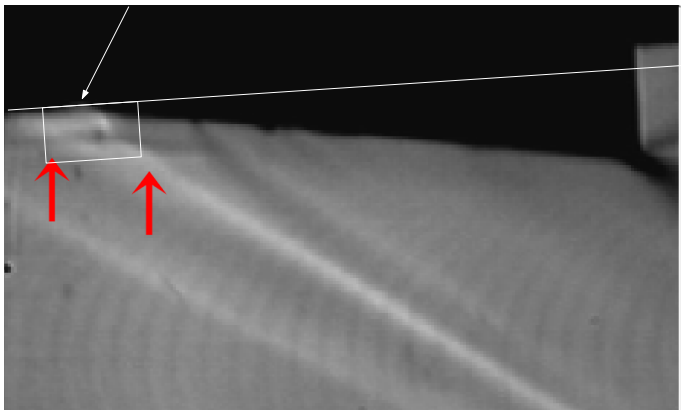

(b) Experimental results at 10 μs, Configuration B

Figure 6.24: Comparison of simulated and experimental [3] pressure waves.

Overall, these simulations indicate that for the tested PA configuration the effects on the supersonic flow are relatively small. The simulations also indicate that in order to maximize the performance of a PA the activation region (the edge of the exposed electrode) should be located upstream of a shock, otherwise a stronger electric field is required to activate the PA. Possible configurations that could have a stronger effect

on the shock geometry/location might include a different position of the PA (further ahead of the shock or recirculation region) and/or have a higher voltage applied to the PA.

Chapter 7

Conclusions

As mentioned in Section 1.5 the main aim of this work is to develop a compressible CFD solver with plasma computation capabilities which would allow to analyse the possible effects that a supersonic shock has on SDBD PA performance and vice versa. The solver is tested at quiescent flow conditions with the background flow properties frozen, while varying different parameters relevant to plasma formation at constant applied voltage to help develop an understanding of the plasma characteristics. Simulations are then performed for a sine-wave applied voltage with multiple cycles followed by plasma simulations containing a constant background flow for different shock configurations. Finally, the simulations are performed for a full plasma-supersonic flow interaction.

The plasma solver is initially tested under various conditions with no flow and verified against similar simulation results available in the literature. These comparisons demonstrate that the current code generated a higher initial current spike for identical condition, though the currents after the initial spike were comparable. This could be due to slight differences in some of the parameters used by different authors.

Simulations are also performed to study the effect of different plasma parameters on the development of a plasma. Results show that a higher initial concentration of charged particles reduces the time needed to reach peak currents as it takes less time

to saturate the plasma with charged particles.

Results also show that different voltage wave forms of the same magnitude have different times to peak current. The difference in the strength of the electric field for various wave-forms results in a difference in the initial ionization rate, where the slower the maximum voltage is reached the longer it takes to reach the maximum currents.

The effects of the thickness of the electrodes is also simulated where for a flush exposed electrode the initial ionization was slower as the thickness is increased. However, after the initial delay the currents for different electrode thickness showed nearly identical behaviour. The thicker the flushed electrode, the more reduces the initial electric field strength at the edge of the electrode in the gas region is reduced, thereby reducing the maximum possible initial ionization rate. However, as the plasma propagates away from the exposed flush electrode the thickness of the electrode becomes less relevant, hence the asymptotic behaviour of the currents.

In the case of an extruded electrode currents were found to be lower for thicker electrodes. With an extruded electrode electrons tend to gather near the top side the electrode, while the maximum electric field occurs at the interface between the dielectric, gas and electrode. The difference between these two locations result in lower ionization rates and therefore lower currents. As the plasma propagates further downstream the currents for thicker electrodes remain lower than for the case of a 0-thickness electrode.

Though most of the simulations for this work are performed with a constant applied voltage, the case of a sine wave applied voltage with four full periods is also analysed. From this analysis it is found that the first two periods are significantly different from subsequent periods. The difference appears in the shape of the currents that are generated by the PA as well as the shape of the plasma field itself. The initial current spike of a sine-wave is comparable in magnitude to a constant applied

voltage case (20 A/m). However, during the second period this spike is four times that (90 A/m). For the last two periods the maximum current value is reduced to approximately two times the constant voltage case (40 A/m), while the plasma region exceeds approximately 800-900 μm downstream (which doesn't change significantly between the last two periods). This indicates a strong need for the simulation of multiple cycles when using a cyclic applied voltage in cases where charged particles don't have enough time to dissipate within one period. This analyses also shows the complexity associated with defining a steady solution for cases of fluctuating applied voltages.

In addition to the development and testing of a solver for plasma flow computations, another aim was of this work is to answer two questions. The first question is " What effects does a supersonic shock have on a plasma generated by SDBD PA?" The presence of a shock is shown to result in a reduction in the plasma propagation where this effect becomes stronger with an increase in shock strength. This indicates that in cases where a PA operates across a shock one needs to consider the difference in operating pressures. As the plasma front passes through the shock into the region of higher pressure, the ions are pushed along the shock away from the dielectric surface by the electric field. In addition, these simulations show that even in cases where the ionization process had been reduced/eliminated by the shock there is still a relatively high concentration of the residual positive ions. This concentration is comparable to the cases where no shock is present, though it diffuses along the shock under the effect of the electric field. From these observations one may conclude that to maximize the performance of a PA it should be located ahead of a shock wave, otherwise a higher operational voltage might be required.

The second question this work seeks to answer is "What effect does a SDBD PA have on supersonic shock?" While the effect of a shock on plasma development in SDBD PA is significant for strong shocks, for the simulated oblique shock conditions

the SDBD PA had little effect on the shock geometry when compared to the overall flow field. In the idealized case of a wedge shock with a free-slip wall condition (no boundary layer), the shock reduced the ionization process consistent with what was observed in the simulations when the plasma calculations are decoupled from the bulk flow. However, even in this case where the ionization is extinguished the heating from the PA left behind a pressure wave with a pressure rise of approximately 11 - 25 kPa.

In a more realistic case of a wedge shock with a boundary layer, the SDBD PA operation occurs within the subsonic region of the flow separation bubble. Since the shock strength is reduced as compared to the free-slip case the plasma sheath propagates without any obstruction. As the plasma propagates along the surface of the dielectric a pressure wave is continuously generated within the sheath region with a pressure rise of approximately 13 kPa. A stronger voltage and/or different PA located further ahead of the separation bubble might have stronger effects on the flow and the shock wave geometry.

Chapter 8

Recommendations and Future Work

Before proceeding with additional simulations it is advisable to create a powerful and versatile solver. The current solver can be improved by including methods to speed up the computations, to provide better computational stability and additional capabilities of the code:

- Currently, the Nitrogen ionization model is hard-coded into the solver. To make the code more versatile (e.g. to model rocket exhaust flow) it needs to be able to take in any number of species and ionization equations. This requires implementation of reaction model similar to the one available with OpenFOAM ReactingFOAM solver.

- The plasma takes up a relatively small region when compared to the entire domain. This is especially true for the shock around a wedge configuration. Therefore it might be computationally viable to have an additional "neutral gas domain", which would have the fluid flow equations and the Gauss equation with zero charge (Eq. 2.14). This would avoid the need to compute the charged particle distribution and all of the ionization parameters in this "neutral gas domain".

- Another way to speed up the computations is to add dynamic mesh capabilities to the code. "Dynamic mesh" refers to the refinement of the mesh during the computations once certain conditions are met. This would allow for a refined region limited to the sheath and plasma regions with high concentrations of charged particles, while maintaining a coarser mesh everywhere else. OpenFOAM 2.4.0 (the version that was used for this work) has dynamic mesh library for 3D meshes only, therefore a 2D dynamic mesh library would need to be implemented. Perhaps later versions of OpenFOAM will allow such capabilities, otherwise they would have to be developed.

- Another method to improve both the performance and stability of the solver is to implement the model similar to the one proposed by Parent [82]. Parent shows that it is possible to have very stable and relatively fast computations by obtaining electric potential from Ohm's Law rather than from Gauss' Law.

The current solver or an updated version of it could further be used to model different aspects of plasma-flow interactions such as:

- Research of possible configuration to affect the geometry/position of a shock either directly or though boundary layer control.

- Research of chemically active flow in the presence of plasma (e.g. scramjet propulsion, rocket exhaust flow).

- Modelling 3D PA configurations might also show more features of plasma-shock interaction.

List of References

[1] A. Fridman. *Plasma Chemistry*. Cambridge University Press. ISBN 9781139471732 (2008).

[2] J. Poggie, I. Adamovich, N. Bisek, and M. Nishihara. "Numerical simulation of nanosecond-pulse electrical discharges." *Plasma Sources Science and Technology* **22**(1), 015001(1–17). ISSN 0963-0252 (2013).

[3] M. Nishihara, D. Gaitonde, and I. Adamovich. "Effect of Nanosecond Pulse DBD Plasma Actuators on Oblique Shocks and on Shock / Boundary Layer Interaction." In "51st AIAA Aerospace Sciences Meeting including the New Horizons Forum and Aerospace Exposition," January, pages 1–17. AIAA 2013-0461. ISBN 978-1-62410-181-6 (2013).

[4] P. Riherd and S. Roy. "Simulations of Serpentine Plasma Actuators in a Laminar Boundary Layer." In "51st AIAA Aerospace Sciences Meeting including the New Horizons Forum and Aerospace Exposition," January, pages 1–11. AIAA 2013-0102. ISBN 978-1-62410-181-6 (2013).

[5] T. Corke, C. L. C. Enloe, and S. P. S. Wilkinson. "Dielectric Barrier Discharge Plasma Actuators for Flow Control*." *Annual Review of Fluid ...* **42**(1), 505–529. ISSN 0066-4189 (2010).

[6] A. B. Liu, P. F. Zhang, B. Yan, C. F. Dai, and J. J. Wang. "Flow Characteristics of Synthetic Jet Induced by Plasma Actuator." *AIAA Journal* **49**(3), 544–553. ISSN 0001-1452 (2011).

[7] C.-C. Wang and S. Roy. "Numerical Simulation of a Gas Turbine Combustor Using Nanosecond Pulsed Actuators." In "51st AIAA Aerospace Sciences Meeting including the New Horizons Forum and Aerospace Exposition," January, pages 1–17. AIAA 2013-0894. ISBN 978-1-62410-181-6 (2013).

[8] B. Jayaraman and W. Shyy. "Modeling of dielectric barrier discharge-induced fluid dynamics and heat transfer." *Progress in Aerospace Sciences* **44**(3), 139–191. ISSN 03760421 (2008).

[9] W. Shyy, B. Jayaraman, and A. Andersson. "Modeling of glow discharge-induced fluid dynamics." *Journal of Applied Physics* **92**(11), 6434–6443. ISSN 00218979 (2002).

[10] Y.-C. Cho and W. Shyy. "Adaptive control of low-Reynolds number aerodynamics in uncertain environments: Part 1. Disturbance regimes and flow characteristics." *Computers & Fluids* **86**, 582–596. ISSN 00457930 (2013).

[11] Y.-C. Cho and W. Shyy. "Adaptive control of low-Reynolds number aerodynamics in uncertain environments: Part 2. Vortex dynamics and system modeling under stall." *Computers & Fluids* **86**, 597–610. ISSN 00457930 (2013).

[12] P. F. Zhang, B. Yan, a. B. Liu, and J. J. Wang. "Numerical Simulation on Plasma Circulation Control Airfoil." *AIAA Journal* **48**(10), 2213–2226. ISSN 0001-1452 (2010).

[13] Y. Suzen, P. Huang, J. Jacob, and D. Ashpis. "Numerical simulations of plasma based flow control applications." *AIAA 2005-4633* (June), 1–11 (2005).

[14] Y. Suzen, G. Huang, and D. Ashpis. "Numerical simulations of flow separation control in low-pressure turbines using plasma actuators." *AIAA 2007-937* (January), 1–8 (2007).

[15] D. Reasor, R. Lebeau, and Y. Suzen. "Unstructured Grid Simulations of Plasma Actuator Models." In "37th AIAA Fluid Dynamics Conference and Exhibit," June. AIAA 2007-3973. ISBN 978-1-62410-008-6 (2007).

[16] K. Dennis, Y. B. Suzen, and N. Uygun. "Simulations of Plasma Flow Control in Low-Pressure Turbines." *AIAA 2008-543* (January), 1–12 (2008).

[17] A. Santhanakrishnan, J. Jacob, and Y. Suzen. "Flow Control Using Plasma Actuators and Linear/Annular Plasma Synthetic Jet Actuators." In "3rd AIAA Flow Control Conference," June, pages 1–31. AIAA 2006-3033. ISBN 978-1-62410-036-9 (2006).

[18] K. Asada and K. Fujii. "Burst frequency effect of DBD plasma actuator on the control of separated flow over an airfoil." *AIAA 2012-3054* (June), 1–12 (2012).

[19] M. Sato, K. Okada, T. Nonomura, H. Aono, A. Yakeno, K. Fujii, K. Asada, and Y. Abe. "Massive Parametric Study by LES on Separated-Flow Control around Airfoil using DBD Plasma Actuator at Reynolds Number 63,000." *AIAA 2013-2750* pages 1–24 (2013).

[20] D. Kim and M. Wang. "Large-eddy simulation of flow over a circular cylinder with plasma-based control." *AIAA 2009-1080* (January), 1–17 (2009).

[21] Y. Cheng, X. Che, and W. Nie. "Numerical Study on Propeller Flow-Separation Control by DBD-Plasma Aerodynamic Actuation." *IEEE Transactions on Plasma Science* **41**(4), 892–898. ISSN 0093-3813 (2013).

[22] M. Orlov, D. *Modelling and simulation of single barrier discharge plasma actuator*. Ph.D. thesis, Notre Dame, Indiana (2006).

[23] B. Mertz and T. C. Corke. "Time-Dependent Dielectric Barrier Discharge Plasma Actuator Modeling." In "47th AIAA Aerospace Sciences Meeting including The New Horizons Forum and Aerospace Exposition," January 2008, pages 1–12. AIAA 2009-1083. ISBN 978-1-60086-973-0 (2009).

[24] D. Orlov and T. Corke. "Numerical simulation of aerodynamic plasma actuator effects." *AIAA 2005-1083* (January), 1–12 (2005).

[25] D. Orlov, T. Corke, and M. Patel. "Electric circuit model for aerodynamic plasma actuator." *AIAA 2006-1206* (January), 9–12 (2006).

[26] D. Orlov, T. Apker, C. He, H. Othman, and T. Corke. "Modeling and Experiment of Leading Edge Separation Control Using SDBD Plasma Actuators." In "45th AIAA Aerospace Sciences Meeting and Exhibit," January, pages 8–11. AIAA 2007-877. ISBN 978-1-62410-012-3 (2007).

[27] J. Poggie and I. Adamovich. "Numerical simulation of nanosecond-pulse electrical discharges." *AIAA 2012-1025* (January) (2012).

[28] S. Roy and D. V. Gaitonde. "Modeling Surface Discharge Effects of Atmospheric RF on Gas Flow Control." pages 10–13. AIAA 2005-160. ISBN 978-1-62410-064-2 (2005).

[29] S. Roy and D. Gaitonde. "Multidimensional Collisional Dielectric Barrier Discharge for Flow Separation Control at Atmospheric Pressures." In "35th AIAA Fluid Dynamics Conference and Exhibit," pages 1–10. AIAA 2005-4631. ISBN 978-1-62410-059-8 (2005).

[30] H. Kumar and S. Roy. "Multidimensional hydrodynamic plasma-wall model for collisional plasma discharges with and without magnetic-field effects." *Physics of Plasmas* **12**(9), 093508(1–10). ISSN 1070664X (2005).

[31] K. P. Singh and S. Roy. "Simulation of an asymmetric single dielectric barrier plasma actuator." *Journal of Applied Physics* **98**(8), 083303(1–7). ISSN 00218979 (2005).

[32] K. Singh, S. Roy, and D. Gaitonde. "Modeling of Dielectric Barrier Discharge Plasma Actuator with Atmospheric Air Chemistry." In "37th AIAA Plasmadynamics and Lasers Conference," pages 1–11. AIAA 2006-3381. ISBN 978-1-62410-034-5 (2006).

[33] K. P. Singh and S. Roy. "Force approximation for a plasma actuator operating in atmospheric air." *Journal of Applied Physics* **103**(1), 013305(1–6). ISSN 00218979 (2008).

[34] R. Durscher and S. Roy. "Force Measurement Techniques and Preliminary Results Using Aerogels and Ferroelectrics for Dielectric Barrier Discharge Actuators." In "42nd AIAA Plasmadynamics and Lasers Conference," June, pages 1–14. AIAA 2011-3735. ISBN 978-1-62410-147-2 (2011).

[35] C.-C. Wang, R. Durscher, and S. Roy. "Three-dimensional effects of curved plasma actuators in quiescent air." *Journal of Applied Physics* **109**(8), 083305(1–9). ISSN 00218979 (2011).

[36] J. Shang and G. Huang. "Simulating Electrodynamic Field of Dielectric Barrier Discharge." In "39th Plasmadynamics and Lasers Conference," June, pages 1–12. AIAA 2008-3777. ISBN 978-1-60086-990-7 (2008).

[37] P. G. Huang, J. S. Shang, and S. A. Stanfield. "Periodic Electrodynamic Field of Dielectric Barrier Discharge." *AIAA Journal* **49**(1), 119–127. ISSN 0001-1452 (2011).

[38] S. O. Macheret, M. N. Shneider, and R. B. Miles. "Electron beam generated plasmas in hypersonic MHD channels." *AIAA 99-3635* pages 1–43 (1999).

[39] S. O. Macheret, M. N. Shneider, and R. B. Miles. "MHD POWER EXTRACTION FROM COLD HYPERSONIC AIR FLOW WITH EXTERNAL IONIZERS." *AIAA 99-4800* pages 1–12 (1999).

[40] S. O. Macheret, M. N. Shneider, and R. B. Miles. "Modeling of discharges generated by electron beams in dense gases: Fountain and thunderstorm regimes." *Physics of Plasmas* **8**(5), 1518. ISSN 1070664X (2001).

[41] S. O. Macheret, M. N. Shneider, and R. B. Miles. "Modeling of air plasma generation by repetitive high-voltage nanosecond pulses." volume 30, pages 1301–1314. IEEE-INST ELECTRICAL ELECTRONICS ENGINEERS INC. ISBN 0093-3813 (2002).

[42] S. O. Macheret, M. N. Shneider, and R. B. Miles. "Magnetohydrodynamic Control of Hypersonic Flows and Scramjet Inlets Using Electron Beam Ionization." *AIAA Journal* **40**(1), 74–81. ISSN 0001-1452 (2002).

[43] S. O. Macheret, M. N. Shneider, and R. B. Miles. "Magnetohydrodynamic Power Extraction from Cold Hypersonic Airflows with External Ionizers." *Journal of Propulsion and Power* **18**(2), 424–431. ISSN 0748-4658 (2002).

[44] S. O. Macheret, M. N. Shneider, and R. B. Miles. "Magnetohydrodynamic and Electrohydrodynamic Control of Hypersonic Flows of Weakly Ionized Plasmas." *AIAA Journal* **42**(7), 1378–1387. ISSN 0001-1452 (2004).

[45] A. Likhanskii, M. Shneider, S. Macheret, and R. B. Miles. "Modeling of Interaction Between Weakly Ionized Near-Surface Plasmas and Gas Flow." In "44th AIAA Aerospace Sciences Meeting and Exhibit," January, pages 1–26. AIAA 2006-1204. ISBN 978-1-62410-039-0 (2006).

[46] B. Parent, S. O. Macheret, M. Shneider, and N. Harada. "Numerical Study of an Electron-Beam-Confined Faraday Accelerator." *Journal of Propulsion and Power* **23**(5), 1023–1032. ISSN 0748-4658 (2007).

[47] A. V. Likhanskii, M. N. Shneider, S. O. Macheret, and R. B. Miles. "Modeling of dielectric barrier discharge plasma actuator in air." *Journal of Applied Physics* **103**(5), 053305(1–13). ISSN 00218979 (2008).

[48] S. Leonov, D. Opaits, R. B. Miles, and V. Solov'ev. "Time-Resolved Measurements of Plasma-Induced Momentum of Air and N2 under DBD Actuation." In "49th AIAA Aerospace Sciences Meeting including the New Horizons Forum and Aerospace Exposition," January, pages 1–11. AIAA 2011-1141. ISBN 978-1-60086-950-1 (2011).

[49] A. Starikovskiy and R. B. Miles. "Dielectric Barrier Discharge Control and Flow Acceleration Enhancement by Diode Surface." In "51st AIAA Aerospace

Sciences Meeting including the New Horizons Forum and Aerospace Exposition," January. AIAA 2013-754. ISBN 978-1-62410-181-6 (2013).

[50] J. P. Boeuf and L. C. Pitchford. "Electrohydrodynamic force and aerodynamic flow acceleration in surface dielectric barrier discharge." *Journal of Applied Physics* **97**(10), 103307(1–10). ISSN 00218979 (2005).

[51] J. Shang. "Electromagnetic Field of Dielectric Barrier Discharge." In "36th AIAA Plasmadynamics and Lasers Conference," June, pages 1–10. AIAA 2005-5182. ISBN 978-1-62410-060-4 (2005).

[52] D. Lee, J. M. Park, S. H. Hong, and Y. Kim. "Numerical simulation on mode transition of atmospheric dielectric barrier discharge in helium-oxygen mixture." *IEEE Transactions on Plasma Science* **33**(2), 949–957. ISSN 0093-3813 (2005).

[53] C. A. Shi, K. Adamiak, and G. S. P. Castle. "Numerical study of the characteristics of a dielectric barrier discharge plasma actuator." *Journal of Physics D: Applied Physics* **51**(9), 095201 (2018).

[54] A. Nakano and H. Nishida. "Physical mechanism of dual-grounded trielectrode plasma actuator." *AIAA Journal* **55**(11), 3781–3788 (2017).

[55] G. I. Font. "Boundary Layer Control with Atmospheric Plasma Discharges." *AIAA 2004-3574* **44**(7), 1572–1578. ISSN 0001-1452 (2004).

[56] G. Font and W. Morgan. "Plasma Discharges in Atmospheric Pressure Oxygen for Boundary Layer Separation Control." In "35th AIAA Fluid Dynamics Conference and Exhibit," volume 4632. AIAA 2005-4632. ISBN 978-1-62410-059-8 (2005).

[57] G. I. Font, S. Jung, C. Enloe, T. McLaughlin, W. Morgan, and J. Baughn. "Simulation of the Effects of Force and Heat Produced by a Plasma Actuator on Neutral Flow Evolution." In "44th AIAA Aerospace Sciences Meeting and Exhibit," AIAA 2006-167. ISBN 978-1-62410-039-0 (2006).

[58] G. Font, L. Enloe, T. Mclaughlin, and D. Orlov. "Plasma Discharge Characteristics and Experimentally Determined Boundary Conditions for a Plasma Actuator." In "45th AIAA Aerospace Sciences Meeting and Exhibit," pages 1–14. AIAA 2007-188. ISBN 978-1-62410-012-3 (2007).

[59] M. Huerta and L. Ludeking. "Simulations of Initial Argon Dielectric Barrier Discharges Using the PIC Code Magic." In "48th AIAA Aerospace Sciences

Meeting Including the New Horizons Forum and Aerospace Exposition," January. AIAA 2010-963. ISBN 978-1-60086-959-4 (2010).

[60] M. Kotsonis and S. Ghaemi. "Experimental and numerical characterization of a plasma actuator in continuous and pulsed actuation." *Sensors and Actuators A: Physical* **187**, 84–94. ISSN 09244247 (2012).

[61] M. Kotsonis, R. Giepman, S. Hulshoff, and L. Veldhuis. "Numerical Study of the Control of Tollmiena - Schlichting Waves Using Plasma Actuators." *AIAA Journal* **51**(10), 2353–2364. ISSN 0001-1452 (2013).

[62] D. Gaitonde, K. Shaler, M. Sahin, B. Glaz, and S. Dinavahi. "High-Fidelity Simulations of NS-DBD-based Control of a Stalled NACA0015 Airfoil." In "51st AIAA Aerospace Sciences Meeting including the New Horizons Forum and Aerospace Exposition," January, pages 1–16. AIAA 2013-1118. ISBN 978-1-62410-181-6 (2013).

[63] J. G. Zheng, Y. D. Cui, J. Li, and B. C. Khoo. "A note on supersonic flow control with nanosecond plasma actuator." *Physics of Fluids* **30**(4), 040907 (2018).

[64] N. Webb, C. Clifford, and M. Samimy. "An investigation of the control mechanism of plasma actuators in a shock wave-boundary layer interaction." *AIAA 2013-0402* (January), 1–13 (2013).

[65] S. Pavon, P. Ott, and P. Leyland. "Effects of a surface dielectric barrier discharge on transonic flows around an airfoil." *AIAA 2009-649* (January), 1–25 (2009).

[66] S. B. Leonov and D. Yarantsev. "Near-Surface Electrical Discharge in Supersonic Airflow: Properties and Flow Control." *Journal of Propulsion and Power* **24**(6), 1168–1181. ISSN 0748-4658 (2008).

[67] Q. Sun, Y. Li, B. Cheng, W. Cui, W. Liu, and Q. Xiao. "The characteristics of surface arc plasma and its control effect on supersonic flow." *Physics Letters A* **378**(36), 2672–2682. ISSN 03759601 (2014).

[68] H. Wang, J. Li, D. Jin, M. Tang, Y. Wu, and L. Xiao. "High-frequency counterflow plasma synthetic jet actuator and its application in suppression of supersonic flow separation." *Acta Astronautica* **142**, 45 – 56. ISSN 0094-5765 (2018).

[69] OpenFOAM Foundation. *OpenFOAM, The Open Source CFD Toolbox, Version 2.2* (2013).

[70] *Physical Values Handbook*. EnergoAtomIzdat (1991).

[71] *Tables of Physical & Chemical Constants*, chapter 4.4 Free electrons and ions in gases. Kaye & Laby Online, 16th edition (2005).

[72] Y. P. Raizer. *Gas Discharge Physics*. Springer-Verlag (1997).

[73] M. Abdollahzadeh, J. Páscoa, and P. Oliveira. "Two-dimensional numerical modeling of interaction of micro-shock wave generated by nanosecond plasma actuators and transonic flow." *Journal of Computational and Applied Mathematics* **270**, 401–416. ISSN 03770427 (2014).

[74] N. A. Popov. "Investigation of the mechanism for rapid heating of nitrogen and air in gas discharges." *Plasma Physics Reports* **27**(10), 886–896. ISSN 1562-6938 (2001).

[75] Guerra, V., Sá, P. A., and Loureiro, J. "Kinetic modeling of low-pressure nitrogen discharges and post-discharges." *Eur. Phys. J. Appl. Phys.* **28**(2), 125–152 (2004).

[76] Flitti, A. and Pancheshnyi, S. "Gas heating in fast pulsed discharges in n2-o2 mixtures." *Eur. Phys. J. Appl. Phys.* **45**(2), 21001 (2009).

[77] B. van Leer. "Towards the ultimate conservative difference scheme. ii. monotonicity and conservation combined in a second-order scheme." *Journal of Computational Physics* **14**(4), 361–370. ISSN 0021-9991 (1974).

[78] *An Introduction to Computational Fluid Dynamics, the Finite Volume Method*. Pearson Education Limited. ISBN 9780131274983 (2007).

[79] C. J. Freitas, U. Ghia, I. Celik, P. Roache, and P. Raad. "AIAA 2003-627 ASME ' S QUEST TO QUANTIFY NUMERICAL UNCERTAINTY Computational Fluid Dynamics Technical Committee Fluids Engineering Division American Society of Mechanical Engineers American Institute of Aeronautics and Astronautics." (January), 1–7 (2003).

[80] DuPont. *DuPont Kapton FPC, Specifications* (2022).

[81] F. M. White. *Fluid Mechanics*, chapter 7. McGraw-Hill Publishing Company (1999).

[82] B. Parent, M. N. Shneider, and S. O. Macheret. "Detailed Modeling of Plasmas for Computational Aerodynamics." *AIAA Journal* **54**(3), 898–911. ISSN 0001-1452 (2016).